

MOHAMMAD EBRAHIM MOUSA PASANDI

**IMPLEMENTATION OF RADIO-OVER-FIBER
OFDM SYSTEM INCLUDING A NOVEL OPTICAL
NULL-STEERING BEAMFORMER**

Mémoire présenté
à la Faculté des études supérieures de l'Université Laval
dans le cadre du programme de maîtrise en génie électrique
pour l'obtention du grade de maître ès sciences (M.Sc.)

DÉPARTEMENT DE GÉNIE ÉLECTRIQUE ET DE GÉNIE INFORMATIQUE
FACULTÉ DES SCIENCES ET DE GÉNIE
UNIVERSITÉ LAVAL
QUÉBEC

2008

© Mohammad Ebrahim Mousa Pasandi, 2008

To my beloved parents

Résumé

L'objectif de ce projet est de concevoir et d'optimiser un système radio-sur-fibre, basé sur OFDM, incluant un nouveau *beamformer* optique avec une capacité de déplacer les points nuls appropriés pour les réseaux locaux sans fil.

Dans le premier chapitre, nous présentons les définitions et les connaissances nécessaires à la compréhension du présent mémoire. Nous introduisons le concept de manipulation de phase et de délai dans le but d'orienter un faisceau. Nous expliquons l'idée générale derrière la formation de faisceau électrique et optique, le concept de beamformer et quelques uns de ses avantages pour les systèmes de communication sans fil avancés.

Comme démonstration expérimentale de la formation de faisceau, nous avons fait le design et fabriqué un réseau d'antennes à l'aide de technologie à *microstrip*. Dans le second chapitre, nous présentons la procédure du design à un élément, la technique d'adaptation d'impédance et certains éléments additionnels qu'il est nécessaires de considérer lors de la fabrication du réseau d'antennes.

Dans le troisième chapitre, nous étudions les diverses techniques de la formation de faisceau. Nous débutons par présenter les avantages et les désavantages des méthodes déjà existantes. Par la suite, le cœur du projet, qui concerne le contrôle indépendant de l'amplitude et de la phase de chaque canal, est introduit. La description du design et la comparaison entre les résultats numériques et expérimentaux démontrent la faisabilité du système. Également, l'impact de ces filtres optiques sur la qualité du signal transmis est étudié. Dans ce mémoire, nous avons considéré le format de modulation IEEE 802.11 comme étant le plus sophistiqué et celui le plus couramment utilisé dans le domaine des réseaux locaux sans fil.

Dans le dernier chapitre, nous présentons des résultats de patrons de radiation mesurés, obtenus en combinant le *beamformer* au réseau d'antennes dans un lien de radio-sur-fibre optimisé. Une discussion concernant les avantages, les désavantages et les travaux futurs permettant d'améliorer ce prototype concluront ce mémoire.

Abstract

The objective of this research is to implement an optimized OFDM-based radio-over-fiber system including a novel optical null-steering beamformer well-suited for wireless-local-area-network applications.

In the first chapter we provide definitions and background that we will need in presenting our research results. We introduce delay and phase manipulations for steering the beam direction. We explain the general idea behind electrical and optical beamformers. We introduce the concept of null-steering beamformer and some of its capabilities in advanced wireless systems.

For the experimental demonstration of the null-steering beamforming, we have fabricated a phased-array-antenna using microstrip technology. In the second chapter, we discuss the design procedure for a single element radiator, its matching technique and introduce related considerations to array fabrication.

In the third chapter, we study optical beamforming techniques. First, we review some previously proposed ideas in this area, their advantages and disadvantages. Then, the heart of this optical null-steering beamformer, the independent control over the phase and amplitude for each channel, is introduced. By describing the method of design and its evolution and then by comparing the simulation and measurement results, we demonstrate the feasibility of this system. The impact of these optical filters on the transmitted signal quality is studied. We consider the IEEE 802.11 as one the most sophisticated modulation formats commonly used for wireless-local-area-network applications.

In the last chapter, we show the pattern measurement results obtained by combining the null-steering beamformer to the phased-array-antenna in an optimized radio-over-fiber link. A discussion about the advantages, disadvantages and future possible efforts for improving this prototype will conclude the results that we have obtained.

Acknowledgement and Thanks

I would like to express my sincere gratitude to my advisor, Professor Sophie LaRoche, for her endless encouragement, support and guidance. Her insight and knowledge makes her a great professor, but her gentle, caring, compassionate character makes her a remarkable person. In spite of her busy schedule, I never had any difficulty to arrange a meeting with her to discuss scientific or personal problems, and I always enjoyed her intelligence and vision. She was much more than a professor to me and helped me to adapt the myriad of changes I faced in a foreign country. It is my great honor to be her student.

I would also like to thank my co-advisor, Professor Leslie A. Rusch. I truly appreciate the invaluable discussions about wireless systems and OFDM aspects of my project, and her bright ideas and comments. I am grateful to Professor Sebastien Roy for all the helps in providing antenna substrate and wireless measurement facilities.

Many thanks to my talented and experienced colleagues: Marco Michele Sisto, Serge Doucet and all the rest, who helped me in various forms to finalize my project. They always put the same amount of time and energy in brainstorming my problems, as they would put for their own. Special thanks to Marco for the motivating discussions, teaching me experimental work, and sharing with me his technical experience.

I would like to acknowledge and thank the staff of “Centre d’optique, photonique et laser” (COPL) and technicians for their assistance, particularly Patrick LaRoche and Philippe Chrétien.

My deep love and appreciation goes to my parents for their support, kindness and patience in all and every stage of my life. They devoted their heart and soul to advance my education and encourage me to love learning and hardworking.

My sincere gratitude to you all,

Mohammad Ebrahim Mousa Pasandi

Table of Contents

Résumé.....	iii
Abstract.....	iv
Acknowledgement and Thanks.....	v
List of Figures.....	ix
List of Acronyms.....	xiii
CHAPTER 1 INTRODUCTION.....	1
1.1. Introduction.....	1
1.2. Beam-Steering Concept.....	3
1.3. Beamforming in the Electrical Domain.....	5
1.4. Optical Beamforming	6
1.5. Null-Steering Beamforming	9
1.6. About This Work	11
CHAPTER 2 DESIGN AND FABRICATION OF THE ANTENNA ARRAY	14
2.1. Introduction.....	14
2.2. Uniformly Excited Linear Arrays.....	17
2.2.1. Pattern Formulations	17
2.2.2. Half Power Beamwidth	18
2.2.3. Grating Lobes.....	19
2.3. Microstrip Patches.....	19
2.3.1. Advantages and Disadvantages	20
2.3.2. Feed Techniques.....	21
2.3.3. Transmission-Line Model	22
2.4. Microstrip Antenna Design and Fabrication.....	26

2.4.1. Substrate Selection	26
2.4.2. Radiator Element Design	28
2.4.3. Impedance Matching	29
2.4.4. Array Fabrication	32
2.4.5. Experimental Results for our Designed and Fabricated Array	33
2.5. Conclusion	36
CHAPTER 3 OPTICAL BEAMFORMING TECHNIQUES.....	37
3.1. Introduction.....	37
3.2. Fiber Bragg Grating Technology.....	38
3.3. Optical Beamforming Methods.....	40
3.3.1. TTD Beamforming Using a Fiber Grating Prism	41
3.3.2. TTD Beamforming Using CFBG and Multiwavelength Tunable Laser	43
3.3.3. TTD Beamforming Using Tunable CFBG	45
3.4. Independent Optical Control over the Phase and Amplitude.....	48
3.4.1. ϕ_{ij} and ϕ_i Control based on Gires-Tournois Filters	50
3.4.2. A New Design Approach	61
3.5. Effect of Beamformer Filters on Signal Quality and Radiation Pattern.....	65
3.5.1. IEEE 802.11 Modulation Format for WLAN Application	66
3.5.2. Experimental Verification of the Beamformer Effect on Signal Quality	66
3.5.3. Beam Squint	69
3.6. Conclusion	70
CHAPTER 4 ROF LINK IMPLEMENTATION AND RADIATION PATTERN MEASUREMENT	72
4.1. Introduction.....	72
4.2. ROF Link Architecture and Hardware	74
4.2.1. Multi-carrier Laser Source	74
4.2.2. RF-Gain Improvement and Distortion Compensation by Employing MZ Modulator Bias Optimization.....	77
4.2.3. FBG Actuators	78

4.2.4. Appropriate Optical Detection Stage	80
4.3. Link Calibration.....	82
4.4. Radiation Pattern Simulation and Measurement.....	86
4.5. Source of Errors in the Optical Domain	90
4.6. DG-BF Advantages and Disadvantages	91
4.7. Conclusion	93
CHAPTER 5 CONCLUSION	94
REFERENCES	97

List of Figures

Figure 1-1	Schematic of beam-steering with delay and phase manipulation for a four-element PAA.	4
Figure 1-2	Schematic of a typical electrical beamformer.	6
Figure 1-3	Schematic of a typical optical beamformer.	7
Figure 1-4	SLL ratio adjustment by amplitude manipulation in a four-element uniform linear array with half-wave spacing pointing at 30° , by applying different relative attenuations.	8
Figure 1-5	Schematic of the proposed ROF link including the beamformer module.	12
Figure 1-6	Achievable amount of beam-steering range versus the inter-element phase tunability for a linear uniform array with half-wave spacing.	13
Figure 2-1	Linear array geometry.	18
Figure 2-2	Microstrip line feed schematic.	21
Figure 2-3	Schematic of coaxial feed.	22
Figure 2-4	Structure of a rectangular microstrip antenna.	23
Figure 2-5	Electric field lines.	24
Figure 2-6	Matching parameters.	30
Figure 2-7	Array layout for printing over the substrate (a) and the fabricated home-made array (b).	31
Figure 2-8	S11 measurement (red trace) and simulation (blue trace) comparison for home-made antenna.	34
Figure 2-9	Pattern measurement of a single element home-made microstrip antenna.	35
Figure 3-1	The transverse holographic method for writing fiber gratings. Two coherent UV beams produce an interference pattern in the fiber. The periodicity of the resulting grating is dependent on the angles of the	40

	incident beams.	
Figure 3-2	Integrated transmit/receive optical beamforming system illustrating the spatial layout of the Bragg gratings for the FGP, shown for the case of a four-element array with five discrete steering angles [29].	42
Figure 3-3	Schematic of a PAA steered by a CFBG. Different optical wavelengths are routed to the radiators through a WDM system [26].	44
Figure 3-4	Configuration of the beamformer based on tunable CFBGs for a four-element array [28].	46
Figure 3-5	Schematic of the beamformer based on tunable CFBG for a four-element array complying WDM configuration [32].	48
Figure 3-6	The single-channel architecture of the proposed novel optical beamformer.	50
Figure 3-7	Theory of operation of the GT-BF for one optical wavelength.	51
Figure 3-8	Design of the optimum GT-CC.	53
Figure 3-9	Map representing the normalized amplitude (a) and wrapped phase (b) response of the GT-BF as a function of the shift of the delay peaks from the reference position centered on the modulation sidebands.	54
Figure 3-10	Measured insertion loss and group delay of the single-cavity GT-CCs.	56
Figure 3-11	Simulation and measurement of amplitude and phase maps for single-cavity GT-CC.	58
Figure 3-12	Setup for measurement of the amplitude and phase maps.	59
Figure 3-13	Proposed architecture for DWDM-ROF link using GT-BF.	60
Figure 3-14	Reflectivity and delay of the FBGL (a) and FBGU (b) for DG-BF.	61
Figure 3-15	Simulated amplitude (a) and phase (b) maps of the DG-BF.	62
Figure 3-16	Measured reflectivity and delay of the FBGL (a) and FBGU (b).	62
Figure 3-17	Measured amplitude (a) and phase (b) maps of the DG-BF.	63
Figure 3-18	Comparison between phase retardation on the secondary diagonal: simulation (a) and measurement (b).	63
Figure 3-19	The multichannel DG-BF.	65

Figure 3-20	Measured EVM response for the single-cavity GT-BF.	68
Figure 3-21	Errors in definition of the radiation diagram: a) error on the HPBW; b) error on the pointing direction; c) error percentage on the pointing direction normalized by the beamwidth.	70
Figure 4-1	Multi-channel WLAN-ROF link including DG-BF.	73
Figure 4-2	Schematic diagram for the multi-carrier generator.	74
Figure 4-3	Measurement setup for examining the signal quality after transmission over the ROF link using a multi-carrier generator.	75
Figure 4-4	Measured optical spectrum and corresponding EVM values.	76
Figure 4-5	Transfer function of the MZ modulator with $V_{bias} = 0$ at the minimum transmission point.	77
Figure 4-6	Schematic diagram (a) and a fabricated version (b) of each FBG actuator.	79
Figure 4-7	Schematic diagram (a) and the fabricated version (b) of the actuators for each chain of DG-BF designed for four-channel application.	80
Figure 4-8	Electronic circuit for a photodiode working as a single-channel detection stage.	81
Figure 4-9	Schematic diagram of the setup used for multichannel calibration.	82
Figure 4-10	Calibration amplitude and phase information versus temperature adjustment for all channels.	83
Figure 4-11	Cumulative phase versus grating displacement of the FBG_{LS} under different strains.	85
Figure 4-12	Measured unwrapped phase retardation and amplitude variation versus symmetric temperature deviation of the two corresponding gratings for each channel.	86
Figure 4-13	Measured (blue curves) and simulated (red curves) radiation pattern diagrams of a four-element array with half-wave spacing for pointing angles of: a) -14° , b) -45° , c) 30° and d) -60° .	87
Figure 4-14	Simulation (red curves) and measurement (blue curves) of the radiation pattern diagram for a four-element array with half-wave spacing	88

while pointing at 0° using the uniform (a) and 3 dB tapered (b) amplitude distribution.

Figure 4-15 Simulation (red curves) and measurement (blue curves) of the radiation pattern diagram for a four-element array with half-wave spacing while pointing at 30° using the uniform (a) and 3 dB tapered (b) amplitude distribution. 88

List of Acronyms

AWG	Arrayed Waveguide Grating
BER	Bit Error Rate
CDMA	Code Division Multiple Access
CFBG	Chirped Fiber Bragg Grating
CO	Central Office
CW	Continuous Wave
DFB	Distributed Feedback
DG-BF	Discrete Gratings Beamformer
DSB	Double Side Band
DWDM	Dense Wavelength Division Multiplexing
EDFA	Erbium Doped Fiber Amplifier
EOM	Electro Optical Modulation
EVM	Error Vector Magnitude
FBG	Fiber Bragg Grating
FDMA	Frequency Division Multiple Access
FSR	Free Spectral Range
FGP	Fiber Grating Prism
GL	Grating Lobe
GT-BF	Gires Tournois Beamformer
GT-CC	Gires Tournois Coupled Cavity
HPBW	Half Power Beam Width
ID3	Third Order Intermodulation Distortion
MEMS	Micro Electro Mechanical Systems
MIC	Microwave Integrated Circuits
MIMO	Multiple-Input Multiple-Output
MZ	Mach Zehnder
OFDM	Orthogonal Frequency Division Multiplexing

OMD	Optical Modulation Depth
OSNR	Optical Signal to Noise Ratio
PA	Power Amplifier
PAA	Phased Array Antenna
PAPR	Peak to Average Power Ratio
PCB	Printed Circuit Board
PD	Photo Detector
PM	Phase Modulator
QAM	Quadrature Amplitude Modulation
RF	Radio Frequency
RL	Return Loss
ROF	Radio Over Fiber
SDMA	Space Division Multiple Access
SINR	Signal to Interference plus Noise Ratio
SLL	Side Lobe Level
SMF	Single Mode Fiber
SNR	Signal to Noise Ratio
SSB	Single Side Band
TEM	Transverse Electric Magnetic
TDMA	Time Division Multiple Access
TLS	Tunable Laser Source
TTD	True Time Delay
VSA	Vector Signal Analyzer
VSG	Vector Signal Generator
VSWR	Voltage Standing Wave Ratio
WDM	Wavelength Division Multiplexing
WLAN	Wireless Local Area Network

Chapter 1

Introduction

1.1. Introduction

The field of wireless communications is growing at an explosive rate, covering many technical areas such as digital communication, electronic circuit design, antenna and microwave engineering, wireless networks and recently even optical communication. The worldwide activities in this industry are a sign of its huge economic significance. The demand for wireless communication is anticipated to expand steadily in the number of users, new services and the accessible coverage range [1-2]. This demand and the scarcity of the radio frequency (RF) spectrum lead to the need to develop technologies to overcome its limitations.

The application of antenna arrays to mobile communication systems has been suggested recently to overcome the difficulties of limited bandwidth. Many studies show that antenna arrays improve system performance by increasing channel capacity, extending coverage range, tailoring beam shape and steering multiple beams to track many users. The use of arrays also reduces multipath fading, co-channel interference, system complexity, cost and bit-error-rate (BER). Adaptive antennas and the algorithms to control them are vital for new high-capacity communication networks [1], [3].

In general, antennas may be classified as omnidirectional, directional and phased array. An omnidirectional antenna, also called as an isotropic antenna, has identical gain in all directions while a directional antenna has more gain in certain directions and consequently less in others. A phased-array-antenna (PAA) uses an array of simple antennas, such as omnidirectional antennas, and combines the signals on these antennas to shape the array output. Each antenna in the array is known as an element of the array. The direction where the maximum gain appears is controlled by adjusting the phase between different antennas; the signals are added in-phase in the direction where maximum gain is required. This proper phase manipulation is called beam-steering and will result in an array gain equal to the sum of the gains of all individual antennas. Taking advantage of beam-steering theory, PAA can transmit data in a narrow beam towards users in one particular direction, and then switch the beam towards another user in a different direction. As a result, using the same frequency band and allocating different beam slots for different users provides more service capacity with the same bandwidth.

The ability of the PAA to control and optimize the radiation pattern and other transmission parameters translates to other advantages such as obviating mechanical components, increasing the propagation range, and boosting system security. For beam-steering applications, there is no need to rotate the array physically. Therefore the PAA is able to change the beam direction much faster than mechanically-steered antennas while providing greater reliability. The transmission range is increased since the PAA radiated power is more focused (because of the higher directivity) in the direction of the user, instead of being propagated over a broad region. Finally, wireless network security is boosted, as only potential hackers in the same direction as the user can intercept the transmitted signal.

By using PAAs, the standard coverage area of a regular antenna can be divided into several smaller angular segments. The PAA then switches between these different segments to concentrate on different users. This diversity scheme is called space-division multiple-access (SDMA). Currently, there are three different multiple-access schemes to differentiate users occupying the same frequency spectrum. Frequency-division multiple-access (FDMA) allocates each user a certain frequency sub-band within the available bandwidth. Time-division multiple-access (TDMA) allocates each user a specific time slot in which they are allowed to transmit and receive data. Code-division multiple-access (CDMA) encodes the signal with a unique code before being transmitted by the antenna and only receivers with the same code can decode the transmitted data. SDMA can be implemented together with FDMA, CDMA and TDMA diversity schemes to increase the capacity of wireless networks [1].

In addition to wireless communications, PAAs have been studied for many decades in the field of radar, offering several advantages such as target tracking capability, increased detection range, and reduced interference levels [1]. Over the past decade, the interest in PAAs has extended to many other areas, such as satellite communications [4], astronomy [5], and even in automotive applications [6], where PAAs can be exploited in cruise-control systems to avoid collision.

1.2. Beam-Steering Concept

Figure 1.1 shows the diagram of a PAA with four elements, equally-spaced at a distance d . The phase difference $\Delta\varphi$ between the signals applied to adjacent elements controls the steering angle of θ_0 . Each PAA element transmits an electromagnetic field which becomes an individual plane wave in the far-field region. The plane-wave fronts will interfere constructively in the desired direction of θ_0 , if $\Delta\varphi$ corresponds to the path-length difference of $d \sin \theta_0$ between adjacent elements. Therefore, the $\Delta\varphi$ required to steer the beam towards a given direction θ_0 is

$$\Delta\varphi = \frac{2\pi}{c} d f_0 \sin \theta_0 \quad (1.1)$$

where f_0 is the carrier frequency of the transmitted RF signal in Hertz, θ_0 is the steering angle in radian and c is the velocity of light (3×10^8 m/s). Equivalently, the phase difference $\Delta\phi$ can be achieved by delaying the adjacent-element signals in the time domain by

$$\Delta\tau = \frac{d}{c} \sin \theta_0 \quad (1.2)$$

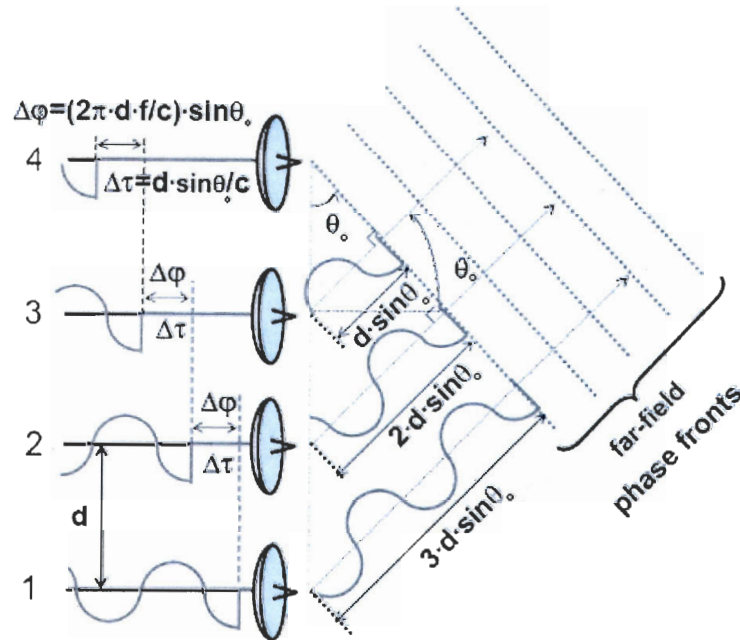


Figure 1-1: Schematic of beam-steering with delay and phase manipulation for a four-element PAA.

For instance, consider a four-element PAA that operates at 5 GHz, and with inter-element spacing of half of the operating wavelength ($d = 30$ mm). To steer the beam toward $\theta_0 = 60^\circ$, the required $\Delta\phi$ is equal to 2.7 rad (155.9 degrees), which corresponds to a $\Delta\tau$ of 86.6 ps.

The PAA elements need not be aligned in a linear arrangement, but can also be arranged in a two-dimensional or three-dimensional grid configuration. In this work, we only study the linear configuration, and therefore we will restrict our discussion to this configuration. The PAA elements may also be any type of antennas such as dipoles, patch apertures or horns [7].

1.3. Beamforming in the Electrical Domain

Figure 1.2 shows a simplified diagram of a typical four-element PAA controlled by an electrical beamformer in the transmit mode. The electrical input signal to be transmitted is first divided by the number of PAA elements through an electrical power splitter. Then, each of these signals passes through a regulator that adjusts the amplitude levels for that channel. Afterwards, each signal is passed through a phase shifter that adjusts to the desired phase. The signals are routed to their respective antenna element, and propagate toward the user.

Beam-steering is achieved by introducing the phase difference ($\Delta\phi$) to the PAA element signals via the phase shifters. There are two types of phase shifters that can be used for this purpose. The first type is called the phase-based phase shifter where the phase shift is dependent on an externally-applied control signal that can be electrical, magnetic, or mechanical. The externally-applied control signal changes the waveguiding characteristics of the device and changes the velocity of the propagating signal. In practice, phase-based phase shifters are made of ferrite materials or pin diodes [8]. This method is the simplest way to implement a phase shifter, as it only requires one component (a phase shifter). Furthermore, any required phase shift can be achieved, as the relation between the phase shift and the external control signal is continuous. However, beamformers that use phase-based phase shifters suffer from beam squint. Beam squint is the phenomenon where the outer frequency components of a broadband signal are transmitted toward different angles. This phenomenon results in signal distortion. While equation 1.1 assumes the signal is concentrated at f_0 , for a wideband signal there is significant energy at frequencies distant from center frequency f_0 . Ideally a phase shift should be determined for each frequency, but this is unmanageable. Phase-based phase shifters introduce an equal amount of phase shift to all frequencies across the spectrum, thus this device results in beam squint. Therefore, beamformers using phase-based phase shifters cannot be used for broadband applications.

The other type of phase shifter is called true-time-delay (TTD) phase shifter. In these phase shifters, electrically-controlled switches are used to switch the propagating signal from one path to another path with a different length, resulting in different delays and this delay difference causes phase shift. Large phase differences can be achieved with these devices over

a relatively short distance. The switching element is the critical component for this type of phase shifter. Recently, beamformers employing micro-electro-mechanical (MEMS) switches have been reported [9]. The drawback of this type of beam-steering circuit is that they can only introduce discrete phase-difference values. The advantage is that they do not suffer from beam squint, so they support larger bandwidths.

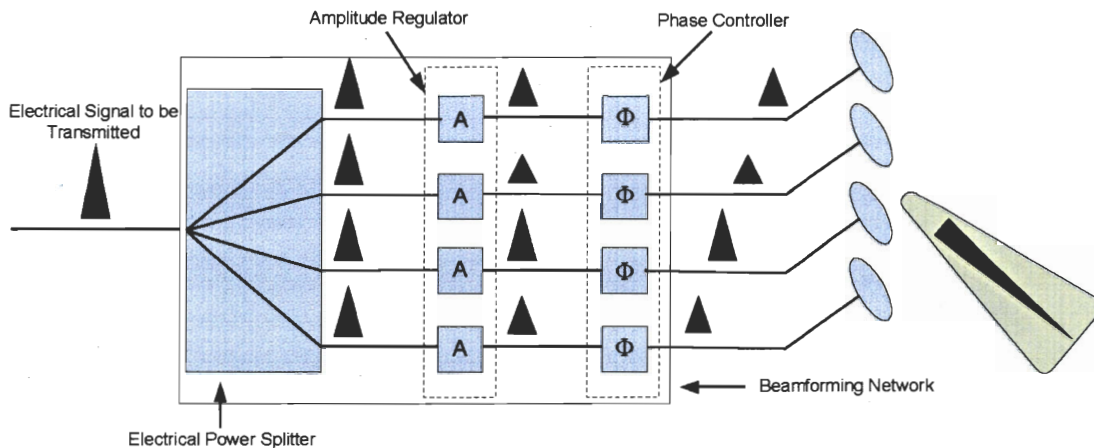


Figure 1-2: Schematic of a typical electrical beamformer.

1.4. Optical Beamforming

In order to provide broadband wireless services for numerous users, we need access to higher carrier frequencies. Electrical circuits operating at high frequencies exist but they tend to be lossy, bulky, heavy, and very susceptible to electromagnetic interference. Optical circuits can be used to alleviate most of the problems encountered with high-frequency electronic circuits [10]. The high-frequency signals can be modulated onto the optical carrier, and subsequently all necessary high-frequency signal processing can be performed in the optical domain. The advantages of the implementation in the optical domain include low propagation losses, small size, low weight, high bandwidth and immunity to electromagnetic interference. Many different types of optical beamformers for high-frequency PAA applications have been reported. An overview of the most recent and elegant optical beamforming techniques is reported in chapter three.

Figure 1.3 depicts a simplified diagram of a typical optical beamformer in the transmit mode. The source can be either a single optical wavelength, or a multiwavelength source to support a wavelength-division-multiplexing (WDM) beamformer. The WDM system employs an optical wavelength demultiplexer instead of an optical power splitter following modulation. Consider the single optical wavelength setup: the signal to be transmitted is first modulated onto a single optical wavelength generated by a laser source. Afterwards, this optical wavelength is divided in power by the number of antenna elements with an optical power splitter. Subsequently, each of the divided signals is connected to an amplitude regulator and a phase controller section. Finally, each of the divided signals is detected by a photodetector (PD), and applied to a PAA element.

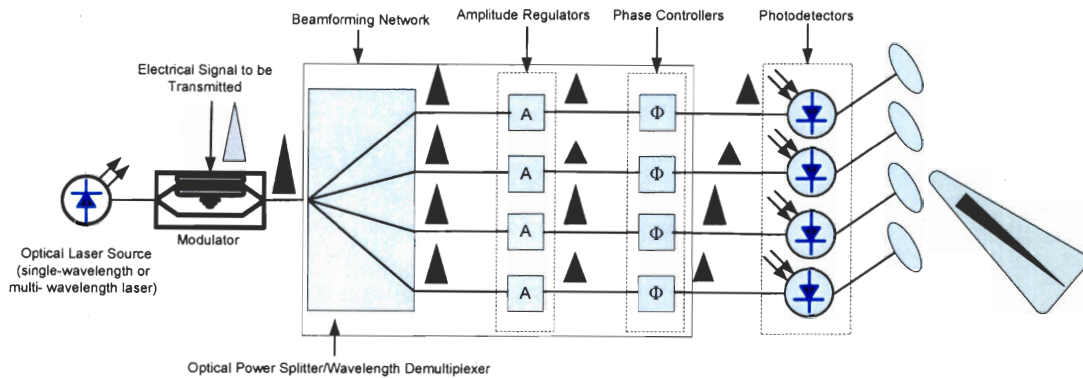


Figure 1-3: Schematic of a typical optical beamformer.

In the WDM beamforming setup, the same signal to be transmitted is modulated onto four optical wavelengths. One of the advantages of electro-optical modulation (EOM) is that a single device can be used to simultaneously modulate an arbitrary number of optical wavelengths. Next, the four optical wavelengths are split by an optical demultiplexer and each wavelength is conveyed through the amplitude regulator and the phase controller, and ultimately applied to the PAA after detection with a PD. Another advantage of optical beamforming is that, because of the low propagation loss, the PAA and the PDs can be placed far from the beamformer, and linked together by a single optical fiber. This allows integration of the components into subsystems to reduce cost. For example, this WDM architecture can be modified by integrating all phase controllers in a unique set to be placed before the de-

multiplexer. This enables the designer to combine the laser source, the EOM and the phase controller set in a single subsystem at a central office (CO) a few kilometers from the PAA.

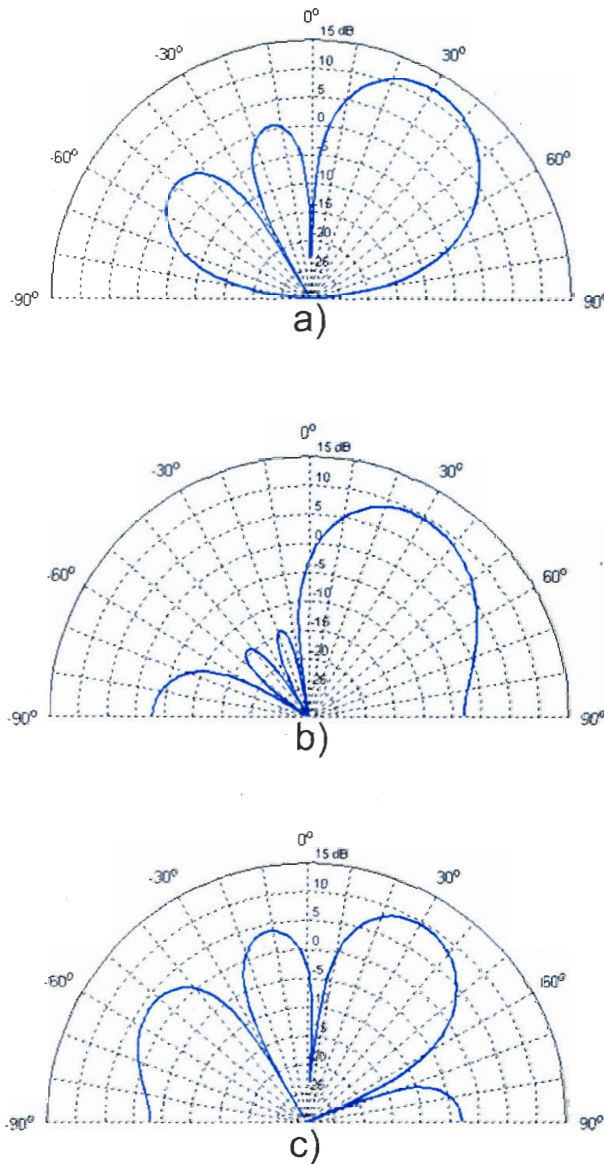


Figure 1-4: SLL ratio adjustment by amplitude manipulation in a four-element uniform linear array with half-wave spacing by applying different relative attenuations: a) 0 dB, 0 dB, 0 dB, 0 dB; b) 0 dB, 3 dB, 3 dB, 0 dB; c) 3 dB, 0 dB, 0 dB, 3 dB. The array elements are omnidirectional antennas.

1.5. Null-Steering Beamforming

Adjusting only the phase of the signals feeding different elements to point a beam in a desired direction is the conventional method of beam-steering in which the amplitude of each signal is kept the same. In this case, the shape of the antenna pattern is unchanged, that is, the relative position of the side-lobes with respect to the main beam and their level. This, however, can be changed by adjusting both amplitude and phase of each signal to shape the pattern. The amount of change depends upon the number of elements in the array. This type of beamforming is known as null-steering beamforming or beam-shaping [1] and the PAA is also called an adaptive array.

The amplitude and phase of the signals for each element may be thought of as a single complex quantity or weight applied to the signals. If there is only one element, weight cannot change the pattern of that antenna. With two elements, however, by changing the weight of one element relative to the other, the pattern can be adjusted to the desired value at one location, that is, it is possible to place one minimum (null) or maximum anywhere in the pattern. Similarly, with three elements, two positions may be determined, and so on. Thus, with an N -element array, $N-1$ positions can be specified. These may be one maximum in the direction of the desired signal and $N-2$ minimums in the directions of unwanted interferers. This flexibility of an N -element adaptive array to fix the pattern at $N-1$ positions is known as the degree of freedom of that adaptive array. For an equally-spaced linear array, this is similar to an $N-1$ degree polynomial of $N-1$ adjustable coefficients, with the first coefficient being unity [1], [7].

Alternately, in this type of beamformer, the side-lobe level (SLL) ratio can be controlled by weighing the elements [7]. Figure 1.4 shows this ability for a four-element linear uniform array with half-wave spacing. When a uniform phase difference of 90° is applied between the array elements and the signal amplitudes are kept the same, the pattern experiences a SLL ratio of 11 dB (Figure 1.4a). Applying a tapered amplitude excitation with 3 dB difference (i.e., attenuation of 3 dB, 0 dB, 0 dB and 3 dB respectively) with the same amount of phase difference of 90° , will result in a pattern with a SLL ratio of more than 14 dB (Figure 1.4b). However the normalized array gain (normalized by the number of elements) is re-

duced by 1.25 dB because less power is fed to the antennas with 3 dB attenuators. Figure 1.4c shows the case when we apply the attenuations of 0 dB, 3 dB, 3 dB and 0 dB respectively. In this case, a stronger side-lobe can be observed with the SLL ratio of 6 dB. Again, the normalized array gain is reduced by 1.25 dB because of two 3 dB attenuators.

Null-steering beamforming is most commonly applied in outdoor wireless networks. However, it has been also proposed for indoor networks to reduce interference and mitigate multipath fading, hence to improve the capacity. For example, Wang [11] uses beamforming in indoor networks to fight multipath fading using a diversity combining technique. Katz [12] combined beamforming and block coding to improve the link diversity of indoor channels. Recently, Chen [13] proposed the use of adaptive arrays in orthogonal-frequency-division-multiplexing (OFDM) systems, in such a way to exploit the characteristics of the OFDM signal to find the radiation pattern that minimizes interference. Interference minimization can be optimized if full control of the antenna radiation diagram is available through simultaneous amplitude and phase control of the antenna elements, in contrast with phase control only [14]. Consider directional sources operating at the same frequency as that of the desired source, but not falling in the direction of the desired source. In situations where the directions of these interferers are known, cancellation is possible by placing the nulls in the pattern in the direction of interferers and simultaneously steering the main beam in the direction of the desired signal. The cancellation of each source of interference by placing a null in the pattern uses one degree of the freedom of the adaptive array.

The advantages described are mostly associated with uplink null-steering beamformers. Several electrical uplink beamformers have been developed and exploited. However, quite a few optical downlink beamformers have been proposed [23-30], to our knowledge, just one optical uplink beamformer has been suggested in [29], but no demonstration was provided.

For both electrical and optical beamformer schemes studied in Section 1.3 and 1.4, beamshaping (null-steering beamforming) can be achieved by not only controlling the phase but also the amplitude of the signal applied to each PAA element. In practice, the amplitude is controlled using electrical/optical attenuators at each antenna element. In this case, the am-

plitude regulators in Figure 1.2 and Figure 1.3 are no longer just a power regulator and they apply the desired set of attenuations in each channel.

1.6. About This Work

The objective of this research is to demonstrate the concept of a novel optical null-steering beamformer, to describe theoretical concepts and to report experimental results. To our knowledge, this type of beamformer has not been reported to date and this work can be considered as an important step toward an all-optical and integrated processing unit for supporting wireless-local-area-network (WLAN) systems using radio-over-fiber (ROF) technologies. The general architecture of the ROF link is shown in Figure 1.5. By using a multiwavelength laser source with a channel spacing of 25 GHz, the link will be compatible with dense WDM (DWDM). Each wavelength feeds one of the array elements. The wavelengths from a multi-carrier source are modulated using double side band (DSB) with a single Mach-Zehnder (MZ) modulator driven by an information signal on a 5 GHz RF carrier. After optical amplification, the modulated wavelengths are optically processed by the beamformer module which is based on fiber Bragg grating (FBG) technology. This module sets the appropriate phase and amplitude on the RF modulated signal of each wavelength to shape the resultant array pattern to the desired pattern. Once modulated, the light is propagated over an ROF distribution link and finally demultiplexed by an arrayed waveguide grating (AWG), detected by PDs and fed to the array elements.

The beamformer module consists of some FBG-based optical filters which do not constitute a TTD system. For a linear uniform antenna array with constant element spacing the steering direction θ_0 can be derived from equation 1.1 as:

$$\theta_0 = \arcsin\left(\frac{c\Delta\varphi}{2\pi d f_0}\right) \quad (1.3)$$

where $\Delta\varphi$ is the amount of interelement phase difference. By using this equation, Figure 1.6 illustrates the achievable beam-steering range versus the inter-element phase tunability for a linear uniform array with half-wave spacing. As we see, for a maximum steering range of 180° , an inter-element phase difference of 2π is required. However, 180° is consi-

sidered an extreme case in beamforming application. Practical beamforming systems have range below 180° .

The signal amplitude configuration of the array elements can be optimized using various methods. The binomial optimization is recognized as a method that provides very low SLL ratio, but wider main lobe [7]. The Dolph-Tchebyscheff method is usually considered as the most complicated and powerful method for any kind of array design [7]. The binomial design technique uses a very aggressive amplitude apodization [7], [16]. For example, an eight-element array with binomial design requires a maximum amplitude attenuation of 16 dB in the RF domain which is equivalent to 8 dB optical attenuation. Therefore, as a rule of thumb, we will consider 10 dB tunability as a design goal.

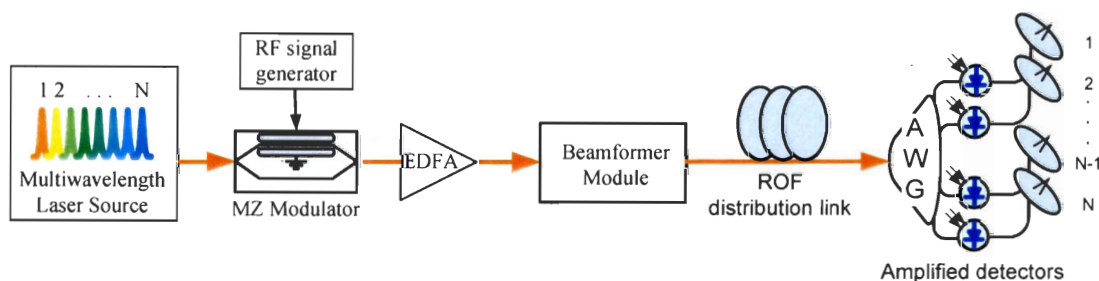


Figure 1-5: Schematic of the proposed ROF link including the beamformer module.

In this chapter, we provided definitions and background that we will need in presenting our research results. We introduced delay and phase manipulations for steering the beam. We explained the general idea behind electrical and optical beamformers. We introduced null-steering beamformer and some of its capabilities in advanced WLAN systems.

For the experimental demonstration of a PAA, rather than using a commercial array antenna, we have fabricated a PAA by microstrip technology as a cheaper and well-matched solution. In the next chapter, we will discuss the design procedure for a single element radiator, its matching technique and introduce related considerations to array fabrication. Since this is not the main contribution of the work, we limit the context to essential notions and we refer the reader to numerous existing references for complementary information.

In the third chapter, we study optical beamforming techniques. First we review some elegant previously proposed ideas in this area, their advantages and disadvantages. Then the heart of this optical null-steering beamformer, the independent control over the phase and amplitude for each channel, is introduced [15]. By describing the method of design and its evolution and then by comparing the simulation and measurement results, we demonstrate the feasibility of this system. The impact of these optical filters on the transmitted signal quality is studied to assure that a null-steering beamformer can transmit signals without adding noise or distorting. For that, we consider the IEEE 802.11 wireless standard as one of the most sophisticated modulation formats commonly used for WLAN applications.

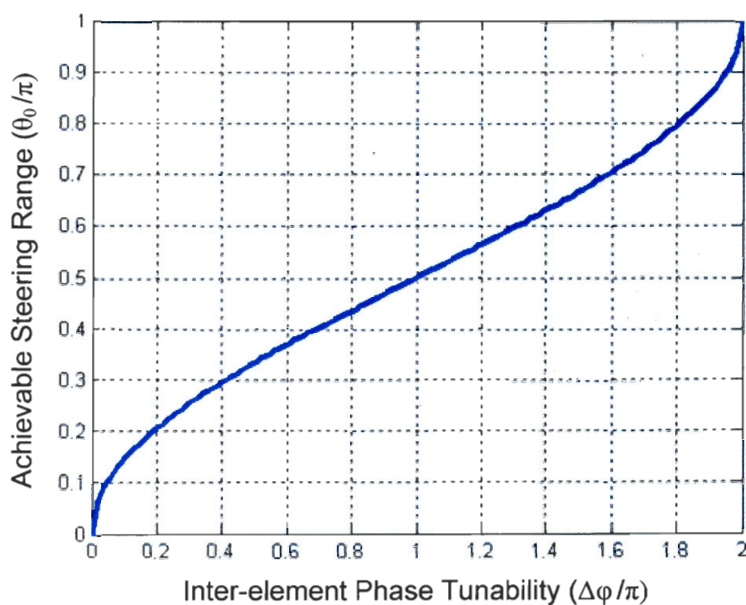


Figure 1-6: Achievable amount of beam-steering range versus the inter-element phase tunability for a linear uniform array with half-wave spacing.

In the last chapter, we will show the pattern measurement results obtained by combining the beamformer to the PAA in an optimized ROF link to prove the concept of null-steering optical beamforming. A discussion about the advantages, disadvantages and future possible efforts for improving this prototype will conclude the results that we have obtained.

Chapter 2

Design and Fabrication of the Antenna

Array

2.1. Introduction

An antenna array is a spatially extended collection of N similar radiators, where N is an integer number higher than 1. The term “similar radiators” means that all the elements have the same polar radiation patterns, orientated in the same direction in three-dimensional space. The elements do not have to be spaced on a regular grid, neither do they have to have the same excitations, but it is assumed that they are all excited with the same frequency and that one can define a fixed amplitude and phase angle for the drive voltage of each

element. In the following paragraphs, we present some basic definitions that will be used frequently in this chapter.

Power Gain: The power gain of an antenna is the ratio of the input antenna power to the output antenna power. This gain is most often expressed in units of dBi, which is a logarithmic gain relative to an omnidirectional antenna. For example, a gain of 12 dBi (also indicated by dBic) means the maximum radiated power by this antenna in a given direction in three-dimensional space is 12 dB more than the radiated power by an omnidirectional one. The same antenna may be used as a transmitting antenna or as a receiving antenna and the antenna gain remains the same in both cases. In the latter case, the gain of a receiving antenna specifies the amount of power it delivers to the receiver with respect to an omnidirectional antenna.

Directivity: The antenna directivity is a measure of the concentration of the radiated power in a particular direction. It may be regarded as the ability of the antenna to direct radiated power in a given direction. It is usually a ratio of radiation intensity in a given direction to the average radiation intensity.

The field pattern associated with an antenna changes with distance and is associated with two types of energy: “radiating energy” and “reactive energy”. Based on them, the space surrounding an antenna can be divided into three regions:

Reactive near-field region: In this region, the reactive field dominates. The reactive energy oscillates towards and away from the antenna, thus appearing as reactance. In this region, energy is only stored and no energy is dissipated. The outermost boundary for this region is at a distance $R_1 = 0.62\sqrt{D_A^3 / \lambda_0}$ where R_1 is the distance from the antenna surface, D_A is the largest dimension of the antenna and λ_0 is the operating wavelength [7].

Radiating near-field region (Fresnel region): This is the region which lies between the reactive near-field region and the far-field region. Reactive fields are smaller in this field as compared to the reactive near-field region and the radiation fields dominate. In this region, the angular field distribution is a function of the distance from the antenna. The outermost

boundary for this region is at a distance $R_2 = 2D_A^2 / \lambda_0$ where R_2 is the distance from the antenna surface [7].

Far-field region (Fraunhofer region): The region beyond $R_2 = 2D_A^2 / \lambda_0$ is the far-field region. In this region, the reactive fields are absent and only the radiation fields exist. The angular field distribution is not dependent on the distance from the antenna in this region and the power density varies as the inverse square of the radial distance [7].

Array factor and array pattern: The polar radiation pattern of a single element is called the “element pattern” and the “array factor” is the polar radiation pattern which would result if the elements were replaced by omnidirectional radiators, having the same amplitude and phase of excitation as the actual elements. If we imagine that all the polar radiation patterns of the elements taken individually are identical (within a certain tolerance) and that the patterns are all aligned in the same direction in azimuth and elevation, then in the far-field region the “array pattern” is derived by multiplying the array factor by the element pattern [7].

To design the array, the first step is to design the appropriate single element. Considering the requirement for low cost, ease in packaging and the 5 GHz band for WLAN application, a microstrip antenna (patch antenna) has been chosen for design and manufacturing. Microstrip antennas can be made to emulate many of different types of antennas but several tradeoffs need to be considered in their design. Because they are manufactured with printed circuit board (PCB) traces on actual PCB boards, they can be very small and lightweight. This comes at the cost of not being able to handle as much radiated power as other antennas. In addition, they are made for very specific frequency ranges, even if in many cases, limiting the frequencies that can be received is actually advantageous to the performance. Due to this characteristic, microstrip antennas are not well suited for wideband communications systems. However, for WiFi and other narrowband purposes, they are the most prevalent solution [16].

In this chapter, at first, we study the formulation of an array patterns to become familiar with the suitable array parameters. Then the design procedure for a single frequency radia-

tor and its matching technique, both based on a microstrip substrate, is discussed. Finally, the measurement results of the S_{11} parameter and the radiation pattern of the fabricated matched antenna are reported.

2.2. Uniformly Excited Linear Arrays

In general, the excitation for each element of an array consists of amplitude and phase. This discrete distribution is often called an aperture distribution, where the discrete array is the aperture. The array pattern is the product of the isolated element pattern and the omnidirectional array factor; this is the “forced excitation” case. To achieve this, the element drives are individually adjusted so that the excitation of each element is exactly as desired. The other case is the “free excitation” situation, where the element drives are all fixed, and the element excitations are those allowed by the scan impedance [17]. Here, the concern will be only with the forced excitation array, where the excitations are constant in amplitude, but may have a scanned phase. To have a uniform and linear configuration, the elements are equally spaced in a row and the inter-element phase differences are all the same.

2.2.1. Pattern Formulations

The radiated field from a linear array is a superposition (sum) of the fields radiated by each element in the presence of the other elements. Following the usual notation, the angular variable, u , that is used in the expression of radiation pattern, can be defined as:

$$u = \sin \theta - \sin \theta_0 \quad (2.1)$$

where: the beam peak is at θ_0 , the angle from broadside is θ and the element spacing is d .

Although the far-field pattern is written as a simple sum of amplitude and exponential phase path length terms, it is convenient to provide a pattern formulation $F(u)$, valid for both even and odd numbers of elements as shown in Figure 2.1:

$$F(u) = \sum_{n=1}^N A_n \exp[jkd(n-1)u] \quad (2.2)$$

where the amplitude excitation coefficients are denoted by A_n , the array has N elements, and $k = 2\pi / \lambda_0$.

For uniform excitation (equal inter-element spacing, same amplitudes, and similar inter-element phase differences) the array pattern has the form [17]

$$F(u) = \exp[j\pi(N-1)u] \frac{\sin \frac{1}{2} Nkdu}{N \sin \frac{1}{2} kdu} \quad (2.3)$$

This inter-element phase shift is $\Delta\phi = kd \sin \theta_0$ given by 1.1. By varying this phase shift, the beam direction, θ_0 , can be scanned to achieve beam-steering.

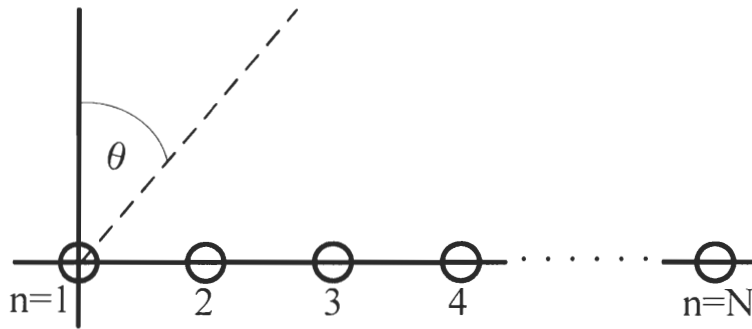


Figure 2-1: Linear array geometry.

2.2.2. Half Power Beamwidth

Half-power-beamwidth (HPBW) is the angular separation between the half-power points on the antenna radiation pattern, i.e., the two points on either side of the maximum, where the gain is one half the maximum value. The half-power points on a uniform array pattern can be computed by solving $\sin \frac{1}{2} Nkdu_{3dB} / N \sin \frac{1}{2} kdu_{3dB} = \sqrt{0.5}$. Increasing the steer angle, θ_0 , will directly increase the HPBW hence pointing the beam at extreme angles broadens the beam and reduces the resultant array directivity. For large arrays, i.e., $N \rightarrow \infty$, the HPBW tends to [17]

$$\theta_{3dB} = \frac{0.886\lambda_0}{Nd \cos \theta_0} \quad (2.4)$$

where by increasing the number of elements, N , we obtain narrower beams and consequently more directivity until the lower limit given in (2.4). Note that the number of side-lobes and the SLL ratio increase with the number of elements [17].

In WLAN applications, eight elements are considered sufficient to provide flexible beam-forming. In this work, as a proof of concept, a four-element array is designed and tested due to the availability of equipment in the laboratory. The proposed approach could be extended to a larger number of elements.

2.2.3. Grating Lobes

We want inter-element spacing to be as large as possible to achieve results higher directivity [17]. However, large spacings between array elements will produce multiple main beams called grating lobes (GL). The larger spacing allows the waves from each element to add in-phase at the GL angles as well as at the main beam angle. For a given main beam angle θ_0 , grating lobes will not appear if the element spacing, d , satisfies [17]

$$d \leq \frac{\lambda_0}{1 + \sin \theta_0} \quad (2.5)$$

We also wish to have an array that can steer the maxima to a range as wide as possible, i.e., $-90^\circ \leq \theta_0 \leq +90^\circ$. We select an inter-element spacing of $d = \frac{\lambda_0}{2}$ to avoid grating lobes in the visible range, to have highest possible directivity and to have maximal steering range.

2.3. Microstrip Patches

Having opted for a PCB implementation of our antennas, we opt for the microstrip antenna form. A microstrip antenna (microstrip patch) is a resonant metallic shape on top of a microstrip conductor. Patches can be in many shapes, but most are rectangular (nearly square) or circular. The polarization and radiation pattern of patches are similar to those of half-

wave dipoles [7]. The zero-order pattern for a rectangular patch with width W and length L is given by [16]:

$$E_x = \cos\theta \cdot \cos\frac{kWs}{2} \cdot \frac{\sin\frac{kLq}{2}}{\frac{kLq}{2}} \quad (2.6)$$

where $s = \sin\theta \cdot \cos\phi$ and $q = \sin\theta \cdot \sin\phi$ while θ and ϕ denote elevation angle and azimuth angle respectively. For a circular patch of radius a , with $\beta = ka \sin\theta$, the zero-order pattern has the form of [16]:

$$E_x = \cos\theta [J_0(\beta) - \cos(2\phi)J_2(\beta)] \quad (2.7)$$

where J_0 and J_2 are Bessel functions of the first kind of order zero and two, respectively.

2.3.1. Advantages and Disadvantages

Microstrip antennas are increasing in popularity for use in wireless applications due to their low-profile structure. That makes them suitable for portable wireless devices such as cellular phones and laptops. They have been also used successfully in military applications and satellite communications [20]. Their principal advantages are: light weight, small volume, low fabrication cost, support of both linear and circular polarization, integratability with microwave integrated circuits (MIC), capability for dual and triple frequency operation, and mechanical robustness when mounted on rigid surfaces [18].

Microstrip patch antennas also suffer from a number of disadvantages compared to conventional antennas. Some of their major disadvantages discussed in [18] are narrow bandwidth, low efficiency and gain, extraneous radiation from feedline and junctions, and low power handling capacity.

Microstrip antennas have a high quality factor (Q) as a resonator. The Q -factor is inversely proportional to the losses associated with the antenna and a large Q -factor leads to narrow bandwidth and low efficiency. The Q -factor can be reduced by increasing the thickness of the dielectric substrate. But as the thickness increases, an increasing fraction of the total

power delivered by the source is diverted to the surface wave [16]. This surface wave contribution can be considered as an unwanted power loss since it is ultimately scattered at the dielectric bends and results in degradation of the antenna characteristics. Drawbacks such as low gain and low handling power capacity can be overcome in the array configuration.

2.3.2. Feed Techniques

Microstrip antennas may be fed by a variety of techniques, either “contacting” or “non-contacting”. In the contacting category, the RF power is fed directly to the radiating patch using a connecting element such as a microstrip line or coaxial cable. In the non-contacting scheme, electromagnetic field coupling is used to transfer power between the microstrip line and the radiating patch [18], [20]. The contacting feed technique was used due to equipment availability. The contacting scheme can be implemented in two common ways.

Microstrip Line Feed: In this feed technique (Figure 2.2), a conducting strip is connected directly to the edge of the microstrip patch. The width of the strip is smaller compared to the radiator and can be etched on the same substrate to provide a planar structure. This is a convenient feeding scheme, due to ease of fabrication and simplicity in modeling. However, as the thickness of the dielectric substrate increases, surface waves and spurious feed radiation also increase [16].

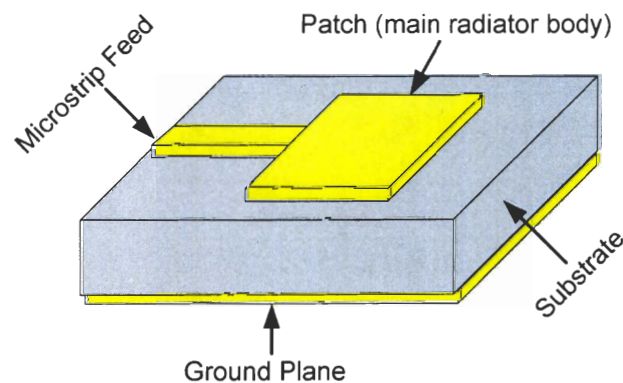


Figure 2-2: Microstrip line feed schematic.

Coaxial Feed: The coaxial feed or probe feed is another common technique used for feeding microstrip antennas. As we see in Figure 2.3b, the inner conductor of the coaxial connector extends through the dielectric and is soldered to the radiator, while the outer conductor is connected to the ground plane. The main advantage of this type of feeding scheme is that it has low spurious radiation. However, its main disadvantages are that it has narrow bandwidth and is problematic to model as it is not planar (a hole has to be drilled in the substrate and the connector protrudes outside the ground plane). For thicker substrates, the increased probe length also leads to a more inductive input impedance and matching problems [16], [18].

In the next section, we will see that by increasing the substrate thickness, the antenna bandwidth increases linearly, however, as was discussed, for a thick dielectric substrate both the microstrip line feed and the coaxial feed suffer from numerous weaknesses. The non-contacting feed techniques can solve some of these troubles.

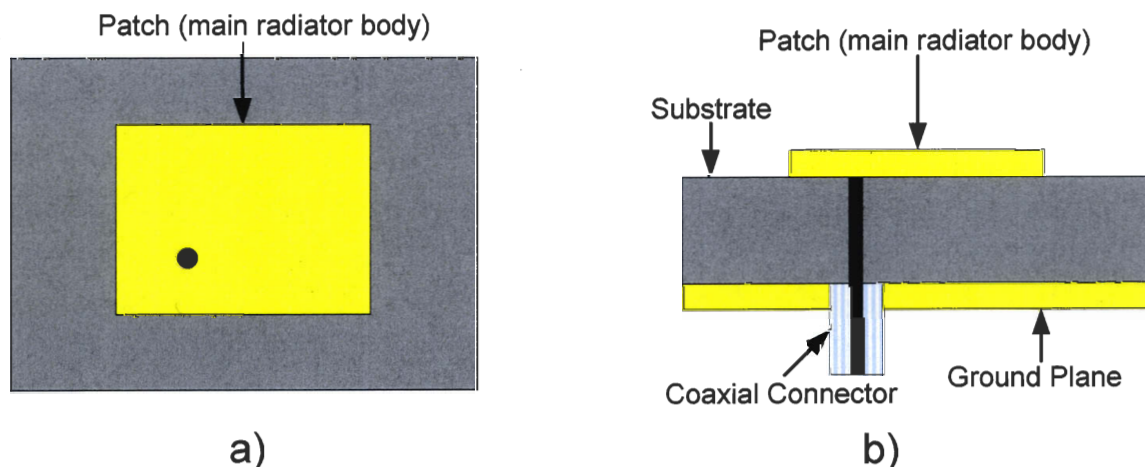


Figure 2-3: Schematic of coaxial feed.

2.3.3. Transmission-Line Model

In this section we present equations describing relationships between PCB material (dielectric constant ϵ_r and substrate height h), the system carrier frequency f_0 , and the physical characteristics of the patch (length L and width W). In Section 2.4.1, we describe our choice

of substrate, and in Section 2.4.2 we deduce the physical dimensions for our antenna design.

The best-known models for the analysis of microstrip antennas are the transmission line model, cavity model, and full wave model [16]. The transmission line model is the simplest of all and it results in good physical insight but it is less accurate. The cavity model is more accurate and gives good physical insight but is complex. The full wave model is extremely accurate, versatile and can treat arbitrarily shaped elements and couplings. The full wave model gives less insight as compared to the other two models and is far more complex in nature. Considering our need for a simple, single-frequency rectangular antenna and the limited fabrication accuracy in layout printing on the substrate and presumed design parameters, the transmission line model is sufficient for our design.

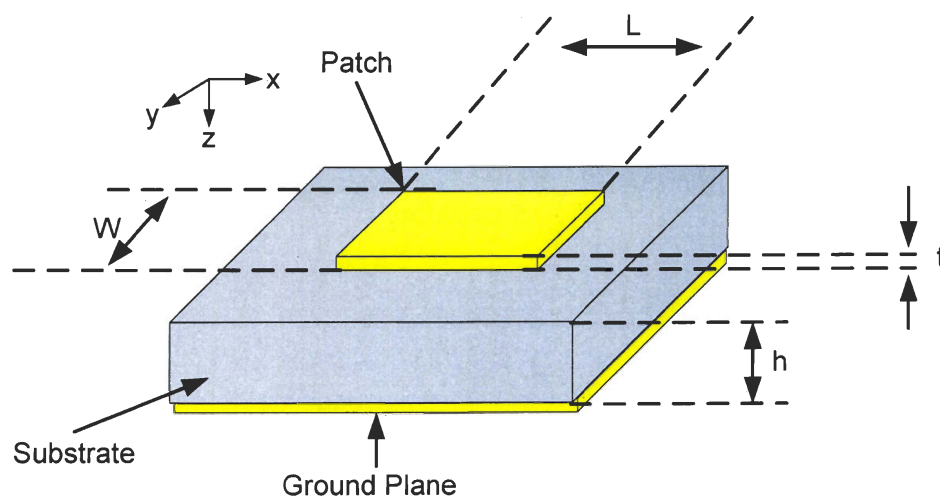


Figure 2-4: Structure of a rectangular microstrip antenna.

The microstrip is essentially a non-homogeneous transmission line with two dielectrics: the substrate and air. Hence, most of the electric field lines reside in the substrate, with parts of some lines in the air. As a result, this transmission line cannot support pure transverse-electric-magnetic (TEM) mode of transmission; it is a strip waveguide and the phase velocities in the air and the substrate are different, making boundary conditions impossible to meet. Instead, the dominant mode of propagation is the quasi-TEM mode of TM_{10} . Thus an

effective dielectric constant (ϵ_{reff}) must be found to account for both the fringing and the wave propagation in the line. The value of ϵ_{reff} is slightly less than ϵ_r , because the fringing fields around the periphery of the patch are not confined in the dielectric substrate but also extend in the air. Consider Figure 2.4, which shows a rectangular microstrip antenna of length L and width W embedded on a substrate of height h . The co-ordinate system is such that the length is along the x direction, width is along the y direction, and the height is along the z direction. The expression for ϵ_{reff} for the TM_{10} mode is [7]

$$\epsilon_{\text{reff}} = \frac{1}{2}(\epsilon_r + 1) + \frac{\epsilon_r - 1}{2\sqrt{1 + 12h/W}} \quad (2.8)$$

In order to operate in the fundamental TM_{10} mode, the length of the patch must be slightly less than $\lambda/2$ where λ is the wavelength in the dielectric medium and is equal to $\lambda_0 / \sqrt{\epsilon_{\text{reff}}}$, where λ_0 is the free space wavelength. The TM_{10} mode implies that the field varies by one $\lambda/2$ cycle along the length, and there is no variation along the width of the patch.

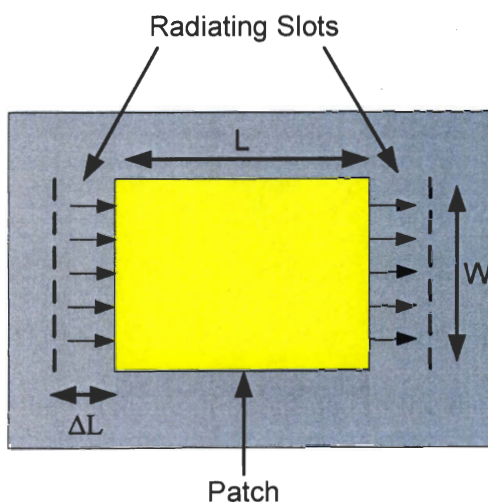


Figure 2-5: Electric field lines.

In Figure 2.5, the microstrip antenna is shown from the top, open circuited at both ends across the length. Along the width of the patch, the voltage is maximum and current is

imum due to the open ends. The fields at the edges can be resolved into normal and tangential components with respect to the ground plane. The normal components of the electric field at the two edges along the width ($x = -\frac{L}{2}$ and $x = +\frac{L}{2}$) are in opposite directions and thus out of phase since the patch is $\lambda/2$ long; they cancel each other in the broadside direction. The tangential components are in phase, meaning that the resultant fields combine to give maximum radiated power normal to the surface of the structure. Thus, the edges along the width can be represented as two radiating slots, which are $\lambda/2$ apart and excited in phase and radiating in the half space above the ground plane. Considering Figure 2.5, the effective length of the patch L_{eff} now becomes

$$L_{eff} = L + 2\Delta L \quad (2.9)$$

The ΔL parameter has been empirically derived as [19]

$$\Delta L = 0.412h \frac{(\epsilon_{reff} + 0.300)(W/h + 0.262)}{(\epsilon_{reff} - 0.258)(W/h + 0.813)} \quad (2.10)$$

For a rectangular microstrip antenna, the resonance frequency for any TM_{mn} mode is [7]

$$f(m, n) = \frac{c}{2\sqrt{\epsilon_{reff}}} \left[\left(\frac{m}{L_{eff}} \right)^2 + \left(\frac{n}{W_{eff}} \right)^2 \right]^{\frac{1}{2}} \quad (2.11)$$

where m and n are modes along L_{eff} and W_{eff} respectively. Since there is no field variation along the width for TM_{10} mode, the values of W_{eff} and W are equal. By solving (2.11) for $m=1$ and $n=0$ (the dominant mode of TM_{10}), the effective length is related to $f_0 = f(1,0)$ by

$$L_{eff} = \frac{c}{2f_0\sqrt{\epsilon_{reff}}} \quad (2.12)$$

For efficient radiation, the width W is suggested by Bahl and Bhartia [20] as:

$$W = \frac{c}{2f_0 \sqrt{\frac{(\epsilon_r + 1)}{2}}} \quad (2.13)$$

Hence, by using equation 2.8, 2.9, 2.12 and 2.13, one can easily find the appropriate dimensions for a single frequency radiator based on the transmission line model. The fractional bandwidth for the resultant rectangular microstrip antenna, for a voltage standing wave ratio (VSWR) less than 2, can be approximated by [16]

$$BW \cong \frac{4h}{\sqrt{2\epsilon_r} \lambda_0} \quad (2.14)$$

This equation states that the bandwidth is proportional to substrate thickness and inversely proportional to the square root of the dielectric constant.

2.4. Microstrip Antenna Design and Fabrication

A single element design has three steps. First an appropriate substrate is selected based on the operating frequency and application. Next, the dimensions of the radiator main body must be determined. Finally, the input impedance of the radiator must be matched to deliver the highest possible power to the antenna.

2.4.1. Substrate Selection

One of the most important tasks in microstrip design is the selection of an appropriate substrate material. The major electrical properties to consider are relative dielectric constant and loss tangent. A high dielectric constant results in a smaller patch, but generally reduces bandwidth (2.14) and requires tighter fabrication tolerance. A high loss tangent reduces antenna efficiency and increases feed losses. Generally, it is best to select a substrate with the lowest possible dielectric constant consistent with the physical space available on the PCB for the antenna. Substrate thickness should be chosen as large as possible to maximize bandwidth (2.14) and efficiency, but not so large as to risk surface wave excitation. As a rule of thumb, for maximum operating frequency f_0 the thickness should satisfy [16]

$$h \leq \frac{0.3c}{2\pi \cdot f_0 \sqrt{\epsilon_r}} \quad (2.15)$$

For example, for our design we require an antenna operating at the resonant frequency of 5 GHz; the maximum allowable thickness is 1.7 mm for a substrate having a dielectric constant of 3. In addition, if the system must operate within a narrow frequency band, dielectric constant uniformity and stability will be important; a variable ϵ_r will cause the patch frequency to wander and can reduce efficiency.

Traditional patch design at microwave frequencies uses substrates such as alumina, quartz and PTFE [7], [20]. These substrates offer excellent electrical performances but the costs are often too high for commercial applications. Epoxy FR4 is a widely used low-cost material for frequencies below about 1 GHz or so. Low-cost commercial RF designs need substrates that combine the previously-mentioned advantages. RO4230™ high frequency laminate is one of these low-cost commercial substrates from “Rogers Corporation” specially produced for high frequency wireless application [21]. This ceramic filled, glass reinforced hydrocarbon-based material provides the controlled dielectric constant, low loss performance and excellent passive intermodulation response required for mobile infrastructure microstrip antenna applications. Moreover, the material is halogen free and meets common worldwide “green” standards! This substrate is fully compatible with conventional FR4 processing and does not require any of the special treatment needed for PTFE-based laminates in the hole preparation process. This laminate is an affordable alternative within the 40 GHz band, thus allowing designers to maximize the price and performance of antennas.

The resin system of RO4230™ dielectric material is designed to provide the necessary thermo-mechanical properties for ideal antenna performance. The thermal coefficient of expansion in both the x and y directions are similar to that of copper. This attribute minimizes the thermal effects of environmental conditions and reduces stresses that can lead to warpage of the printed circuit board antenna [21].

In addition to excellent thermo-mechanical performance, RO4230™ laminate embodies electrical characteristics that antenna designers need. The laminate has a dielectric constant

of 3 ± 0.05 and a loss tangent of 0.0020 measured at 5 GHz. These values allow antenna designers to realize substantial gain values while minimizing signal loss [21].

2.4.2. Radiator Element Design

In this section, we examine the design procedure of a single element radiator. We start by specifying the operating parameters such as operational frequency (f_0), dielectric constant (ϵ_r) and height of the substrate (h). The resonant frequency of the antenna must be selected appropriately. For transmitting IEEE 802.11a signal, according to the protocol, we have two choices: 2.4 GHz or 5 GHz. Considering the beamformer design is for 5 GHz band operation, we selected a resonant frequency of $f_0 = 5$ GHz. The RO4230™ has been chosen as the dielectric material with dielectric constant of $\epsilon_r = 3$ and dielectric height of $h = 1.524$ mm which satisfy the condition of (2.15).

Using these basic parameters and employing the transmission line model, we then proceed to determine the dimension of the antenna:

Step 1: Having selected $\epsilon_r = 3$ and $f_0 = 5$ GHz, we calculate the radiator width (W) using equation (2.13):

$$W = \frac{c}{2f_0 \sqrt{\frac{(\epsilon_r + 1)}{2}}} = 21.2 \text{ mm}$$

Step 2: Having selected $h = 1.524$ mm, the effective dielectric constant (ϵ_{reff}) from (2.8), is:

$$\epsilon_{\text{reff}} = \frac{1}{2}(\epsilon_r + 1) + \frac{\epsilon_r - 1}{2\sqrt{1 + 12h/W}} = 2.732$$

Step 3: The effective length (L_{eff}) is found from (2.12):

$$L_{\text{eff}} = \frac{c}{2f_0 \sqrt{\epsilon_{\text{reff}}}} = 18.1 \text{ mm}$$

Step 4: The length extension (ΔL) is found from (2.10):

$$\Delta L = 0.412h \frac{(\epsilon_{\text{reff}} + 0.300)(W/h + 0.262)}{(\epsilon_{\text{reff}} - 0.258)(W/h + 0.813)} = 0.98 \text{ mm}$$

Step 5: The length of the patch (L) is found from (2.9):

$$L = L_{\text{eff}} - 2\Delta L = 16.2 \text{ mm}$$

Step 6: The transmission line model is only valid for infinite ground planes. However, practically we have a finite ground plane. It has been shown in [18] that similar results for finite and infinite ground plane can be attained if the size of the ground plane is approximately three times greater than the patch dimensions of the substrate thickness all around the periphery. Hence, for this design, the minimum ground plane dimensions should be greater than:

$$L_g = 6h + L \approx 26 \text{ mm}$$

$$W_g = 6h + W \approx 31 \text{ mm}$$

In the fabrication process we devoted a larger surface for the ground plane to make sure that the L_g and W_g conditions are met.

2.4.3. Impedance Matching

For the radiator to transmit the signal at 5 GHz, the signal should be fed efficiently to the antenna. Impedance matching to antennas can be achieved using different techniques such as external electronic circuits, external microstrip circuits, dual or triple matching stubs, quarter wave section, etc. We impedance matched the antennas without using any extra circuit or device simply by optimizing the connection. As we discussed in Section 2.3.2, for a two-layer patch design, two methods, both belonging to the “contacting” category, are prevalent: coaxial feed and microstrip feed. So the goal will be to perfectly match the characteristic impedance of the feedline or coaxial probe with the input impedance of the antenna at the contact point.

The first technique, coaxial feed, requires a perpendicular connection between the center pin of the coaxial cable and the radiator body (see Figure 2.3b). The hole position is selected in such a way to guarantee an input impedance equal to the characteristic impedance of the coaxial cable, which is usually 50Ω . However, the implementation is problematic as great precisions is required in the hole fabrication; also symmetric soldering is required to achieve a good matching response.

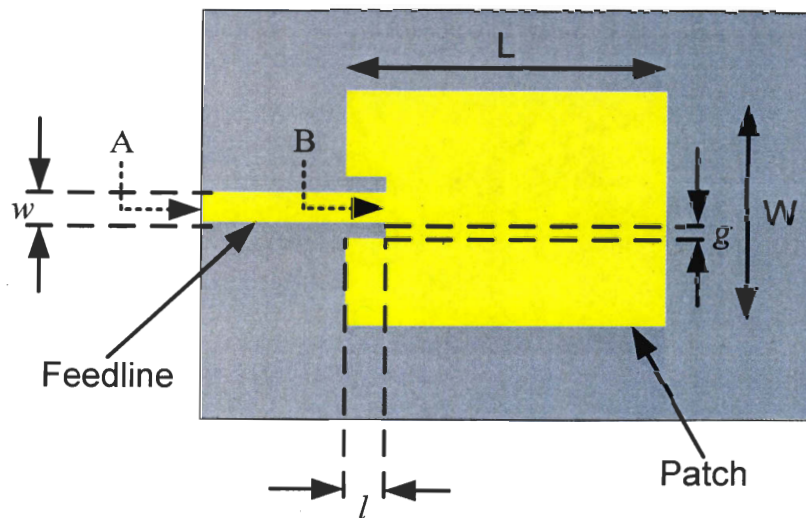


Figure 2-6: Matching parameters.

The other technique, microstrip feed, has been chosen, as depicted in Figure 2.6. For microstrip feed impedance matching, further parameters must be determined: microstrip feedline width (w), the amount of inset (l) and the amount of separation between microstrip line and radiator body (g). The purpose of the inset cut in the patch is to match the impedance of the feedline to the patch without the need for any additional matching circuit or element. This is achieved by proper control over the inset position. Knowing that the SMA cables and connectors have the characteristic impedance of 50Ω , the input impedance of the feedline must be 50Ω at the connection point with the coaxial cable (Point A in Figure 2.6). From here the microstrip feedline width (w) is determined and it will consequently force the amount of inset (l) to be chosen in a way to provide the input impedance of 50Ω at the connection point with radiator body (Point B in Figure 2.6).

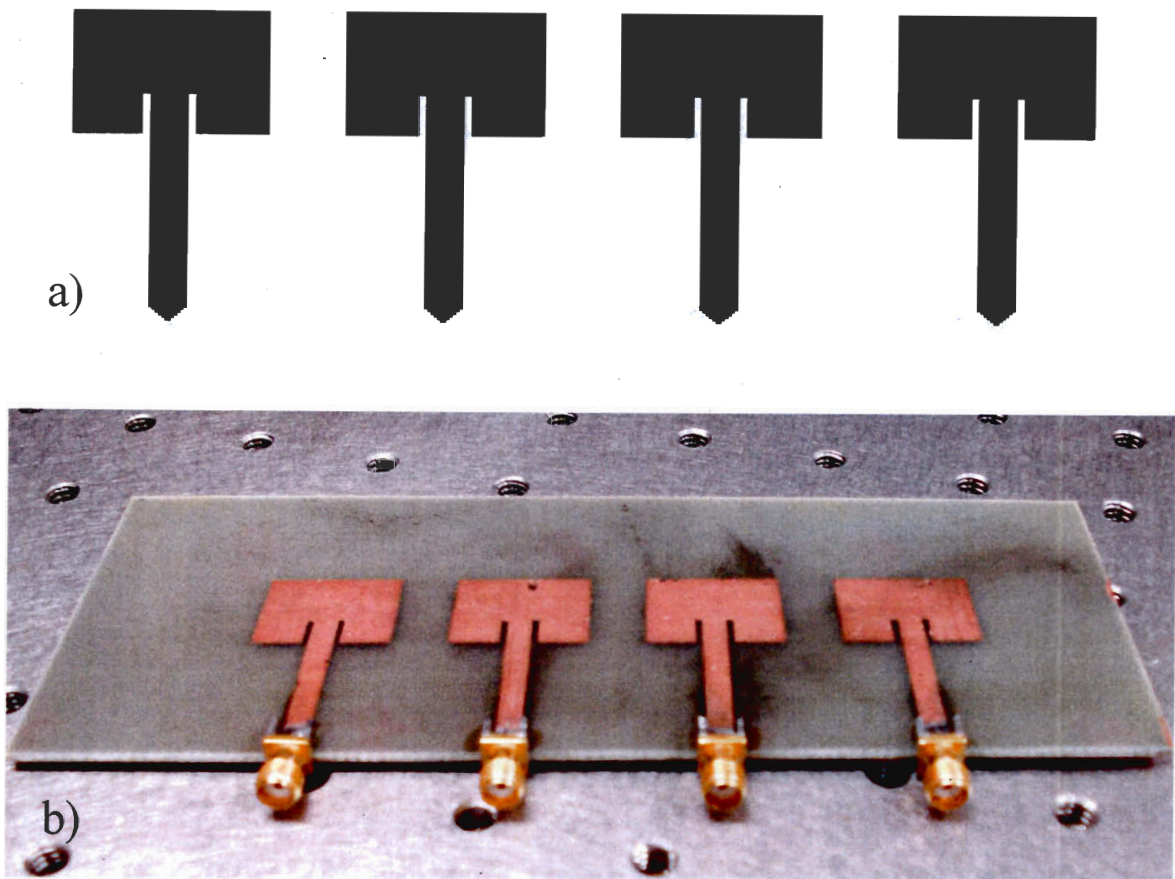


Figure 2-7: Array layout for printing over the substrate (a) and the fabricated home-made array (b).

The characteristic impedance of a microstrip line can be calculated, knowing the width of w and substrate thickness of h , as [16]

$$Z_0 = \frac{60}{\sqrt{\epsilon_{\text{reff}}}} \ln\left(\frac{8h}{w} + \frac{w}{4h}\right) \quad \text{for } \frac{w}{h} \leq 1$$

$$Z_0 = \frac{120\pi}{\sqrt{\epsilon_{\text{reff}} [w/h + 1.393 + 0.667 \ln(w/h + 1.444)]}} \quad \text{for } \frac{w}{h} \geq 1 \quad (2.17)$$

This equation gives a width of 3.8 mm for the feedline to meet the 50 Ω characteristic impedance condition for RO4230™ material. A trial and error method is used to find the inset value at point B using commercial software [16]: for different inset amounts, the return loss (RL) is computed and the inset amount giving the most negative RL is selected. According

to [16], there exists a point along the length of the patch where the RL is minimum. The simulation leads to 5.5 mm as the amount of inset for $f_0 = 5$ GHz.

With an inset around the feedline, some gap, g in Figure 2.6, must be used to isolate the line from the patch. There are no particular guidelines for this. As an approximate rule-of-thumb, a spacing of 0.1 to 0.5 of the line width is suggested [20]. Wide lines have more field concentrated under the line; thus narrow spacings are appropriate. Conversely narrow lines should have wider spacings. For all cases, the combination of feed and gap width should be less than 25% of the patch width to avoid blockage [20]. In our design, we use $g = 1$ mm to satisfy these conditions.

Up to this point, we have determined the general antenna design for operating at a single frequency to achieve acceptable transmitting or receiving characteristics. However, by joining the feedline to the radiator main body, the feedline will act as a part of the radiator, affecting the resonant frequency. To have a more precise design, we should consider the microstrip feedline as a part of the antenna resonance system. This correction requires an advanced simulation, which was performed using commercial software [16]; we obtained: $L = 16.43$ mm, $W = 21.2$ mm, $g = 1$ mm, $l = 5.5$ mm and $w = 3.8$ mm.

By comparing these values to the proposed design parameters in Section 2.4.2, we find only one difference: the length of the radiator is increased from 16.2 mm to 16.43 mm.

Finally, to connect the pin of a coaxial cable to the feedline, perfect soldering is indispensable. We found empirically that by tapering the feedline at the connection point with SMA probe (Point A in Figure 2.6), we can achieve better matching and consequently lower RL. This tapering, shown in Figure 2.7a, ensures that the current distribution over the width of the feedline is monotonic.

2.4.4. Array Fabrication

To fabricate the array antenna, we put several single elements beside each other with the appropriate spacing. As we already discussed, for the best performance, maximum steering capability and diminishing grating lobes in the visible area, a spacing of $\lambda_0/2$ is recommended. For 5 GHz operation, this value is 3 cm. Figure 2.7a depicts the layout of the four-

element array based on design parameters calculated in Sections 2.4.2 and 2.4.3. To make the array, based on the available facilities in the laboratory, the following procedure was established by Mr. Patrick LaRochelle, a technician at COPL:

Step 1: The array was imprinted with black ink on one side of the substrate on the copper layer. To do this, Figure 2.7a was printed on photo-paper and then ironed over the substrate; the ink was transferred onto the copper.

Step 2: The whole substrate was immersed in ferric chloride to remove the unwanted copper layer around the antennas and feedlines. We immersed the copper board in the solution and agitated it until the etching action was completed. Ferric chloride normally can etch up to a maximum of 100 g of copper per liter of solution. The etching process can be sped up by heating the solution to a temperature no higher than 55° C (135° F). Before the immersing process, we protected the copper of the rear side of the substrate (the ground side) by wrapping it in scotch tape.

Step 3: After completing the etching process, the scotch tape was removed from the ground layer, and SMA connectors were soldered on.

2.4.5. Experimental Results for our Designed and Fabricated Array

Scattering parameters, also called S-parameters, describe the performance of linear, time-invariant microwave networks. An N -port microwave network has N arms into which power can be fed and from which power can be taken. In general, power can get from any arm (as input) to any other arm (as output). We also observe that power can be reflected by a port, so the input power to a single port can partition between all the ports of the network to form outgoing waves. S-parameters are conceptually simple, analytically convenient and capable of providing detailed insight into a measurement and modeling problem. A single antenna can be considered as a one-port microwave network and the S_{11} parameter denotes its input reflection coefficient. Lower S_{11} results in lower RL that increases the efficiency of the antenna.

Figure 2.8 shows the measured and simulated traces of S_{11} for the designed microstrip antenna. For simulation, we observed the impact of carrier frequency on the input impedance of the antenna and consequently we calculated the S_{11} parameter. The measurement has been taken with an Agilent RF network analyzer with model number of E5070B after a full electrical calibration. The result shows an acceptable agreement with simulation results. The slight difference between the center frequencies may come from the design uncertainties and manual fabrication. The S_{11} depth of this home-made design at the center frequency, -17 dB, shows it is successfully matched for single-frequency operation.

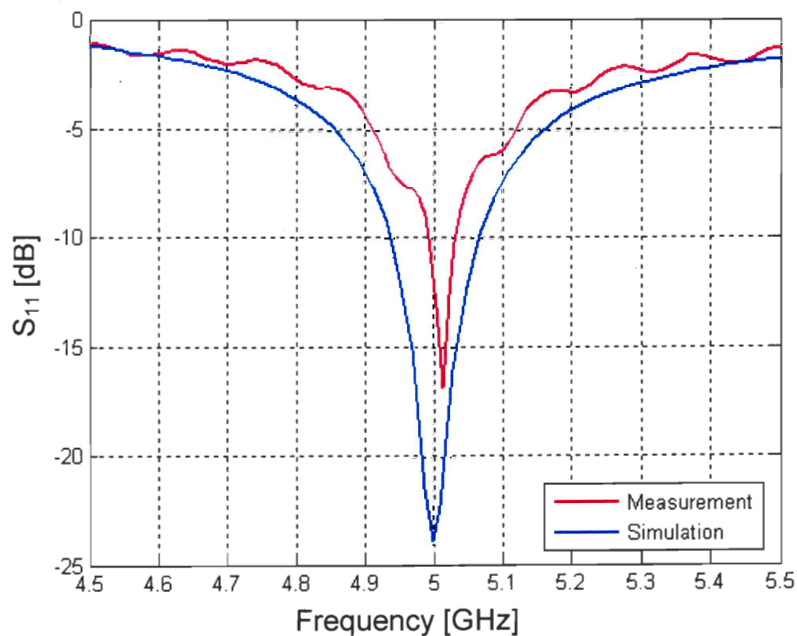


Figure 2-8: S_{11} measurement (red trace) and simulation (blue trace) comparison for home-made antenna.

Figure 2.9 shows the radiation pattern measurement result for a single-element rectangular antenna designed and fabricated as described previously. Considering the two-layer design, a 180° angular range covered the front side of the antenna. The other 180° angular range, facing the rear side of the antenna, does not radiate as it is grounded. The pattern measurement setup was based on a rotating transmitter and a fixed receiver. We fixed a single transmitting antenna, on a plate connected to the shaft of a stepper-motor. Another single

antenna (similar to the transmitter element) was used for reception. Both transmitter and receiver have the same height (1 m) from the floor. We placed the transmitter and receiver antennas at 1 m distance to meet the far-field range criterion and to reduce the impact of reflections. We rotated the transmitter side for 180 steps covering 180° of the front side of the antenna; for each step the received RF power in the receiver was measured by a signal analyzer and saved. The speed and delay time for each rotation step were chosen empirically in support of stable power acquisitions.

The asymmetry in the pattern is normal for microstrip antennas and has been reported in [18] and [20] as one of the patch drawbacks. Although the pattern in Figure 2.9 is not perfectly omnidirectional, the array formed from multiple copies of this antenna can be used for our beamforming experiment. It is worth mentioning that for obtaining the array factor, we normalize the measured array pattern to the single-element pattern, therefore we can get rid of the asymmetry and directionality, seen in Figure 2.9. Some large ripples on the pattern are noticeable. These ripples may come from the imperfect properties of the anechoic chamber we manually set up around transmit and receive antennas.

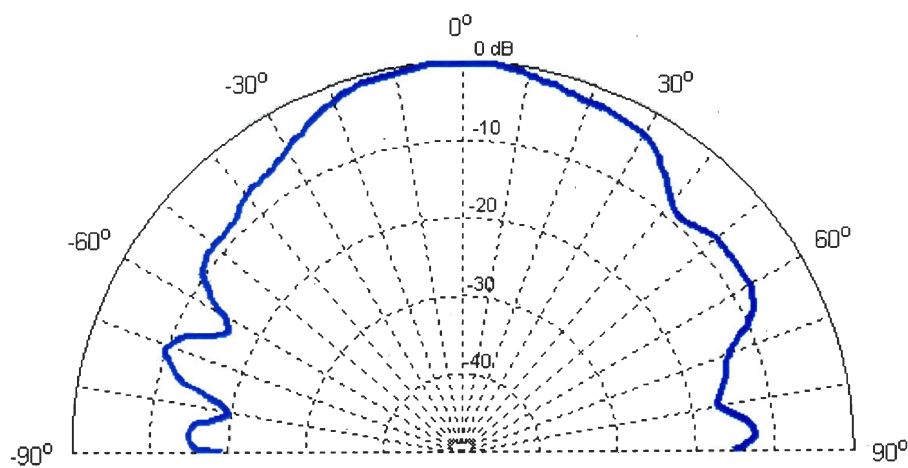


Figure 2-9: Pattern measurement of a single element home-made microstrip antenna.

2.5. Conclusion

In this chapter we introduced definitions and the array formulations that we will use to describe the PAA parameters. Afterward, we briefly explained the transmission line model for designing a single-element patch antenna operating at a single frequency. Then by using this model the appropriate antenna was designed and matched for our specific application. Finally, by measuring the radiation pattern and S_{11} parameter, we examined the radiation and matching qualities, respectively. In the last chapter, we use this array antenna as a part of ROF link to demonstrate the optical null-steering beamforming.

Chapter 3

Optical Beamforming Techniques

3.1. Introduction

Array antennas are becoming increasingly important in mobile communications because they allow for dynamic and fast shaping of the antenna radiation diagram without the use of mechanical parts. The flexibility in designing the shape of the radiation pattern depends on the number of degrees of freedom available in the array: amplitude and phase control allow for a more flexible design of the radiation pattern than phase alone.

Drawbacks for widespread application of all-electronic control of the amplitude and phase of antenna elements include cost, complexity, size, weight, loss, and susceptibility to elec-

tromagnetic interference. Photonics holds great promise for alleviating these problems, and enables the use of antenna remoting and optical signal processing. So-called true time delay optical beamformers feature wideband operation with flat frequency response, potentially limited only by the bandwidth of photodetectors and modulators. However, for low bandwidth applications simpler techniques based on phase manipulation may be of interest. Most of these optical beamformers, including our proposed optical null-steering beamformer, are based on FBG technology because of the ease in integration with ROF link and low-cost manufacturing.

In this chapter, first we briefly introduce a FBG and some of the associated definitions that we will need to describe our research. We review some previous research on optical beamforming and discuss their performance. Then the null-steering beamformer which requires independent control over the phase and amplitude is introduced. We first describe the concept, the design and its evolution. By comparing simulation and measurement results, we demonstrate the feasibility of our design and we experimentally study the effect of this beamformer on signal quality. For that purpose, we observe the transmission quality of an IEEE 802.11a signal, as one of the most sophisticated modulation formats commonly used for WLAN applications. Lastly, the impact of beam squint on the radiation pattern will be simulated and discussed.

3.2. Fiber Bragg Grating Technology

A FBG is an optical fiber in which the refractive index in the core is perturbed forming a periodic or quasi-periodic index modulation profile. A narrow band of the incident optical field within the fiber is reflected by successive, coherent scattering from the index variations. The maximum mode coupling or reflection occurs when the Bragg condition is fulfilled, as [22]

$$\lambda_B = 2n_{eff}\Lambda \quad (3.1)$$

where λ_B is the Bragg wavelength, n_{eff} is the effective modal index and Λ is the perturbation period.

The refractive index profile of the grating may be modified to add other features, such as a linear variation in the grating period, called a chirp. The chirp has the effect of broadening the reflected spectrum. In this case, the Bragg wavelength will change along the fiber following the change in the grating period. A grating with a non-zero chirp has the property of adding dispersion, meaning that different wavelengths reflected from the grating will be subject to different delays. This property is used in the development of delay lines for PAA systems and dispersion compensators as well.

If the strength of the index modulation in a grating is constant over some length, and suddenly drops to zero outside that range, the reflection spectrum exhibits side-lobes which may be disturbing sometimes. They can be largely removed with the technique by apodizing the grating, i.e., the strength of the index modulation is smoothly ramped up and down along the grating. Of course, one then needs to increase the overall length of the grating to achieve a certain peak reflectivity. In an apodized fiber Bragg grating, there is a tradeoff between optimum side-lobe suppression and maximum reflectivity for some restricted grating length and a given maximum strength of index modulation.

FBGs are created by inscribing or writing the periodic variation of the refractive index into the core of an optical fiber using an intense ultraviolet (UV) source, such as a UV laser, thanks to the photosensitivity characteristic. Photosensitivity means that exposure of UV light leads to a permanent rise in the refractive index of certain doped glasses. Typical values for the index change are ranging between 10^{-6} to 10^{-3} , depending on the UV exposure and the dopants in the fiber. By using techniques such as hydrogen loading, an index change as high as 10^{-2} can be obtained. Fiber gratings are nowadays usually fabricated by a variant of the transverse holographic method [22]. By exposing the fiber to a UV interference pattern from the side, the pattern is printed into the fiber as seen in Figure 3.1. Only the core is usually doped (for example with germanium), and consequently the grating is only formed in the core and not in the cladding.

Because a FBG can be designed to have an almost arbitrary, complex reflection response, it has a variety of applications. In telecommunications, the use of FBG-based devices is very popular since they have low insertion loss, allow low-cost manufacturing and are compatible with existing optical fibers used in telecommunication networks. Probably the most

promising applications have been dispersion compensation, wavelength selective devices and tunable delay lines for beamforming applications [22].

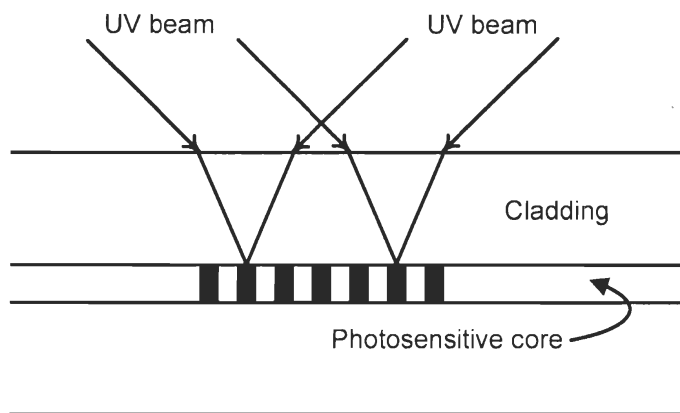


Figure 3-1: The transverse holographic method for writing fiber gratings. Two coherent UV beams produce an interference pattern in the fiber. The periodicity of the resulting grating is dependent on the angles of the incident beams.

3.3. Optical Beamforming Methods

The first optical beamforming approaches were based on a number of uniform FBGs written at different positions; the distances between gratings determine the beam pointing direction of the array antenna [23], [24]. This system assures broadband operation, but it only allows a discrete number of steering angles.

Subsequently, it was demonstrated that chirped fiber Bragg gratings (CFBG) can produce a linear phase change of the modulating signal at microwave frequencies, and the slope of the phase response can be continuously modified by tuning the wavelength of the optical carrier [25], [26]. Broadband operation and continuous spatial scanning properties have been demonstrated with these systems. However, these systems are very complicated, as they need the use of a tunable laser source (TLS) and tunable bandpass filters that should be tuned synchronously.

To eliminate these disadvantages, a variable time-delay line has been used for a PAA system, which applies strain perturbation at different positions of a uniform FBG to induce different time delays via tuning different position of the grating [27]. The system operates at a

single fixed optical wavelength, but the minimum delay step is limited to about 10 ps by the minimum available distance between the adjacent perturbations. This solution was modified in [28] and the minimum delay step was reduced to 1 ps.

3.3.1. TTD Beamforming Using a Fiber Grating Prism

Reference [29] presented, for the first time, measured data on a FBG-based, TTD processor for beamforming in both transmit and receive modes. Measurements were taken over a 3.5 GHz bandwidth. The system level diagram for the beamformer is shown in Figure 3.2. For the transmit mode of operation, one TLS is externally modulated with an EOM. This modulated light feeds a group of N single-mode fibers through an equal-path 1: N power divider. The receive EOMs are not used in the transmit mode, and optical circulators are used to direct the modulated signals to the fiber grating prism (FGP). Each fiber includes a spatially distributed array of FBGs which collectively form the FGP. The different peak reflection wavelengths of the different gratings are within the tuning range of the laser. The 1: N splitter includes a N -fold set of integrated 3 dB directional couplers that gather the back-traveling light from the wavelength selective gratings. Reflected light is time-delayed in accordance with the particular grating which is addressed based on the selected wavelength. For the transmit mode, a second set of equal-length fibers transports the N coupler outputs to a set of PDs located to feed the antenna elements with delayed microwave signals. In the receive mode an unmodulated TLS feeds N optical channels. The received microwave signals are directed to a set of N EOMs. The modulated optical signals are then directed to the FGP via the optical circulators. These optical signals are summed together and sent to a PD for recovery of the collective microwave signal. Wavelength shift in the TLS selects a desired outgoing as well as incoming beam direction.

Figure 3.2 also illustrates the spatial layout of the fiber prism for the case of a four-element array ($N=4$). Here, the main lobe of the PAA can point in any one of five discrete directions ($M=5$) as selected by the laser wavelength. In [29], the experimental result for time delay response of the system for the case of $N = 3$ and $M = 4$ is reported for the maximum steering range of 120° within a 3.5 GHz bandwidth. However, they did not measure or simulate the radiation pattern.

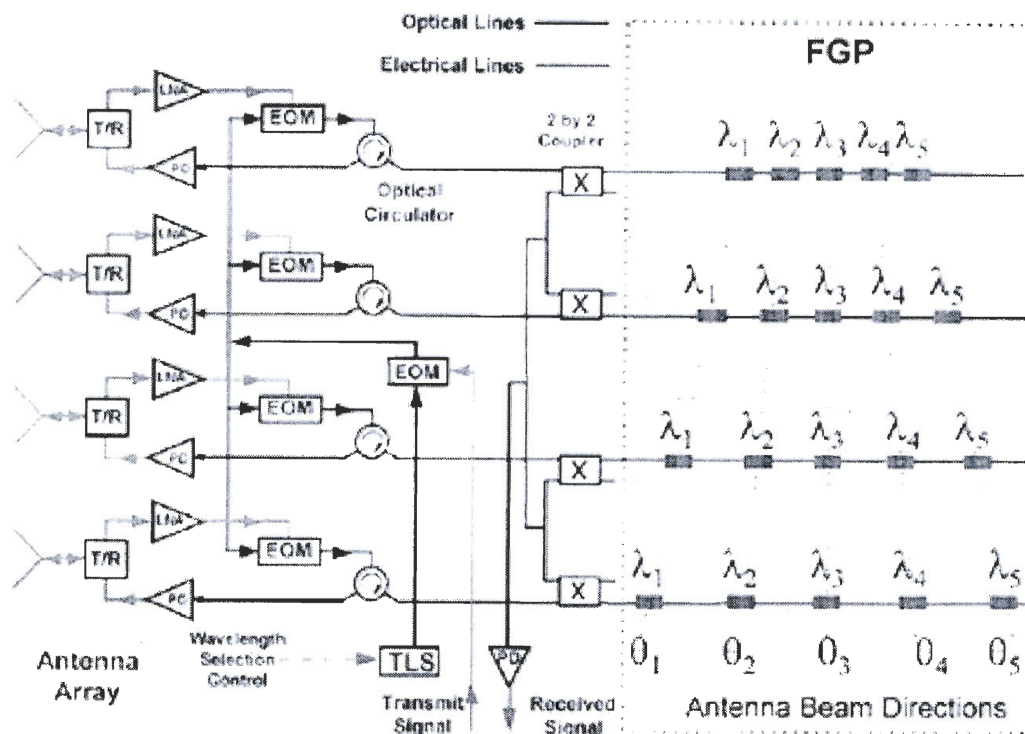


Figure 3-2: Integrated transmit/receive optical beamforming system illustrating the spatial layout of the Bragg gratings for the FGP, shown for the case of a four-element array with five discrete steering angles [29].

The two main considerations in analyzing the described system are power budget and positioning error. Regarding system loss, the laser power reaching the PDs in Figure 3.2 is reduced by several factors in both transmit and receive mode of operation. The FGP introduces a loss $1-R$, where R is the reflectance of the selected grating. The reflectance of the gratings can be greater than 99%, while the $M-1$ unselected gratings per channel do not introduce appreciable optical loss, typically less than 0.5 dB. The major loss mechanisms are the couplers (6 dB round-trip), the $1:N$ splitter ($10 \log N$ dB) and the circulator (approximately 1 dB per direction). Note that the receive mode experiences additional loss due to a second $N:1$ splitter. There are also two EOM modulators that typically introduce excess loss of approximately 7 dB. Splices, connectors, isolators, polarization control, and the like will add additional loss to the system. The total loss is the sum of the above, and the RF loss is twice the optical loss. However, loss does not cause serious problems since the system is fiber-based and optical amplifiers can be incorporated into the design to compensate for the

insertion losses in the system. On the other hand, the positioning accuracy of the FBGs on the fiber limits the delay accuracy. A delay error causes the actual steer angle to differ slightly from the design goal. A positioning accuracy of ± 1 mm corresponds to 1.4° and 2.8° direction error, at 2.5 GHz and 5 GHz respectively.

3.3.2. TTD Beamforming Using CFBG and Multiwavelength Tunable Laser

In [26], the authors presented theoretical and experimental results of the phase and amplitude distributions of a microwave modulating signal when the optical carrier is reflected by a CFBG. The signal of a multiwavelength laser source is amplitude modulated by an EOM and after reflection in a linearly CFBG, the different wavelengths are demultiplexed to drive the elements of a PAA. The signal is distributed to the antenna elements through an $1:N$ power splitter and subsequently filtered by a set of tunable bandpass filters, as it is illustrated in Figure 3.3. The corresponding amplitudes and phases arising from the reflection at the Bragg grating determine the radiation pattern of the PAA.

Each wavelength of multiwavelength laser source carries the signal for a specific element of PAA and by taking advantage of the chirp of CFBG, each wavelength experiences different amount of time delay when it is reflecting in CFBG as shown in Figure 3.3. Two consecutive array elements are fed with two different optical wavelengths ω_i and ω_{i-1} , and the resultant steering angle can be written in terms of the grating time delay as:

$$\sin(\theta) = \frac{c}{d} (\tau(\omega_i) - \tau(\omega_{i-1})) = \frac{c}{d} \Delta\tau \quad (3.2)$$

where d is the distance between the array elements, c is the velocity of light, $\tau(\omega_i)$ is the time delay experienced by the signal on wavelength ω_i and $\Delta\tau$ is as depicted in Figure 3.3. This equation is another version of (1.2). The time delay (τ) of a fiber grating depends on the grating chirp. The function $\tau(\omega)$ is linear in gratings with a linear chirp; in that case, the beamforming network can operate by distributing a set of equally spaced optical frequencies to the array elements and the steering angle can be continuously controlled by the frequency steps.

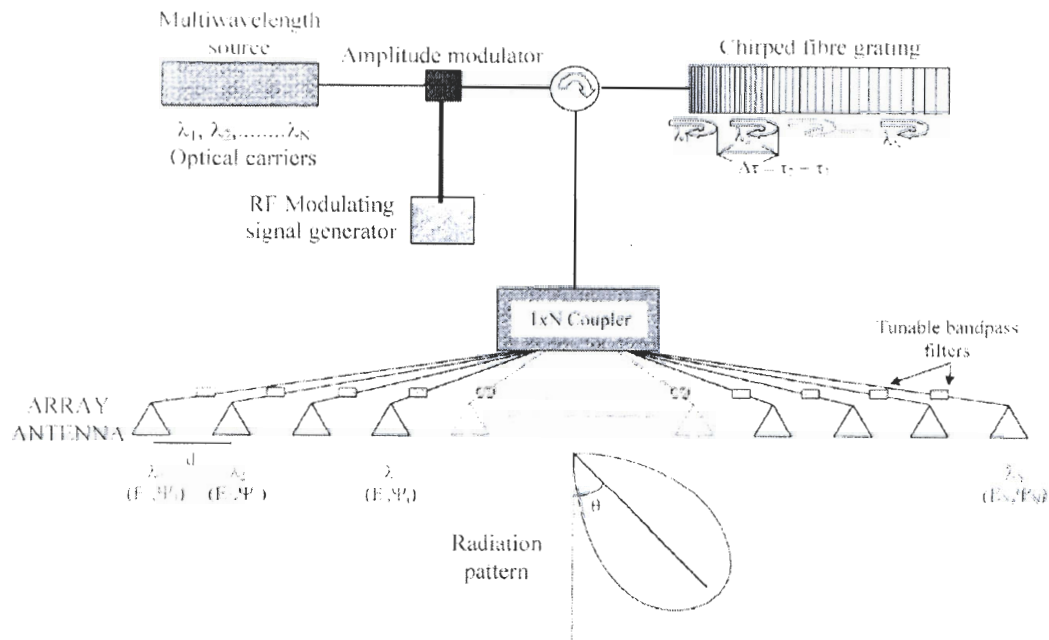


Figure 3-3: Schematic of a PAA steered by a CFBG. Different optical wavelengths are routed to the radiators through a WDM system [26].

Unlike [29], this system provides continuous beamforming. In [26], the authors reported the measured time delay response for a maximum steering range of 180° for an 18 GHz bandwidth. They also simulated the resulting radiation pattern for a 32-element PAA.

The main considerations for the described system are the need for a multiwavelength TLS and the vulnerability of DSB modulation to dispersion. The main difficulty in of this system is that one needs to provide a multiwavelength source in which the wavelengths should be tuned simultaneously with equal increasing or decreasing wavelength spacing. For a TTD system with N channels, for example, N tunable laser sources with the wavelengths controlled by a programmable wavelength controller should be used. Furthermore, this system requires tunable optical filters to select each wavelength before its respective PD. These make the whole TTD system bulky, sensitive and very expensive.

In the detection process, there are two signals arising from the beating between the optical carrier and each sideband; the optical signals interfere in order to yield the detected signal at the microwave modulating frequency. It is well known that chromatic dispersion can in-

roduce RF signal fading when the two sidebands become out of phase [26]. Substituting the grating phase response by its second-order Taylor series, [26] obtained that the detected RF signal drops to zero when the time delay difference between both sidebands is an integer value times the period of the RF signal, which corresponds to the following modulating frequency f_{null} :

$$f_{null} = \frac{1}{\lambda_0} \sqrt{\frac{c}{2D}} \quad (3.3)$$

where D is chromatic dispersion of the CFBG. This phenomenon imposes a limitation on the operational bandwidth. The limitation arising from signals beating can be overcome by using the single side band (SSB) modulation technique, at the expense of another increase in system complexity and cost.

This design was improved later by [30], using multichannel CFBG to reduce both the grating length and laser source tuning range. Reduction of laser tuning range enables this system to operate in a WDM configuration, and to replace the tunable optical bandpass filters with an AWG.

3.3.3. TTD Beamforming Using Tunable CFBG

In [28], a continuously variable delay line for PAA applications is presented. The proposed delay line operates at a single wavelength and is based on a properly designed linear CFBG. Continuous delay is achieved by changing the temperature or strain along the grating region. The setup of the proposed TTD unit employing a CFBG delay line is illustrated in Figure 3.4. The laser is externally modulated by a microwave signal through an EOM. The modulated light feeds a group of N single mode fibers through an equal path 1: N power divider. It is worth mentioning that this architecture is not based on a WDM approach and each channel is transmitted on a separate optical fiber. Therefore, if the N -element PAA location is far from the central unit, we need to connect the PAA to the beamformer with N parallel fibers. For each branch, the modulated wavelength is guided through an optical circulator to a wideband CFBG with a central wavelength of λ_B . Each CFBG is properly actuated in strain or temperature and the actuator system is controlled by a simple feedback

loop. The imposed perturbations in every line will be set by the controller in order to provide the distribution of phases needed to achieve the desired radiation pattern of the antenna. The N delayed modulated lights are then detected by high-speed amplified photodetectors and sent to feed the antenna elements. In a PAA, the steering angle corresponding to the main lobe of the array antennas (θ_0) can be calculated from (1.2). In this system, considering a single branch, continuous time delays $\Delta\tau$ are obtained by uniformly perturbing the grating so that the optical carrier is reflected at different spatial locations along the grating region, leading to different traveling times for the signal. Thus, the time delay for each channel is determined by the spectrum shift $\Delta\lambda_B$ induced by the applied perturbation.

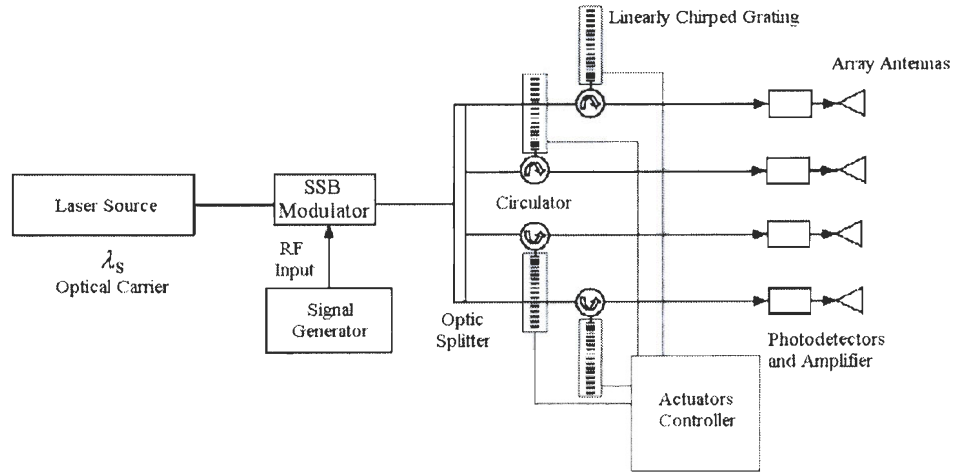


Figure 3-4: Configuration of the beamformer based on tunable CFBGs for a four-element array [28].

If a linear chirp is chosen, the relation between the resonance position and the wavelength shift ($\Delta\lambda_B$) is linear, as is the round-trip delay. If the group delay is linear enough, then the time-delay ($\Delta\tau$) depends on the CFBG mean dispersion (D_m) and on $\Delta\lambda_B$ according to the approximated relation of:

$$\Delta\tau = D_m \cdot \Delta\lambda_B \quad (3.4)$$

It is well known that the relation between a temperature variation (ΔT), a strain change ($\Delta\varepsilon$) and the grating spectrum shift ($\Delta\lambda_B$) is [31]:

$$\Delta\lambda_B = (K_\varepsilon\Delta\varepsilon + K_T\Delta T)\lambda_B \quad (3.5)$$

where K_ε and K_T are, respectively, the strain and the thermal normalized responsivity. Based on this line of argument, the linearly chirped grating provides a linear delay difference.

Similar to [26], this system provides continuous beamforming. In [28], the authors reported the measured time delay response for a maximum steering range of 110° for a 30 GHz bandwidth. They did not measure or simulate the radiation pattern.

The two main considerations in analyzing the described system are component issues and positioning error. On one hand, considering the number of FBGs in the link, the same number of optical circulator is required which increases the price and volume of the system. For instance an eight-element PAA will need eight optical circulators. On the other hand, employing SSB modulation to overcome dispersion interaction (as discussed in Section 3.3.2) increases the link complexity and cost as well. Furthermore, a delay bias error can exist because of the limited positioning accuracy of the FBGs on the fiber and the variation of the fiber feedings for different channel. However, this uncertainty can be calibrated and compensated for each channel by the FBG delay lines.

Reference [32] presented a beamformer using a similar concept and compatible with WDM configuration by employing a multiwavelength laser source and just one tunable CFBG as shown in Figure 3.5 for a five-element PAA. The light of the multiwavelength laser is externally modulated by a microwave signal through an EOM. The output of the laser source has five fixed wavelengths with identical wavelength spacing which makes it compatible with WDM configuration. The modulated light is sent to the tunable CFBG through an optical circulator, and then reflected by the tunable CFBG. The reflected light feeds a group of single-mode fibers through an equal-path $1:N$ power divider. Each channel includes a band-pass filter whose center wavelength coincides with one of the N wavelengths of the laser source. The different time delays are obtained in accordance with the particular carrier wavelengths for N different channels. The delayed modulated light is then detected by N amplified PDs to feed PAA elements. The time delay difference is linear with the chirp rate and the beam direction can be tuned by changing the chirp rate of the CFBG.

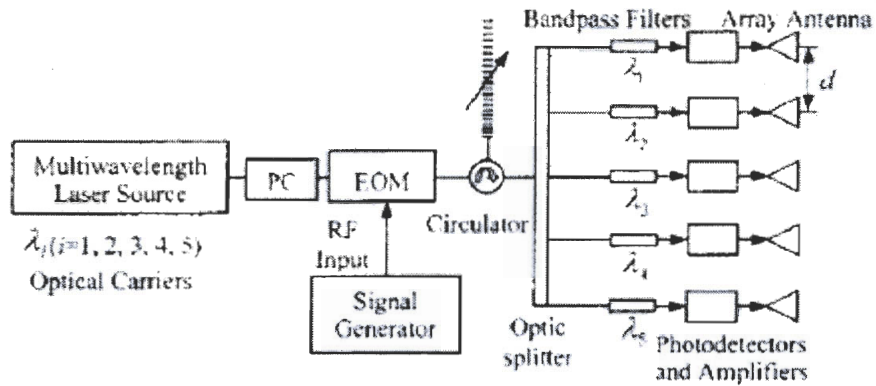


Figure 3-5: Schematic of the beamformer based on tunable CFBG for a four-element array complying WDM configuration [32].

3.4. Independent Optical Control over the Phase and Amplitude

For low modulation depths, the optical baseband equivalent description of the electric field, $E(t)$, of a DSB modulated optical signal can be approximated by the sum of three spectral components. After filtering the signal with an optical filter, we can write the electric field as:

$$E(t) = A_c e^{j\phi_c} + A_{SL} e^{j(-\omega_{RF}t + \phi_{SL})} + A_{SU} e^{j(+\omega_{RF}t + \phi_{SU})} \quad (3.6)$$

where ω_{RF} is the RF modulation frequency, A_c and ϕ_c are amplitude and phase of the optical carrier, A_{SL} , ϕ_{SL} , A_{SU} and ϕ_{SU} are the amplitudes and phases of the lower and upper modulation sidebands. In the most general case: $A_{SL} \neq A_{SU}$, but if the filter amplitude is constant over the spectrum band, we can take $A_{SL} = A_{SU} = A_s$. Thus, after photo-detection, the detected RF voltage signal at ω_{RF} is proportional to:

$$V_{RF} \propto A_c A_s \cos(\phi_L - \phi_U) \cdot \cos(\omega_{RF} + \phi_L + \phi_U) \quad (3.7)$$

where $\phi_U = \frac{\phi_{SU} - \phi_C}{2}$ and $\phi_L = \frac{\phi_C - \phi_{SL}}{2}$ represent half the cumulated phase difference between the sidebands and the carrier due to the filter phase response. Note that ϕ_U and ϕ_L can be written as:

$$\phi_L = \frac{1}{2} \int_{-\omega_{RF}}^0 \tau(\omega) d\omega \quad (3.8a)$$

$$\phi_U = \frac{1}{2} \int_0^{\omega_{RF}} \tau(\omega) d\omega \quad (3.8b)$$

where $\tau(\omega)$ is the group delay response of the optical filter. With fiber dispersion, (3.7) transforms into [33]:

$$V_{RF} \propto \cos\left(\phi_L - \phi_U + \frac{L_f D}{4\pi c} \lambda_0^2 \omega_{RF}^2\right) \cdot \cos(\omega_{RF} t + \phi_L + \phi_U) \quad (3.9)$$

where D is the dispersion, L_f the fiber length, c the speed of light and λ_0 the optical carrier wavelength. According to both (3.10) and (3.12), $\phi_L + \phi_U$ appears in the signal phase and $\phi_L - \phi_U$ appears in the signal amplitude. Therefore by adjusting separately ϕ_U and ϕ_L , independent control of signal phase and amplitude is possible. Note also that by a wise selection of $\phi_L - \phi_U$, one can compensate for chromatic dispersion of the ROF link. Therefore, the independent control over ϕ_U and ϕ_L is key for independent setting of amplitude and phase for the signals feeding the array element.

For a single channel, the proposed structure of a novel beamformer is sketched in Figure 3.6. This solution was proposed by Mr. Marco Sisto, a PhD student at COPL [34]. The beamformer is physically formed by two FBG-based optical filters, one with positive chirp and the other with negative chirp (the absolute chirp factor is similar). We will refer to the gratings as FBG_L and FBG_U , because they are used to adjust ϕ_L and ϕ_U respectively. Recalling (3.8a) and (3.8b), we note that the values of ϕ_U and ϕ_L are each defined by the integrated group delay, respectively, in the lower and upper portion of the spectrum, between

the modulation sidebands and the optical carrier. By stretching or controlling the temperature of the gratings, their delay response can be shifted, thus the values of ϕ_U and ϕ_L can be tuned. Since the actuators work independently on two different gratings (FBG_L and FBG_U), the control over ϕ_U and ϕ_L will be independent.

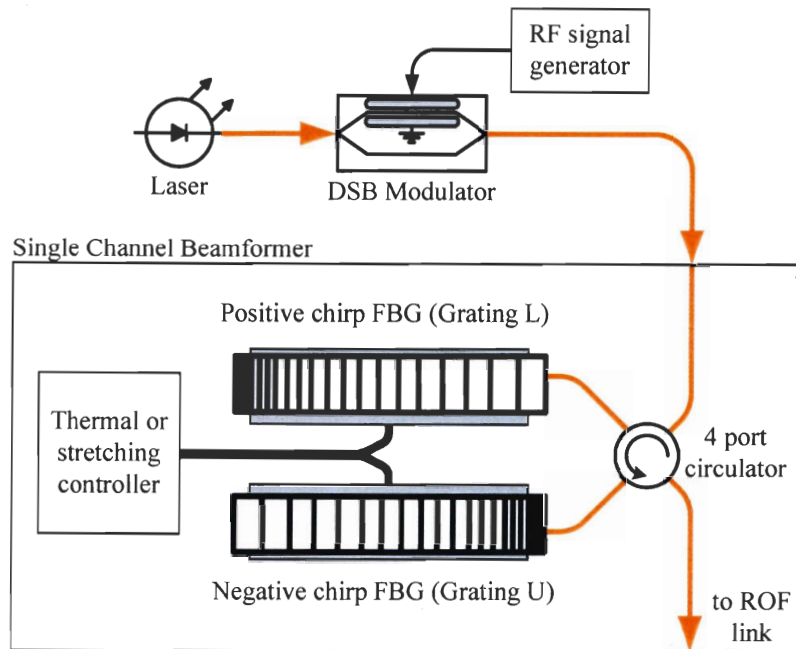


Figure 3-6: The single-channel architecture of the proposed novel optical beamformer.

3.4.1. ϕ_U and ϕ_L Control based on Gires-Tournois Filters

To design the FBG_L and FBG_U gratings, we used a Gires-Tournois cavity that is a Fabry–Perot etalon with a 100% back-reflector. This is an all-pass filter operating in reflection, that has spectrally periodic group delay variations with a free spectral range (FSR) fixed by the cavity length. In order to tailor the shape of the group delay response of the filter, lattice-coupled cavities [35] might be implemented by adding more reflectors with the same relative spacing and conveniently designed reflectivities. The reflectors may be made by superimposed CFBGs, so N superimposed CFBGs form $N-1$ Gires-Tournois fiber Bragg grating coupled cavities (GT-CCs). The beamformer that we propose is physically formed by a pair of these GT-CC filters (Figure 3.6) and we call the whole system a Gires-Tournois beamformer (GT-BF).

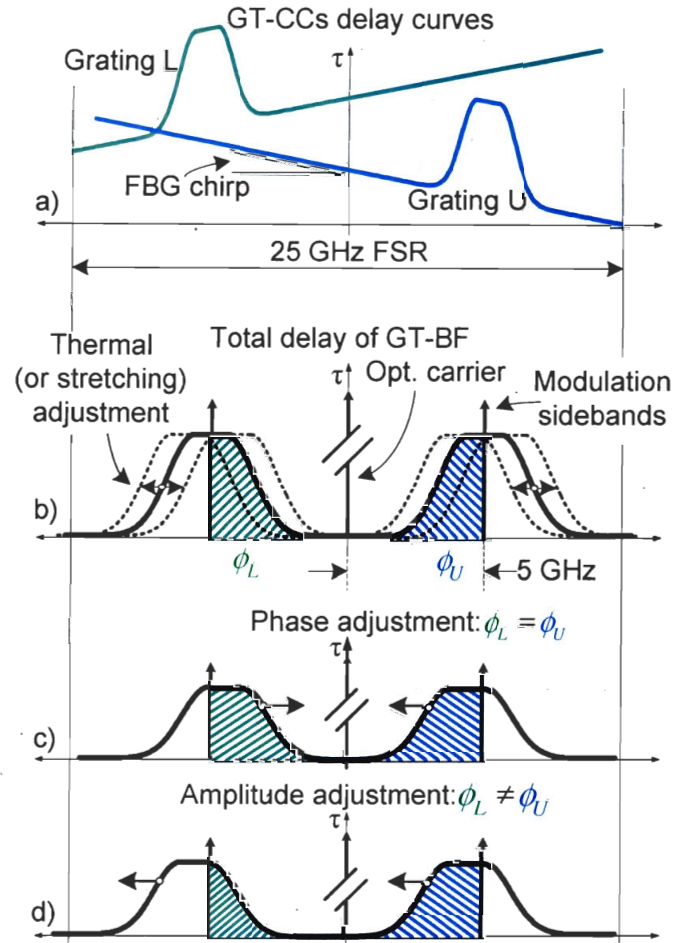


Figure 3-7: Theory of operation of the GT-BF for one optical wavelength: a) The GT BF is composed by two GT-CCs with 25 GHz FSR with conveniently designed delay curves. The delay peaks from each GT-CC are centered on two modulation sidebands. The peaks are repeated periodically every 25 GHz. b-d) Amplitude and phase of the antenna signals are controlled by adjusting the relative position of the peaks.

The delay response of each GT-CC over one FSR is shown in Figure 3.7a: the FBG chirp causes a linear increase of the GT-CC delay response over the FSR which adds up to a delay peak at the cavity resonance frequency. The group delay is additive, and because the cascaded GT-CCs have chirp with the same absolute value but opposite sign, the total delay is flat over the FSR except for the two peaks at the resonance frequencies of the two GT-CCs as shown in Figure 3.7b. The peaks can be shifted independently in order to increase or decrease the value of the integrals in (3.8a) and (3.8b). When the peaks are shifted sym-

metrically (Figure 3.7c) with respect to the optical carrier, the first cosine term in (3.9) is kept at unity and only the signal phase is changed. When the peaks are shifted non-symmetrically (Figure 3.7d), the amplitude can be changed while keeping the phase constant.

a) Design of GT-CCs and Simulation Results

In the following we briefly describe how the GT-CCs has been designed; more details can be found in [15]. As already explained, the GT-CCs should have a 25 GHz FSR to be compatible with DWDM systems. The cavities are physically realized using superimposed CFBGs, shifted by a distance $L_c \approx 4$ mm. This fixes the FSR following the well known Fabry-Perot relation:

$$FSR = \frac{c}{2n_g L_c} \quad (3.10)$$

where c is the speed of light and n_g is the group index. When using a lattice-coupled design, two or more cavities are appended by adding more superimposed CFBGs. Then, the total coupled-cavity length is mL_c where m is the number of coupled cavities. The greater the value of m , the easier it is to tailor the delay and amplitude response. Also, note that the values of ϕ_U and ϕ_L are limited to a maximum range of $m\pi$, which allows for a maximum signal phase shift of $2m\pi$. However, the extreme values of ϕ_U and ϕ_L require maximum shifts of the delay peaks, which is impractical for a single cavity design. So, $m > 1$ is needed for $(0, 2\pi)$ signal phase shift. The maximum value of m is fixed by other constraints, such as coupled-cavity spacing and maximum grating length, as explained later. We designed the GT-CCs using three coupled cavities (four superimposed CFBGs) with a total length of 12 mm.

The CFBGs have a reflection bandwidth which covers several FSR. Because they are distributed mirrors along the grating physical length, each FSR is placed at a different physical position along the grating length. The FBG chirp C is constant so the resonant frequency spacing, or the cavity spacing, is constant and equal to:

$$d_{FSR} = \frac{FSR}{C} \quad (3.11)$$

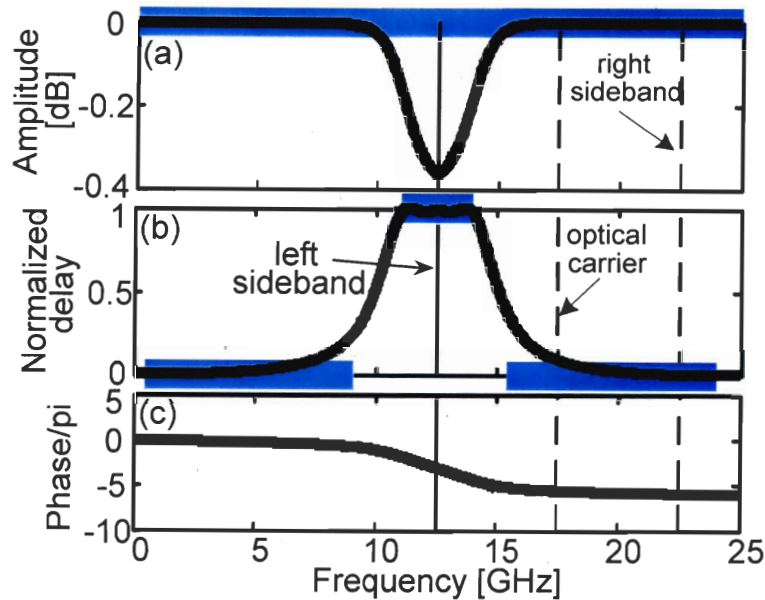


Figure 3-8: Design of the optimum GT-CC. Blue lines represent the design target: amplitude response (a), normalized delay response (b) and resultant phase response (c).

We considered $d_{FSR} > mL_c$, avoiding spatial superposition between the cavities. However, d_{FSR} cannot be made arbitrarily large because the design must satisfy the relation:

$$N \cdot d_{FSR} < L_{FBG} \quad (3.12)$$

where N is the number of FSRs covered by the grating and L_{FBG} the maximum grating length. Chirped gratings can be written in the fiber using a chirped phase mask and the mask length limits L_{FBG} to a maximum practical value of 14 cm considering the lab facilities, i.e. the available phase masks and fabrication techniques. So, using a phase mask with a 0.1 nm/cm chirp, $FSR = 25$ GHz and $n_{eff} = 1.46$, we have $d_{FSR} = 1.37$ cm and we can accommodate eight FSRs along an 11cm-long grating, well within L_{FBG} . This value of d_{FSR} also respects (3.12) and justifies the choice of designing the GT-CCs with three coupled cavities.

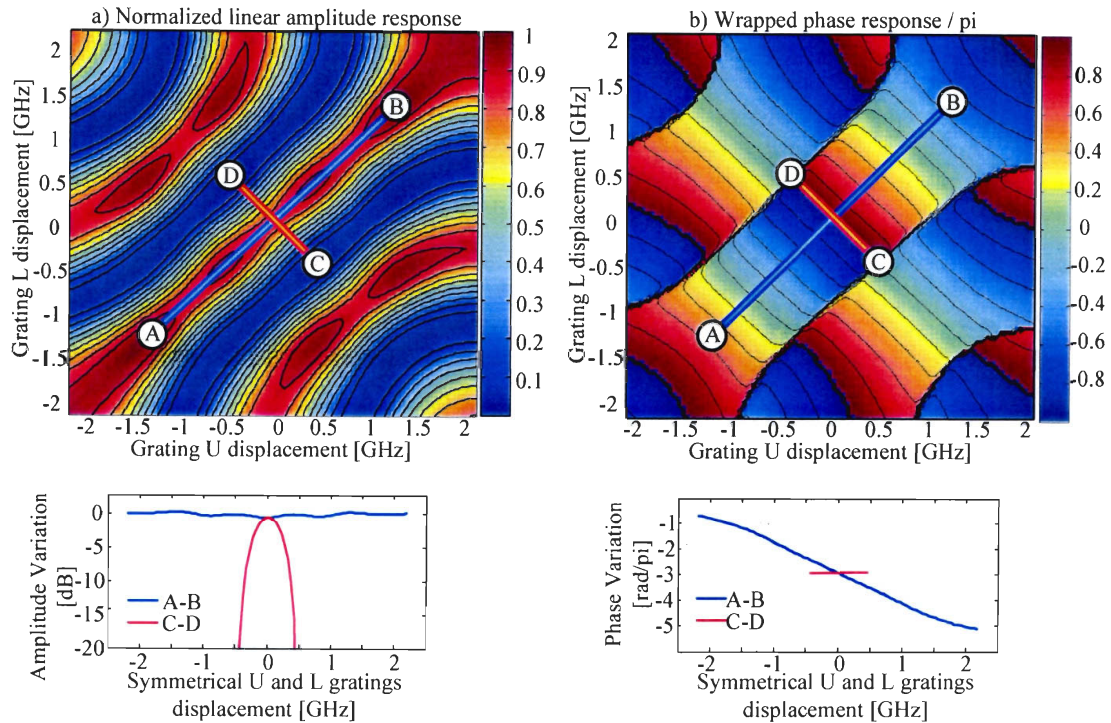


Figure 3-9: Map representing the normalized amplitude (a) and wrapped phase (b) response of the GT-BF as a function of the shift of the delay peaks from the reference position centered on the modulation sidebands.

After fixing the number of cavities, we designed the shape of the delay response of the GT-CCs by tuning the FBGs. The phases of coupled cavities are fixed and identical. The design method is divided into three steps: first we define a target group delay response. Afterwards, we calculate the delay response of a bulk coupled cavity filter using a polynomial ARMA model [35] and we apply an optimization algorithm on the reflectivity values in order to approximate the target delay response. The target delay that was defined for the peak centered on the left modulation sideband is shown by the blue bold lines of Figure 3.8b. To ensure the linearity of the GT-BF phase response over a 100 MHz bandwidth, the delay peaks must be flat over a band of at least 100 MHz around the sideband for every position of the delay peak. Also, the delay peak, which controls the value of ϕ_L , must not affect the value of ϕ_U and vice versa. In addition, the resolution on the position of the peak is finite and fixed by the temperature or stretching resolution; therefore, a lower and wider peak allows for more phase shift resolution. We defined the target delay curve with a flat zone

width of 2.5 GHz and a minimum value in the region between the optical carrier and the right sideband to ensure maximum decoupling between ϕ_U and ϕ_L .

The simulations of the phase and amplitude response of the GT-BF are shown in Figure 3.9a and 3.9b respectively. These simulation results are based on modeling and optimizing a thin film filter with three coupled cavities. Simulation was performed using a Z-transform model of the three-cavity GT-BF. The model allows calculating the response from the values of cavity mirror reflectivity and cavity phase (small variations over length). All cavities were assumed to have the same phase (exactly the same length). A genetic algorithm was used to find the reflectivities of the three mirrors forming the cavities. The fourth mirror is assumed to have 20 dB reflectivity (four mirrors are needed for three coupled cavities). The genetic algorithm calculated these reflectivities as (from strongest to weakest): 13.4 dB, 8.35 dB and 1.58 dB.

In Figure 3.9, at the (0, 0) GHz position, the delay peaks are centered on the modulation sidebands. Moving the gratings position along the secondary diagonal (line A-B) of these maps, from (-1.2, -1.2) GHz to (1.2, 1.2) GHz, allows for more than 2.3π phase shift of the RF signal with variations in amplitude below 0.5 dB. Amplitude variations are due to the amplitude response of the GT-CCs is not being perfectly flat. To get exactly constant amplitude, the working point must be moved on the isolines shown in Figure 3.9a. Phase is constant and amplitude varies when moving the gratings along the main diagonal (line C-D).

b) Experimental Measurements: Single-Cavity GT-CCs

Superimposed CFBGs can be written in fiber using a chirped phase mask and exposing to UV light the same section of fiber again and again. However, this method is not practical for more than two superimposed FBGs, because it is hard to precisely couple the cavities. The three-cavity GT-CCs can be more easily obtained using a phase-sampled phase mask, which also provides precise identification of the position of the cavities [36]. At first, we did not have this complex phase mask, so we measured and simulated the performance of a single-cavity GT-BF, obtained by writing two superimposed CFBGs written with a standard phase mask, in order to prove the validity of our simulations. The FBG-based filters

for the measurement was written on UVS-INT fiber (without hydrogen) with a chirp factor of 0.5 nm/cm, a cavity length of 4 mm and a reflectivity about 30 dB. Each grating was 40 mm long and showed less than 3 dB loss.

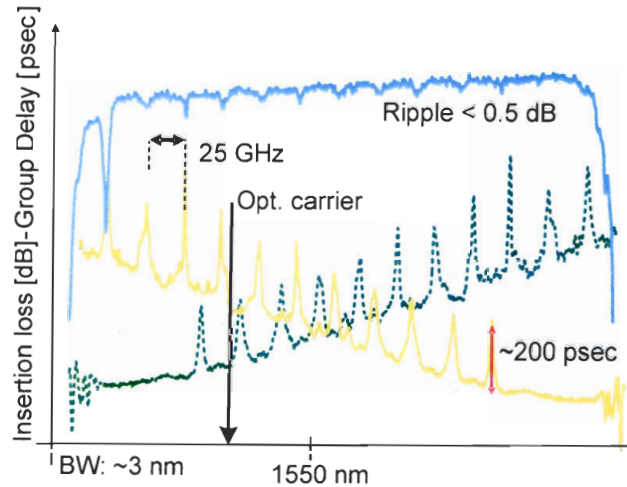


Figure 3-10: Measured insertion loss and group delay of the single-cavity GT-CCs.

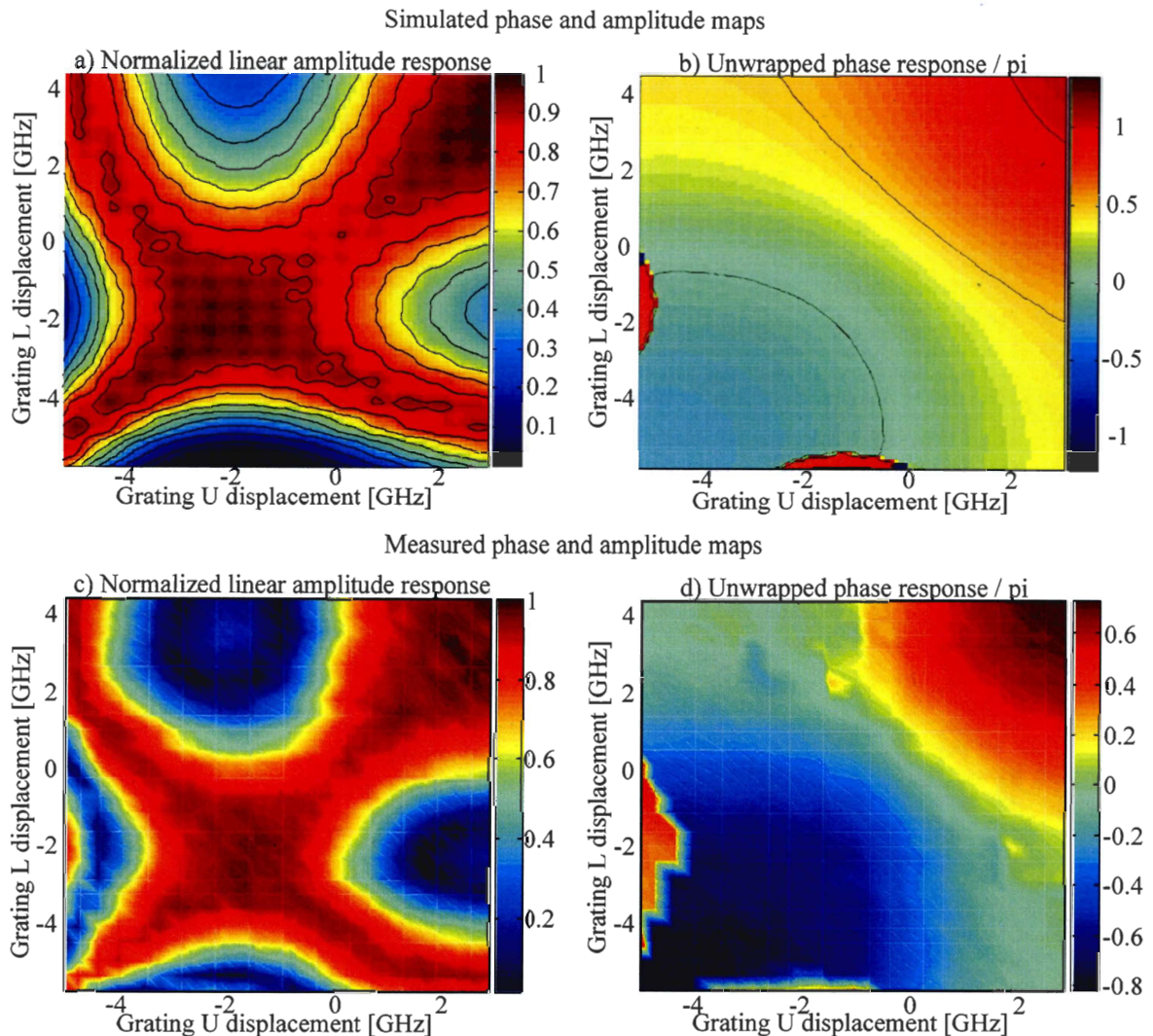
The measured insertion loss and group delay response of a single-cavity GT-CC over several FSR are shown in Figure 3.10. The simulated phase and amplitude maps as a function of the position of the delay peaks are shown in Figure 3.11a and 3.11b and the measured behavior as a function of grating temperatures is shown in Figure 3.11c and 3.11d. The measurement setup for this experiment is depicted in Figure 3.12. The light of the laser source is modulated by a MZ modulator biased at quadrature point with 5 GHz sinusoidal RF carrier and after optical amplification it passes through the single-channel beamformer. Note that the tunable laser is used to have more freedom in selecting one specific peak pair in the GT-BF response, but its wavelength is fixed along all measurements. We programmed LabVIEW to automatically control the setup: the software sends commands to the thermal controller to fix the temperature of the gratings. After a few seconds for thermal stabilization, the real-time oscilloscope is used to acquire an image of the detected sinusoidal signal after being filtered by the GT-BF. The oscilloscope is synchronized with the RF signal generator and triggered on a 10 MHz reference clock, also given by the RF signal generator and in a fixed relation of phase with the 5 GHz tone. On the oscilloscope, the 5 GHz trace appears stable and is acquired and saved on the computer. For recording the sig-

nal, an averaging factor of 256 was applied. We next set switches to exclude the laser and the detector from the circuit; the GT-BF is fed with a test signal coming from the optical network analyzer which is used to measure the optical delay of the GT-BF. With this second measurement, we can ensure a proper map of the temperature settings to values of shifts of the delay peaks, so that we can calculate amplitude and phase maps as a function of the actual frequency shifts of the delay peaks. The timing management and measurement synchronization were two of the most important issues in this setup. For instance, thermal stabilization of the filters and the transient time of switches should be respected. The thermal stabilization time delay value depends on the temperature controllers, temperature tuning steps and the structure of heating facilities: for a step of 0.2° in this setup, a delay of 10 second has been applied. All the data is saved on a computer and post-processed using MATLAB code to calculate the amplitude and phase maps shown in Figure 3.11c and 3.11d, where they are compared with the simulation maps. The same setup can be used to measure the performances of the filter with OFDM signals, as described in the Section 3.5.2.

As anticipated from the design process, one cavity does not allow for 2π phase tunability: maximum simulated and measured phase tunability is about 1.6π . Furthermore, perfect amplitude control for each desired phase value cannot be achieved.

c) Efforts towards a Multichannel Solution

Encouraged by the good agreement between measurement and simulation results for the single-cavity GT-CC, and considering the simulated amplitude and phase tunability of a three-cavity GT-CC, the next step clearly would be to fabricate a three-cavity GT-CC. Furthermore, due to the spectrally periodic phase response of the Gires-Tournois filters, the signal from a multiwavelength source can be processed by a single pair of gratings and then demultiplexed to feed an antenna array. Because of the underlying chirp of the fiber grating structures, the resonating fields at each wavelength are spatially separated along the fiber axis and independent tuning of each signal can be obtained by the use of a segmented heater as represented in Figure 3.13 and previously used for chromatic dispersion compensation [37].



Our objective was therefore to develop a multichannel beamformer requiring a single pair of GT-CC filters. This idea was based on the assumption that, with the right GT-CC design, it could be possible to control all the RF signals for all the array elements by associating each signal to different FSRs of the periodic response of GT-CCs to map each FSR to a different physical section of the GT-CC gratings by choosing the appropriate chirp and to control these sections independently. This was suggested by the fact that the minimum physical length of a series of N coupled cavities with a given FSR is:

$$L_{FBG} = N \frac{c}{2n_g FSR} \quad (3.13)$$

where c is the speed of light, N is the number of FSRs and n_g is the fiber group index. For a three-cavity design with the FSR of 25 GHz, $L_{FBG} \approx 1.2$ cm.

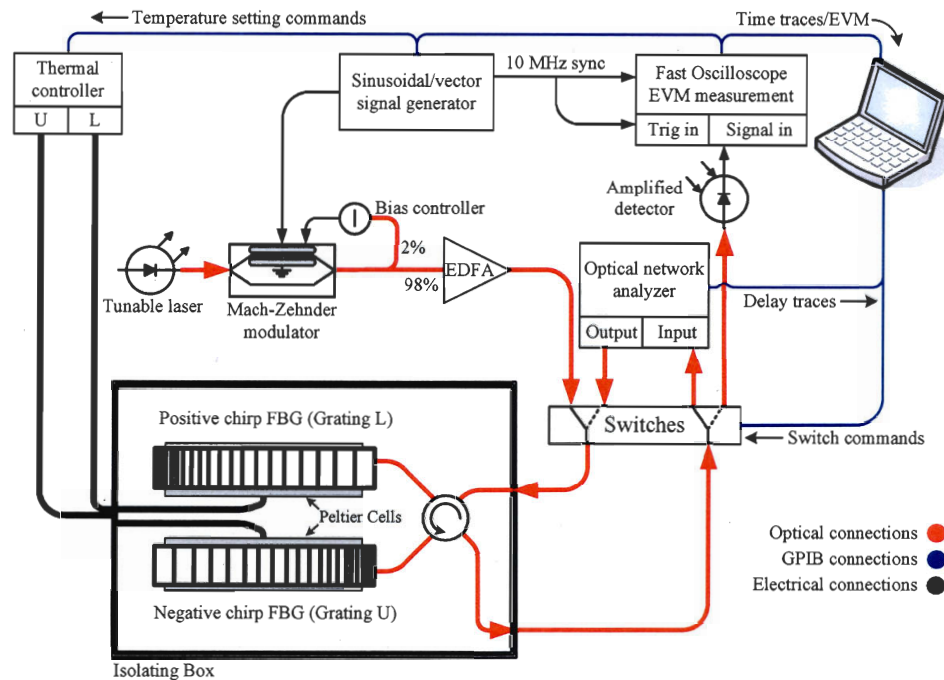


Figure 3-12: Setup for measurement of the amplitude and phase maps. Tunable laser: Phonetics tunics-BT; Modulator: JDS OC-1; EDFA: JDS OAB1552+1FA0; Switch: JDS SB series; Thermal controller: ILX LDT 5910B; Signal Generator: Agilent E4438C; Fast Oscilloscope: Agilent DSO81004B Infiniium, real time, 10 GHz bandwidth; Optical Network Analyzer: Advantest Q7750; Bias Controller: YY-Labs Mini-MBC-2; EVM Analyzer: Agilent E4440A; Amplified Detector: Agilent 11982A LCA.

Equation 3.13 is a simplification of a more complex reality because it considers the gratings as localized reflectors. This is indeed a poor assumption: the cavities extend much more than L_{FBG} because the gratings have non-zero length of interaction with the optical signal. However, by choosing $d_{FSR} \gg L_{FBG}$ it seemed possible to effectively separate the FSRs in such a way that each FSR, and signal wavelength, was mapped in a different portion of the GT-CC grating. Temperature or stretching control of each section of the gratings would affect the signal wavelengths separately and independently.

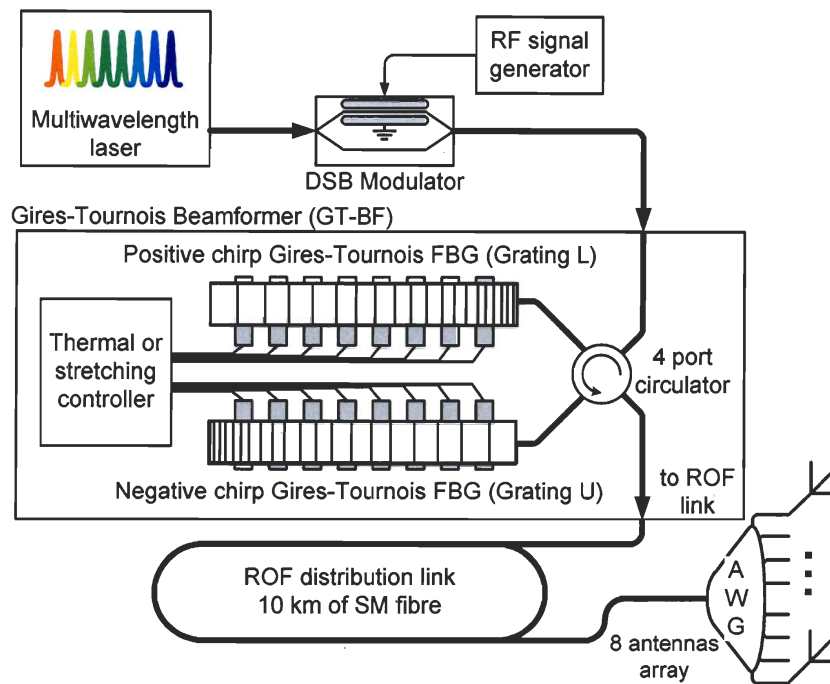


Figure 3-13: Proposed architecture for DWDM-ROF link using GT-BF.

To test this idea, we undertook simulations of a three-cavity GT-CC grating. With the modulation index distribution obtained from the design step, we simulated a local variation of temperature, that is, a variation of the average index in a specific location along the GT-CC grating, and we tried to optimize the width and position of the perturbed zone to observe the shift of a delay peak while the adjacent peaks stay unchanged. Unfortunately, we have not been able to shift a delay peak while keeping its shape and leaving unchanged the adjacent peaks. We found that the shape of the delay peaks were very sensitive to very small perturbations of the relative phases of the cavities. In our best designs, the delay shape is conserved only if the average index perturbation extends over more than 2.5 cm, but the adjacent peaks are heavily distorted. On the other hand, a perturbation extending over a short grating region leaves the adjacent channels unchanged but strongly perturbs the shape of the tuned channel. We tried other chirp values for the grating design, but gratings with very low chirp must be very long to cover eight FSRs (for eight-channel beamforming). The limit on the grating length is fixed by the maximum length of the phase mask, which was 14 cm. Within this grating length, we did not find a satisfying design [15].

3.4.2. A New Design Approach

In the following we briefly describe the new design approach; more details and a comprehensive study can be found in [15]. The simulated traces of reflectivity and delay for new designs of the FBG_L and FBG_U are shown respectively in Figures 3.14a and 3.14b. These designs are not based on coupled cavities anymore and do not provide multi-channel capabilities. We will call this new device a discrete-gratings beamformer (DG-BF).

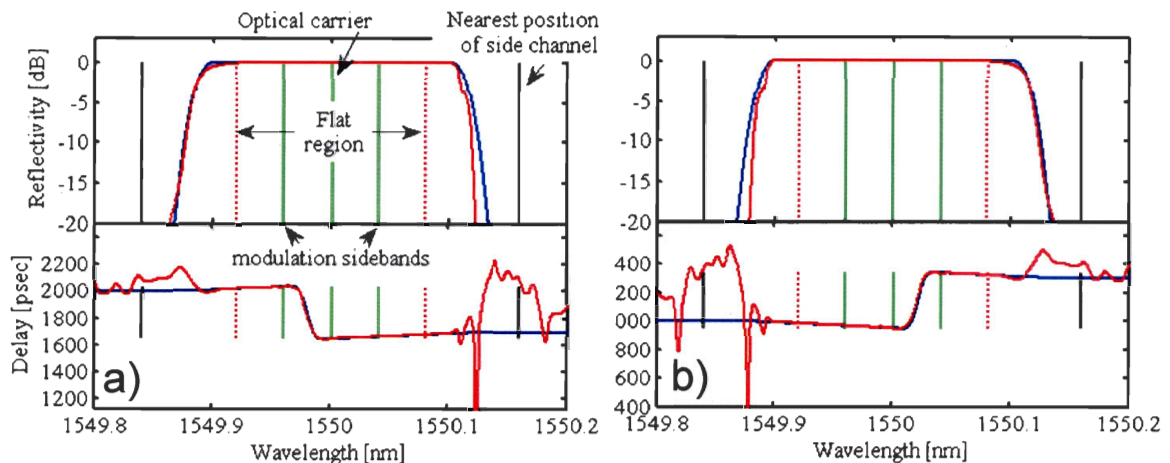


Figure 3-14: Reflectivity and delay of the FBG_L (a) and FBG_U (b) for DG-BF. In blue: design goal; in red: actual grating. Green vertical lines represent the position of the optical carrier and modulation sidebands. Red dotted lines limit the region of maximum flat response.

The gratings are designed to have a flat pass-band amplitude response with a bandwidth of 20 GHz, and a step-shape delay response centered respectively onto the lower and upper modulation sideband of the optical spectrum. The gratings chirp is ± 0.25 nm/cm. The gratings reflectivity must be lower than -20 dB in the out-of-band region, where the adjacent channels are transmitted: the modulation sidebands of the nearest channels are 20 GHz on either side of the carrier frequency of the reference channel. We imposed -20 dB reflectivity at 17 GHz to either side of the carrier frequency of the reference channel. The gratings are 85 mm long. Their modulation index is first calculated using a layer peeling algorithm [38], and then multiplied by an apodization window to limit the grating lengths.

We can simulate the amplitude and phase maps for this solution, in a similar way as we did for the GT-CC design, by shifting the gratings delay and amplitude response shown in Fig-

ure 3.14. The resultant simulation maps are presented in Figure 3.15a and 3.15b, where a black quasi-rectangular zone gives the region of operation. The maximum phase tunability range along the secondary diagonal of the map of Figure 3.15b reaches up to 2.5π , as shown in Figure 3.18b. Furthermore, for each desired phase value, by tuning in the perpendicular direction, we can attenuate the amplitude by 10 dB while keeping the phase amount constant. These two features are similar to the capabilities of the GT-BF three-cavity simulation (Figure 3.9) and provide all we need for a null-steering beamformer.

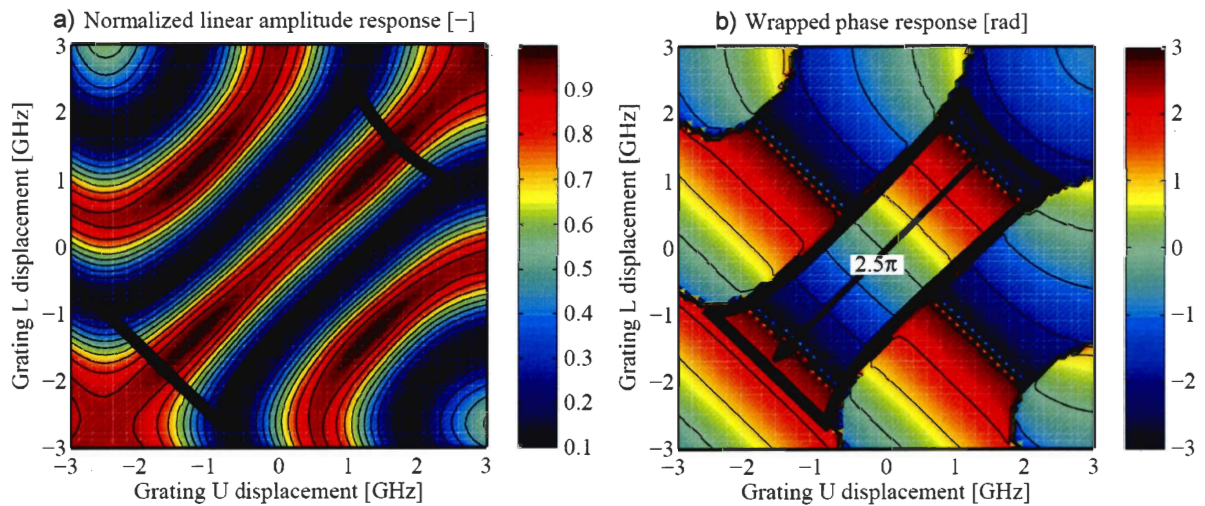


Figure 3-15: Simulated amplitude (a) and phase (b) maps of the DG-BF.

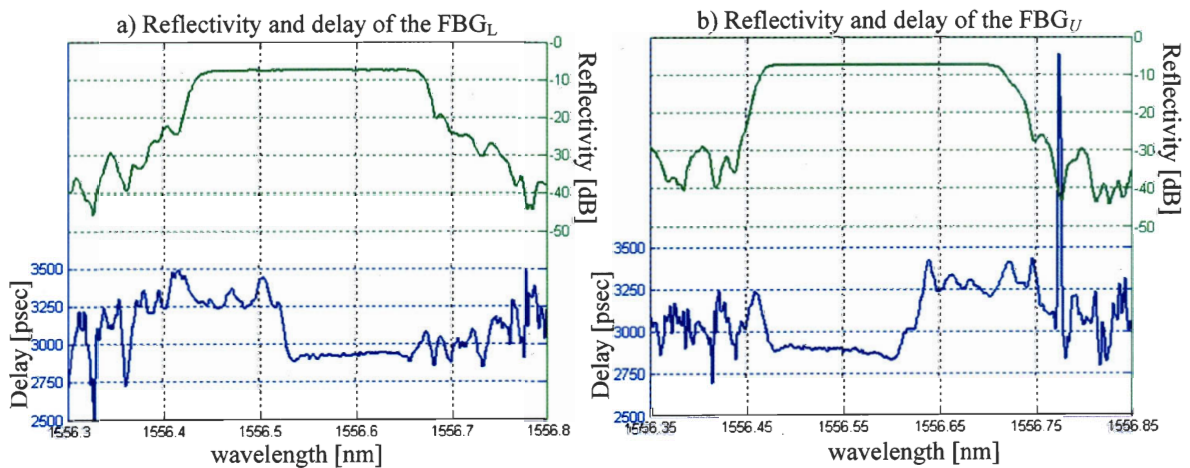


Figure 3-16: Measured reflectivity and delay of the FBG_L (a) and FBG_U (b).

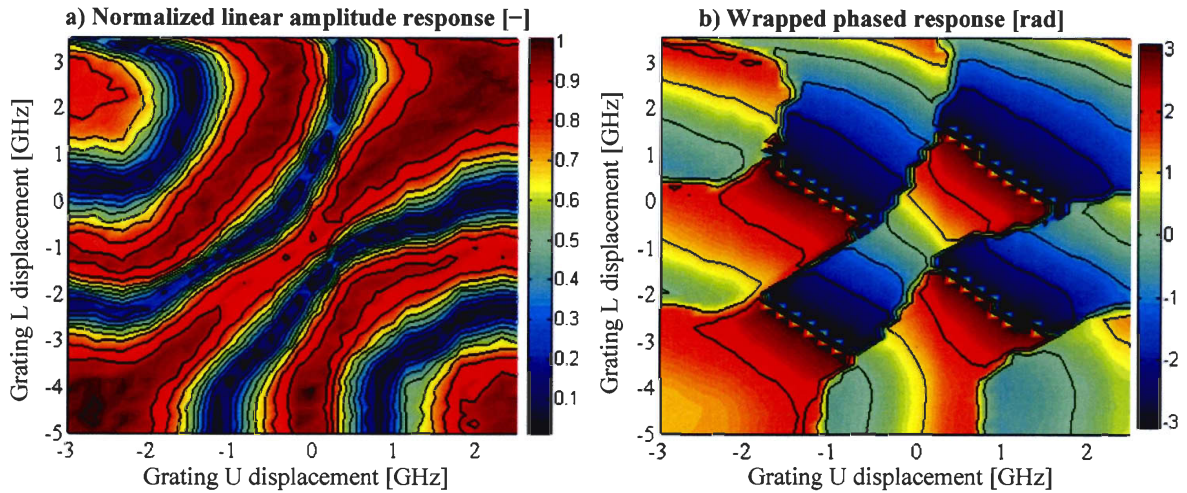


Figure 3-17: Measured amplitude (a) and phase (b) maps of the DG-BF.

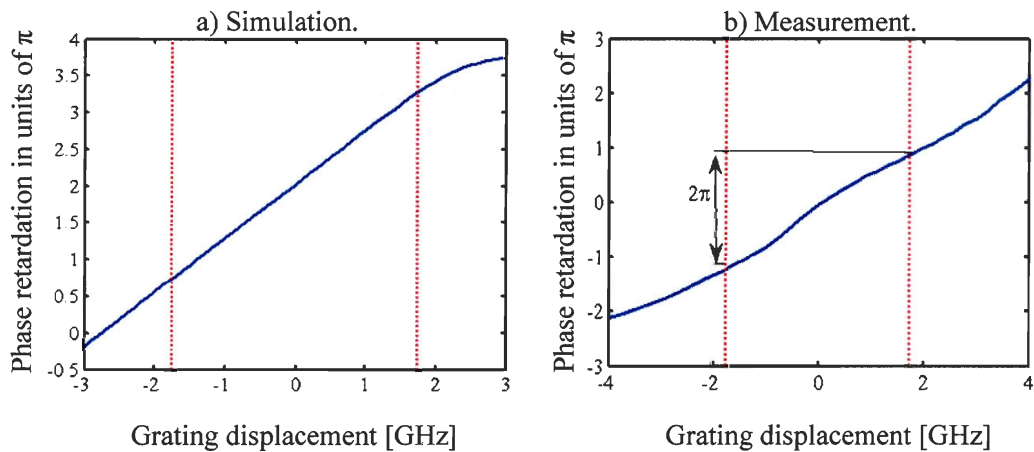


Figure 3-18: Comparison between phase retardation on the secondary diagonal: simulation (a) and measurement (b).

The measurement results for these maps can be obtained, as we did for the single-cavity GT-BF experiment, by shifting the gratings delay and amplitude response with temperature controllers. Figure 3.16 shows the measured delay and reflectivity of the filters that we have fabricated for this measurement. Figure 3.17 depicts the measured amplitude and phase maps. The measurement setup is similar to the single-cavity GT-BF measurement setup depicted in Figure 3.12. The only differences were related to the thermal actuator hardware which was modified for the new length of gratings (for more details see Section

4.2.3) and the temperature controllers for which we employed two channels of multichannel ILX LDC-3908.

Comparison between simulation and measurement confirms the general conformity and good control over the amplitude of the signal for each desirable phase value in a 2π range in a way that, by sweeping on the secondary diagonal from (-1.2, -3) GHz to (1, 1) GHz, we can change the phase of RF signal by more than 2π and for each desired phase value. By tuning in the perpendicular direction we can attenuate the amplitude by at least 10 dB while keeping the phase amount constant. Figure 3.18 compares the phase retardation in simulation and measurement.

a) The Multichannel Solution of DG-BF

The multichannel DG-BF has the configuration depicted in Figure 3.19 and is formed by two cascaded chains of independent gratings: one chain for all the FBG_U filters and the other chain for all FBG_L filters. In each chain, the gratings have 25 GHz wavelength spacing in conformity with the DWDM design goal.

The signal from a multiwavelength source is modulated by a single DSB modulator so that each wavelength carries the signal for a specific array element. Each wavelength is filtered twice by separate FBGs, which are part of two chains of concatenated gratings before transmission over an ROF link. By adjusting the temperature or by stretching each FBG, phase and amplitude of the signal on each wavelength can be controlled independently. This solution minimizes the complexity of the design of filters and ensures that the channels are independent.

The main disadvantage of the proposed configuration is that the minimum length of each chain is N times the length of a single grating (8.5 cm), that is as much as 68 cm for eight channels! Such long chains of gratings, along with the actuators needed for controlling the DG-BF, are not easy to package. Shorter gratings can be designed by increasing the chirp and decreasing the delay step. However, decreasing the step reduces the phase tunability range: in this design the minimum step height needed for a phase tunability range of 2π is about 370 ps. Also, the windowing function used to limit the length of the gratings can be

tighter, trading-off the smoothness of the delay response and the flatness of the amplitude response.

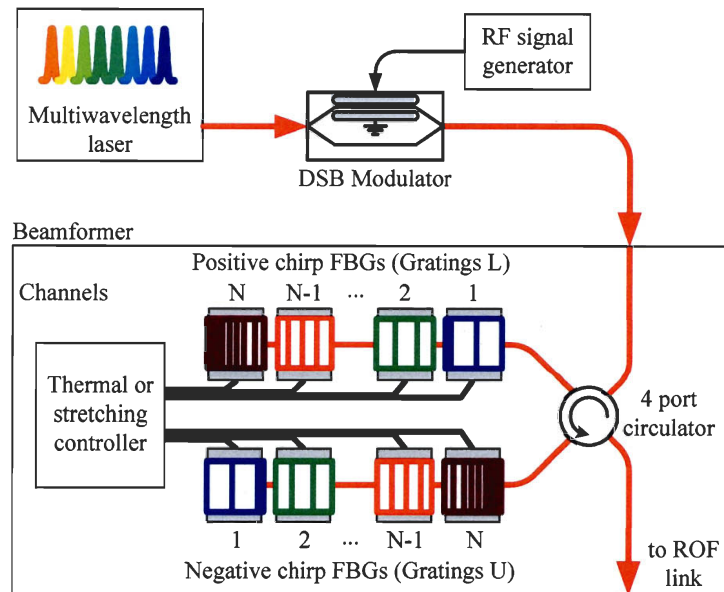


Figure 3-19: The multichannel DG-BF.

3.5. Effect of Beamformer Filters on Signal Quality and Radiation Pattern

FBG-based devices are known to present an imperfect spectral response that introduces some level of amplitude and phase distortion. Although the impact of these ripples on digital communication systems has been widely studied, little has been reported on grating penalty in ROF systems. In addition, the proposed beamformer affects the relative phase of the optical spectrum components, and the study of its impact on a complex signal like IEEE 802.11a/n is indispensable to prove the reliability of this null-steering beamformer in ROF applications for indoor communication. In this section, we focus on one channel and characterize this tunable FBG-based null-steering beamformer by performing error-vector-magnitude (EVM) measurements.

Furthermore, because this device is not true time delay, its bandwidth is limited by the maximum allowable beam squint. We simulate the impact of this limitation on our system and find the amount of error that it can introduce for WLAN applications.

3.5.1. IEEE 802.11 Modulation Format for WLAN Application

Considering the capability of the null-steering beamformer for multiple-input multiple-output (MIMO) applications, the IEEE 802.11n compliant signal would be the best protocol to transmit over this beamformer since it is the most common modulation format that supports MIMO techniques. Unfortunately, this standard was not well-established when we started this project, so we instead check the effect of the beamformer using the IEEE 802.11a format, the established standard working in the 5 GHz band. It supports data rates of 54, 48, 36, 24, 18, 12, 9 and 6 Mbit/s [39].

IEEE 802.11a signal uses a 52-subcarrier orthogonal frequency-division multiplexing (OFDM); multi-level quadrature amplitude modulation (QAM) is employed for modulating data tones. OFDM is a multicarrier transmission technique used in applications related to both wired and wireless communications. The OFDM technique divides the available frequency spectrum into many closely spaced carriers, which are individually modulated by low-rate data streams. The orthogonality between the carriers facilitates the close spacing of carriers. The orthogonality principle implies that each carrier has a null at the center frequency of each of the other carriers in the system while also maintaining an integer number of cycles over a symbol period [39].

3.5.2. Experimental Verification of the Beamformer Effect on Signal Quality

In order to experimentally verify the performance of filters, we generated and transmitted the IEEE 802.11a signal with the highest possible data rate (54 Mb/s) over an ROF link: the signals were composed of frames with a synchronization symbol, a channel-response training symbol, and a payload of 16 OFDM-symbols. In the standard, the maximum transmission rate is achieved using a 64-QAM format that is very sensitive to link noise and intermodulation distortion. Furthermore, the OFDM signals are characterized by a high peak-to-

average-power ratio (PAPR), which increases the signal sensitivity to distortion. Narrow-band signals such as IEEE 802.11a are mostly affected by the third-order intermodulation distortion (ID3), because even-order distortion terms can be filtered in the RF domain. In many ROF links, the optical modulator is the main source of ID3.

To verify the quality of the OFDM signal, EVM measurements were performed. The EVM parameter is

$$EVM_{dB} = 10 \log_{10} \left(\frac{\sum_n |r_n - z_n|^2}{\sum_n |r_n|^2} \right) \quad (3.14)$$

where the vector r represents the inphase and quadrature coefficients of the transmitted 64-QAM symbols and the vector z is the coefficient of the received symbols. The EVM is equal to the ratio of the average power of the error vectors to the root mean square power of the transmitted symbols without any errors. The IEEE 802.11a protocol imposes -25 dB as the maximum allowable EVM value for error-free transmission.

To perform this test, we used a tunable laser source, a MZ modulator, the beamformer and an amplified photodetector. The setup of Figure 3.12 was used for EVM measurements. The RF input to the modulator was provided by a vector signal generator (VSG), and the received signal was fed to a vector signal analyzer (VSA) for the EVM measurement. The electrical back-to-back EVM measurement, with the VSG directly connected to the VSA, was -48 dB. The optical back-to-back EVM measurement at the MZ output was -37 dB. This EVM degradation is expected and arises from MZ third-order distortion. The MZ modulator bias was set at the quadrature point with automatic bias controller. The bias controller module works based on an optical feedback and an internal oscillator trying to lock the operation point on the quadrature point. Due to the numerous measurement points required for a complete map, the whole measurement takes a long time: for the map of Figure 3.20a, a three-day measurement was made. Since the bias of the MZ modulator drifts in a relatively short time (some minutes), using this automatic bias controller was indispensable.

EVM measurement of single-cavity GT-BF: The position of the beamformer delay peaks can be changed independently by using their respective temperature settings as we have done to obtain amplitude and phase measurements. Then several different data frames were generated and transmitted over the ROF link including the beamformer and we measured averaged EVM. The measured map is shown in Figure 3.20a. The EVM measurement along the secondary diagonal is reported in Figure 3.20b. The solid straight lines in this figure correspond to the measured EVM level after the MZ modulator.

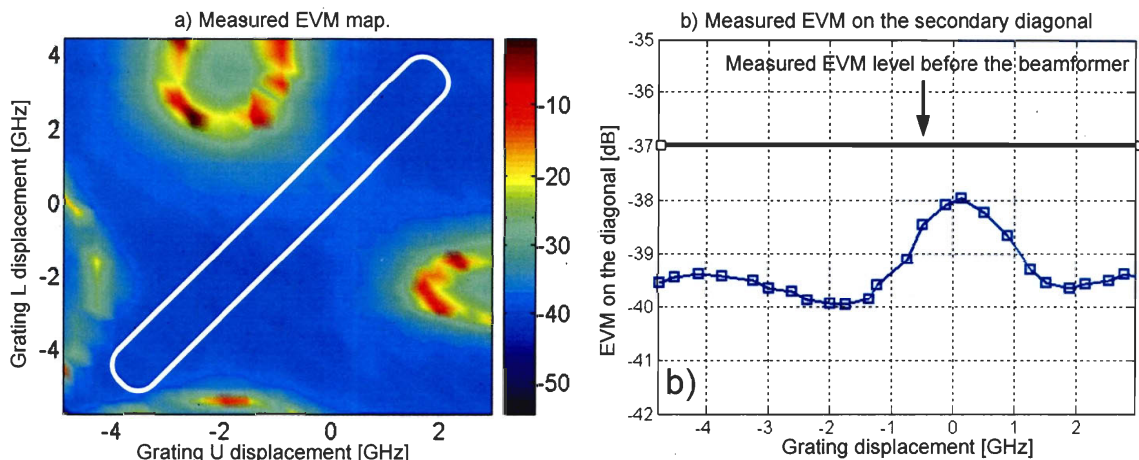


Figure 3-20: Measured EVM response for the single-cavity GT-BF.

Strong attenuation of the signal amplitude (refer to Figure 3.11c) eventually degrades the EVM, as is apparent in the lobes of Figure 3.20a; however in the zone of interest, the EVM is much better than -25 dB and complies with the standard. In addition, the EVM measured after the GT-BF is better than the EVM measured after the MZ modulator (solid straight line), indicating that some compensation of the nonlinearity takes place. It has been reported [40] that, by wisely manipulating the optical spectrum, some of the ID3 generated by the modulator can be suppressed. For instance, fiber dispersion can change the relative phase of different components of the propagating spectrum such that the received ID3 at the fiber end may be less than what is measured at the modulator output. In the GT-BF case, we believe that this results from the different amounts of group delay in the filters experienced by the various ID3 components, leading to partial cancellation of the nonlinear terms.

EVM measurement of DG-BF: The same experimental method was used for characterizing the EVM response of the DG-BF filters to make sure they are well-suited for real ROF applications. Despite the fact that we repeated the measurements several times, we could not accomplish this measurement perfectly because of an unexpected problem related to the interaction between the bias controller module and erbium-doped fiber amplifier (EDFA). This interaction caused a dramatic fluctuation of EVM level and limited the optical back-to-back result to -33 dB. We did not see this interaction at the time of the EVM experiment for GT-BF and we conclude that the bias controller was probably damaged.

Although we could not precisely characterize the EVM response over the entire map due to this problem, the EVM was measured over the secondary diagonal by manually setting the bias. The measured EVM was less than -37 dB, which was much better than the threshold of error-free transmission (-25 dB). It proves that the DG-BF does not distort the signal.

3.5.3. Beam Squint

As we already mentioned this null-steering FBG-based beamformer acts on the signal phase instead of time delay so this is not a TTD system. The phase shift is constant over the signal bandwidth and not frequency dependent, as it would be in a TTD beamformer and this causes the beam squint. A phase shift within $(0, 2\pi)$ is sufficient as this beamformer is designed to work with narrowband signals. When the ideal antenna phase value exceeds this range, it is folded back in. This is a second source of error on the radiation diagram, because far-field interference of the antenna patterns does not occur on the same wave-front for all the antennas.

In the special case of simple beam-steering, we simulated the maximum error on the beam pointing direction and on the HPBW as a function of the signal frequency and steering-angle, taking into account both the beam squint effect and the phase wrapping. For that, we calculated the previously-mentioned errors within a 100 MHz signal bandwidth at 5 GHz for an array composed of eight antennas with half-wave spacing. The results are shown in Figure 3.21. The maximum pointing error for the IEEE 802.11a 20 MHz band for 75° steering angle is 0.43° , that is, only 1.3% of the HPBW in that pointing direction (see Figure

3.21c). This amount is absolutely acceptable for most communication systems, especially in indoor environments.

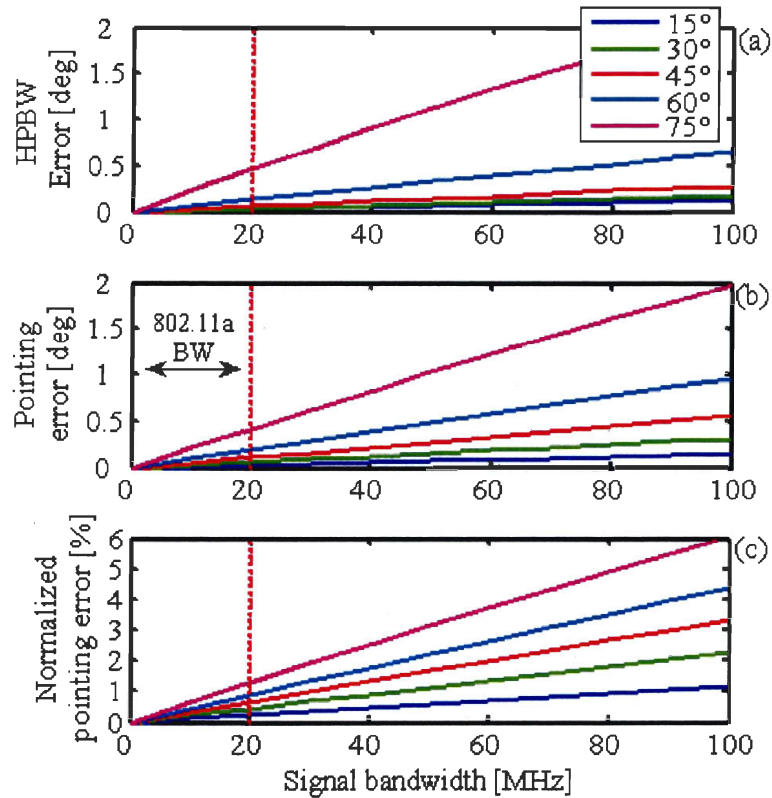


Figure 3-21: Errors in definition of the radiation diagram: a) error on the HPBW; b) error on the pointing direction; c) error percentage on the pointing direction normalized by the beamwidth.

3.6. Conclusion

In this chapter, we introduced some previous TTD optical beamforming techniques and we discussed their performance and drawbacks. These TTD systems were implemented either with fiber grating prism, or CFBG and multiwavelength source, or tunable CFBGs. We described the operation of our phased-based optical beamformer, the design procedure and its evolution. We confirmed via simulation and measurement the control of both amplitude and phase of the modulated RF signal. Finally, the impact on signal quality of optical filters was verified by transmitting the IEEE 802.11a signal over the beamformer. This experi-

mental result proved that the beamformer, as a part of ROF link, does not distort the modulated signals.

In the next chapter, we will exploit the described beamformer module in a complete ROF link respecting DWDM configuration to demonstrate the beamforming by measuring the PAA radiation pattern.

Chapter 4

ROF Link Implementation and Radiation Pattern Measurement

4.1. Introduction

After finalizing the design for DG-BF optical filters and demonstrating an independent control over the phase and amplitude for a single channel via simulation and measurement, we are now prepared to perform wireless beamforming. The wireless link consists of a four-element array antenna as the transmitter, a single-element antenna as the receiver and an additive white Gaussian channel in between. These antennas have been designed and fabricated using methods described in the second chapter. As discussed in Section 3.4.2, the

beamformer consists of two chains of independent gratings, one with positive chirp for all lower sideband filters and the other one with negative chirp for all upper sideband filters. In order to perform the beamforming via a four-element PAA, each chain is formed by four cascaded individual FBGs with similar design though operating at different wavelengths. To achieve the same accumulated delay for all channels, the gratings are placed uniformly with inverse order in two chains. We measured the delay with an optical network analyzer as we were splicing the FBGs; uniform spacing with a precision of 1 mm was attained.

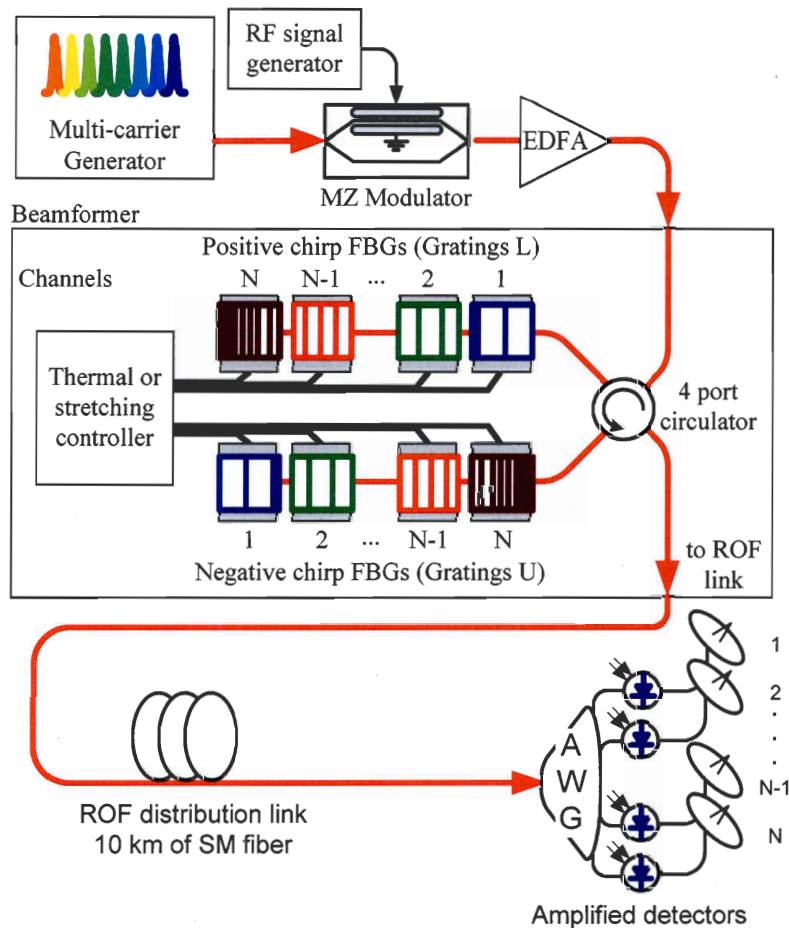


Figure 4-1: Multi-channel WLAN-ROF link including DG-BF.

In this chapter, we briefly describe the different components in the ROF link. We perform link calibration and obtain the calibration parameters for each channel. The radiation pattern measurement technique is explained, and we demonstrate the beam-steering and null-

steering capabilities of the DG-BF by comparing simulation and measurement results. We discuss the source of errors, and the advantages and disadvantages of our beamformer.

4.2. ROF Link Architecture and Hardware

The complete link is depicted in Figure 4.1. As we already mentioned, this link is based on DWDM configuration with channel spacing of 25 GHz. The wavelengths from a multi-carrier source are modulated (by the DSB technique) with a single MZ modulator driven by a 5 GHz RF carrier. Each wavelength feeds one array element. The modulated wavelengths are optically amplified by an EDFA and then filtered by the DG-BF. Each channel is filtered twice by separate FBGs, which are part of two chains of concatenated gratings. By adjusting the temperature of each FBG, the phase and amplitude of the signal on each wavelength can be controlled independently (see Section 3.4). Afterward, the wavelengths pass through the distribution link consisting of 10 km of standard single-mode fiber (SMF) and then demultiplexed by an AWG with channel a spacing of 25 GHz. Each branch goes through an amplified PD to feed the respective antenna.

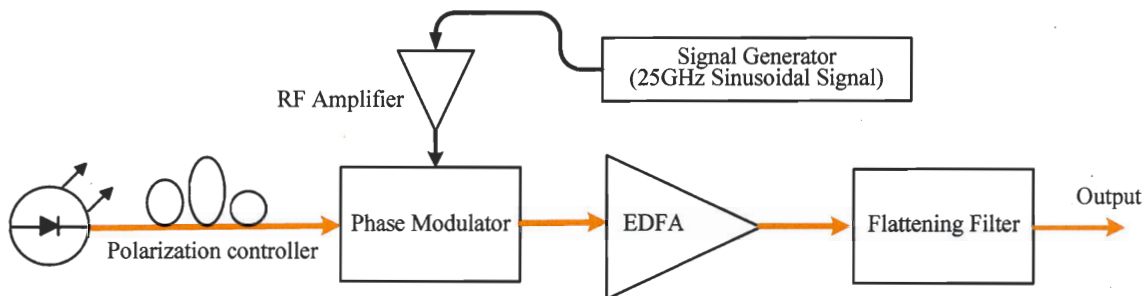


Figure 4-2: Schematic diagram for the multi-carrier generator.

4.2.1. Multi-carrier Laser Source

We exploited a novel multi-carrier generator [42] as the multiwavelength optical source. This simple method produces a flattened multi-carrier spectrum by combining a phase modulated laser signal with an apodized CFBG that is carefully tailored to equalize the optical carrier power. The CFBG is a transmission grating with an apodized index profile designed with an iterative algorithm. After the equalizing filter, less than 2.7 dB peak-to-peak deviation was found amongst seven optical carriers spaced by 25 GHz and the optical sig-

nal-to-noise ratio (OSNR) was better than 40 dB. The setup for the multi-carrier laser source is depicted in Figure 4.2 showing the multi-carrier generator composed of a continuous wave (CW) laser, a phase modulator (PM) and a CFBG for flattening all the carriers and one EDFA to compensate the power loss in PM and CFBG. In the multi-carrier generator, the polarization states of all carriers are the same. This enables the generated carriers to be perfectly modulated with a single MZ modulator placed after one polarization controller.

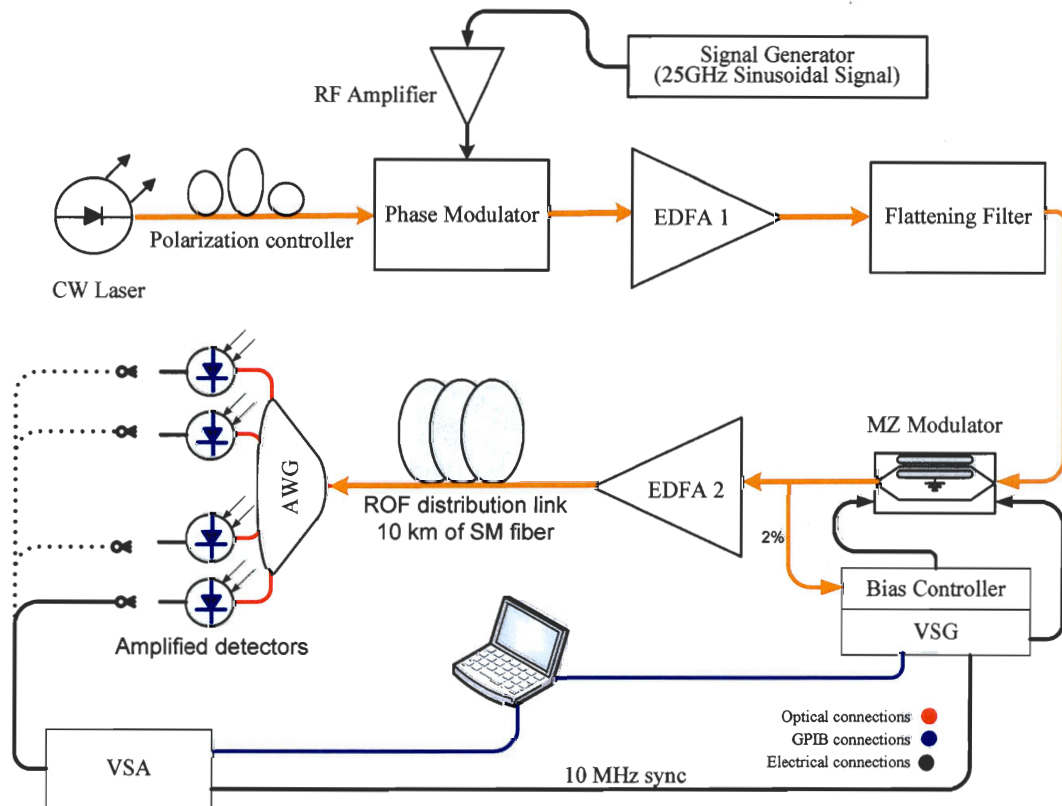


Figure 4-3: Measurement setup for examining the signal quality after transmission over the ROF link using a multi-carrier generator. CW laser: Phonetics tunics-BT; Modulator: JDS OC-1; EDFA 1: INO FAD-180; EDFA 2: JDS OAB1552+1FA0; Phase Modulator: EOspace PM-0k5-20; Signal Generator: Agilent 83731B; VSG: Agilent E4438C; Bias Controller: YY-Labs Mini-MBC-2; EVM Analyzer: Agilent E4440A; Amplified Detector: Agilent 11982A LCA; AWG: KyLia Mics-32/025.

We characterized the quality of the multi-carrier generator by modulating all the carriers with an IEEE 802.11a signal and measuring the EVM level for each carrier, to be sure that additive noise or distortion introduced by this source does not have a significant effect on WLAN-ROF transmission quality. To execute the test, we assembled an optical back-to-

back setup in which the generated wavelengths were modulated by a single MZ modulator biased at the quadrature point. The RF input to the modulator was provided by the VSG. All modulated wavelengths were passed through the distribution link consisting of 10 km of SMF and were demultiplexed by an AWG. Each demultiplexed signal was sent to an amplified photodetector and the detected RF signal was fed to the VSA for EVM measurement. The setup is illustrated in Figure 4.3. The measured EVM values for each wavelength are shown in Figure 4.4. Since all measured EVM values are less than -25 dB, the threshold of error-free transmission, we conclude that the multi-carrier laser can generate and transmit IEEE 802.11 signals with an acceptable quality. Furthermore, the power and wavelength spacing of this source was completely stable, and for a three-day continuous test it did not show any fluctuation, change or instability. However, the achieved flattening was not perfect as one could see in Figure 4.4. Its effect on the whole link can be compensated by either optical amplification or power regulation as will be explained in Section 4.3.

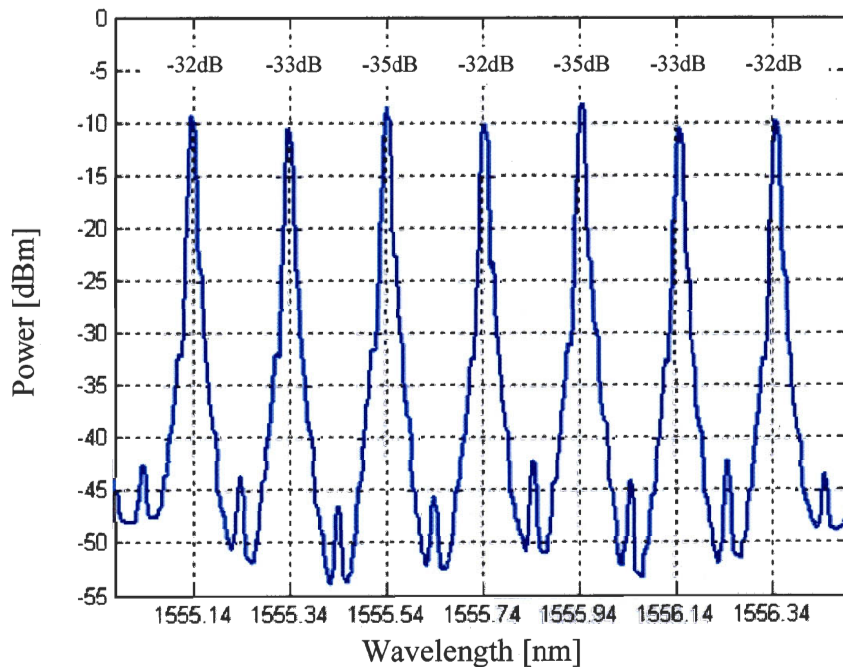


Figure 4-4: Measured optical spectrum and corresponding EVM values.

4.2.2. RF-Gain Improvement and Distortion Compensation by Employing MZ Modulator Bias Optimization

In many wideband optical links, MZ modulator bias is set at the quadrature point in order to increase modulation efficiency and reduce second-order distortion [43]. This bias setting gives maximum spurious-free dynamic-range (SFDR) and RF power gain in wideband links. In contrast with wideband systems, suboctave ROF links show no superposition between the bands occupied by the fundamental transmitted frequency and the harmonics generated by the nonlinearities of the modulator. Thus, suboctave systems are mostly affected by ID3, because second-order harmonic distortion terms are out of band and can be filtered in the RF domain.

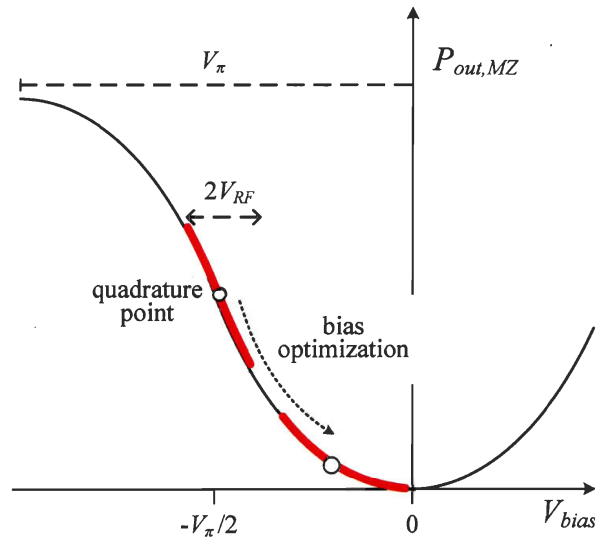


Figure 4-5: Transfer function of the MZ modulator with $V_{bias} = 0$ at the minimum transmission point.

In [44], a novel method was proposed to optimize the RF gain in narrowband ROF links employing a MZ modulator followed by an EDFA for amplification. Optimization is achieved by control of the modulator bias in order to improve the signal optical-modulation depth (OMD). Thus, for a given modulation amplitude, the optical signal has a reduced mean optical power and can access the small signal gain of the EDFA. This unsaturated gain is higher than the saturated one, thereby significantly increasing the RF gain of the

link. Figure 4.5 illustrates the bias point usually used to optimize the ROF link. In addition, [44] proves that the same optimized bias point leads to minimum accumulated ID3 in the signal band. In other words, the signal quality can be improved by changing the bias point from quadrature to reduce additive distortion to the signal.

Since the ROF link depicted in Figure 4.1 is externally modulated by a MZ modulator and has been followed by an EDFA, we take advantage of this technique. By optimizing the MZ modulator bias in the setup of Figure 4.3, a minimum RF gain of 12 dB for each channel was observed while an EVM level of -36 dB for all wavelengths was achieved. Comparing this value with the EVM levels of Figure 4.4, an error reduction of 1 dB to 4 dB for the received signal is seen because of the ID3 compensation.

4.2.3. FBG Actuators

As discussed in the third chapter, to tune the response of the FBG-based filters we need to apply the temperature/stress over the gratings, independently. Considering the available equipment in the laboratory, we chose temperature tuning based on the thermoelectric Peltier device.

Peltier devices, also known as thermoelectric modules, are small solid-state devices that function as heat pumps and can be used as both heaters and coolers. A typical unit is a few millimeters thick by a few millimeters to a few centimeters square. It is a sandwich formed by two ceramic plates with an array of small Bismuth Telluride cubes in between. The system has two sections: a cold side and a hot side. The cold side is commonly used to cool an object such as a photodetector or a FBG. The hot side consists of a heat sink. When a DC current is applied, heat is moved from one side of the device to the other, where heat is removed with a heat sink. If the current is reversed the device makes an excellent heater. Peltier devices are not very efficient and can draw amps of current. This disadvantage is more than offset by the advantages of no moving parts, no Freon refrigerant, no noise, no vibration, very small size, long life, precise temperature control, etc.

In the DG-BF application, considering the 85 mm long FBGs, a large surface Peltier is required resulting in high power consumption. For running this system we used an eight-

channel temperature controller that could provide 1.5 A current for each channel to have a reasonably fast (a few seconds per each degree) and stable thermal control. It is worth mentioning that this configuration was a quick solution based on the available facilities in the laboratory and commercial solutions can become more efficient.

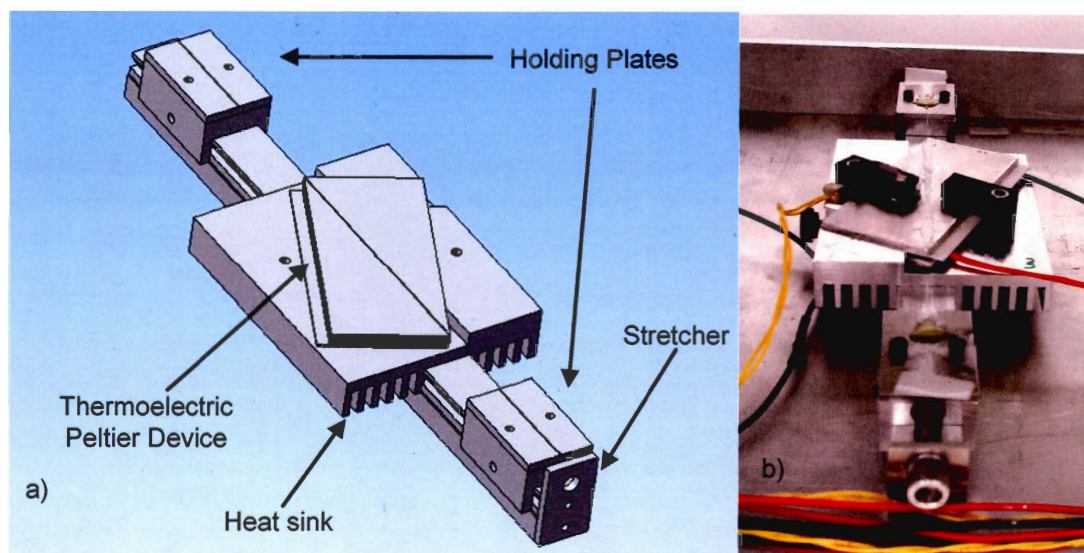


Figure 4-6: Schematic diagram (a) and a fabricated version (b) of each FBG actuator.

We were not able to write each FBG in its appropriate channel wavelength because of the mechanical instabilities in our FBG writing facilities for writing long gratings. To avoid extreme temperature adjustment, we shifted the filters' response to the desired channel wavelength by strain tuning. To do so, we fabricated all FBGs in the shortest possible wavelength response and then by applying proper amount of stretch on each FBG, we shifted the spectrum to the longer wavelengths. Figure 4.6 shows the layout of one FBG actuator with strain and temperature tuning capabilities that we fabricated.

Strain tuning requires the fiber to be fixed and this is usually done by using fiber holders with mechanical clamps. Since N gratings are cascaded for the N -element PAA beamforming application, we could not use fiber clamps due to their associated loss (around 2 dB for each clamp). Therefore the fibers were fixed by gluing them (with epoxy glue) on the two holding plates shown in Figure 4.6. Gluing on the surface of the temperature controller was

not successful since the amount of stretch will be affected by surface temperature because of the surface expansion and contraction.

Following the previously-mentioned considerations, we present the schematic diagram of the actuators for a four-channel beamformer in Figure 4.7. This system controls one chain of filters and the other chain needs a similar device.

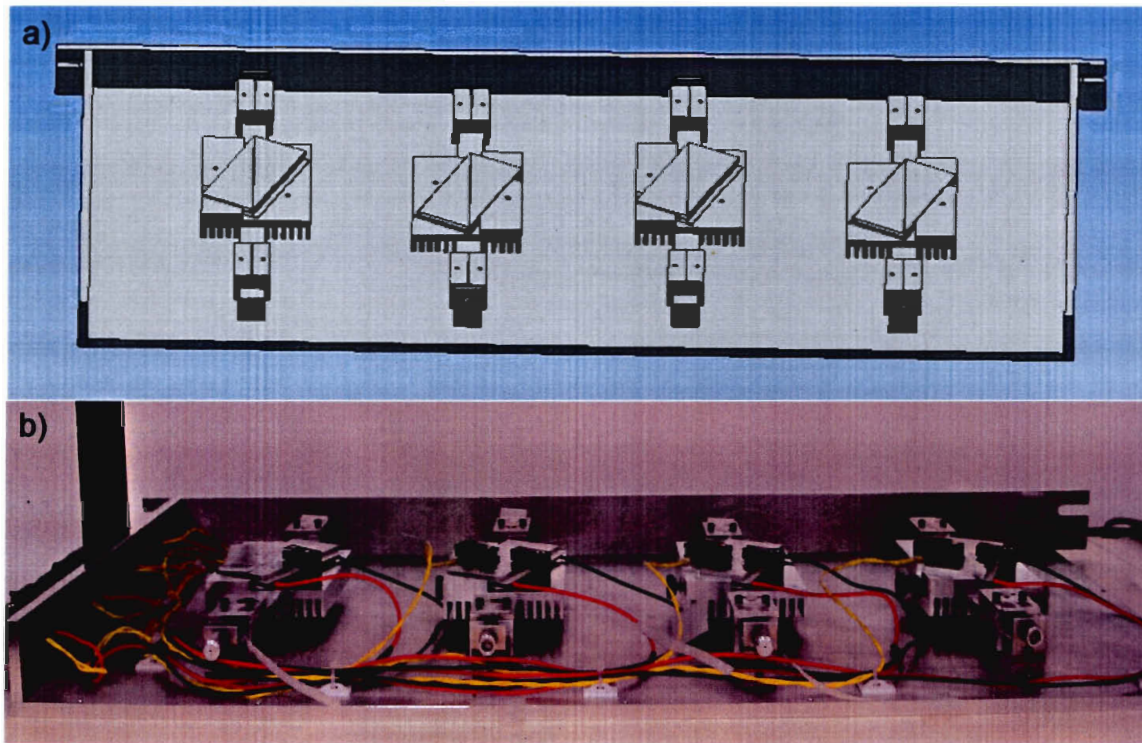


Figure 4-7: Schematic diagram (a) and the fabricated version (b) of the actuators for each chain of DG-BF designed for four-channel application.

4.2.4. Appropriate Optical Detection Stage

Optical-to-wireless transceivers for the base stations in ROF links face major challenges in improving signal-to-noise ratio (SNR) and increasing transmitted RF power. To achieve the RF power suitable for wireless transmission, a power amplifier (PA) is usually used in the base station inline with the PD, which results in additional cost, noise, and distortion. For example, when transmitting an IEEE 802.11 compliant signal, considering its high PAPR, the PA stage can clip the signal and dramatically distort it. To avoid clipping, the PA is di-

mentioned to have 1 dB compression power several times higher than the mean power of the transmitted OFDM signal, which is very inefficient.

As we discussed in Section 4.2.2, the ROF link can result in high RF gain and ID3 cancellation by optimizing the bias of an external MZ modulator. However, in [44] the power had to be attenuated optically at the last stage of the link in order to respect the maximum input power of the PD. By using a high-power linear PD, we would not need to attenuate the optical power and via bias optimization technique, the PA stage can be omitted from the ROF link. Use of high-power linear PDs in typical WLAN-ROF links has been introduced and their effect on signal quality was characterized in [45].

Unfortunately, these components were not available at the experiment time and so we used a simple circuit (see Figure 4.8) based on four standard photodiodes (JDS EPM-745) as the detection part. Since these regular PDs do not support high-power applications, an amplification stage consisting of four PAs (Mini-Circuits ZX60-8008E-S+) follows the PDs to provide enough RF power for wireless radiation.

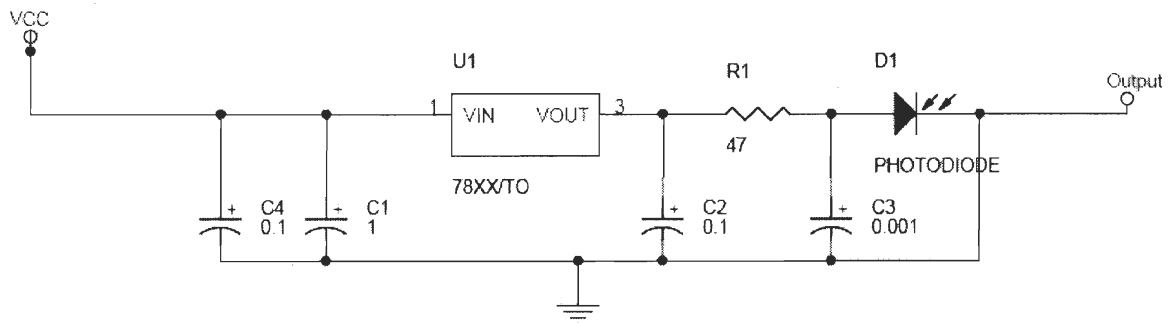


Figure 4-8: Electronic circuit for a photodiode working as a single-channel detection stage.

The resistance R_1 in Figure 4.8 has been chosen by trial-and-error to simultaneously match the output impedance of the PD to the characteristic impedance of the coaxial cable (50Ω) and control the PD bias current. We empirically found that 47Ω was the optimum value to maximize RF power delivery. To check the impedance matching, we used a triple-stub microwave transformer in which three stubs are placed a quarter-wavelength apart on a coaxial line and adjusted in length to compensate for impedance mismatch. We chose the resis-

tance R_1 in such a way that the delivered power with and without the triple-stub is the same, implying that the impedance matching of the PD is optimized.

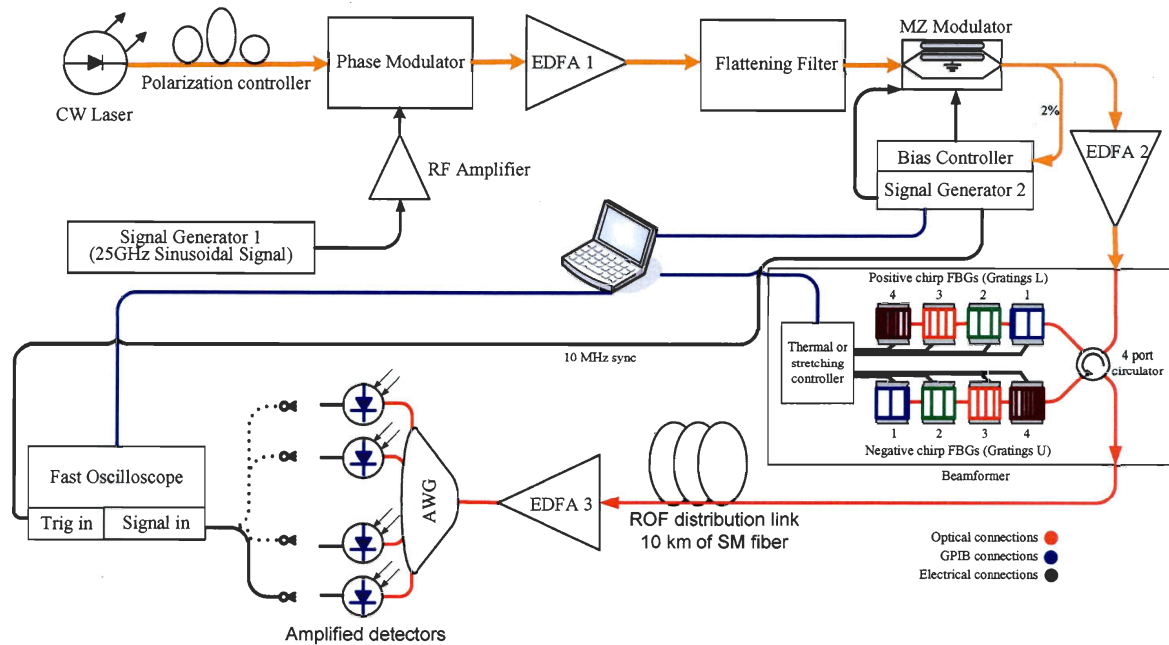


Figure 4-9: Schematic diagram of the setup used for multichannel calibration. JDS OC-1; EDFA 1: INO FAD-180; EDFA 2 & EDFA 3: JDS OAB1552+1FA0; Switch: JDS SB series; Thermal controller: ILX LDC-3908; Signal Generator 1: Agilent 3731B; Phase Modulator: Eospace 0k5-20; Signal Generator 2: Agilent E4438C; Fast Oscilloscope: Agilent DSO81004B Infiniium, real time, 10 GHz bandwidth; Bias Controller: YY-Labs Mini-MBC-2; Amplified Detector: Agilent Lightwave Converter; AWG: KyLia Mics-32/025.

4.3. Link Calibration

To operate this beamformer, we need to know the phase and amplitude response of the cascaded filters as a function of the temperature setting in order to be able to set the complex excitation for each channel. In other words, a processor in the CO would determine the desired phase and amplitude for each channel and generate the appropriate Peltier control signals. To obtain the calibration maps of these control signals, a setup similar to that in Figure 3.12 is developed for multichannel operation. We do not use an optical network analyzer, as the filters can be directly calibrated versus the actuating adjustment values instead of frequency shift. The multichannel calibration setup is shown in Figure 4.9.

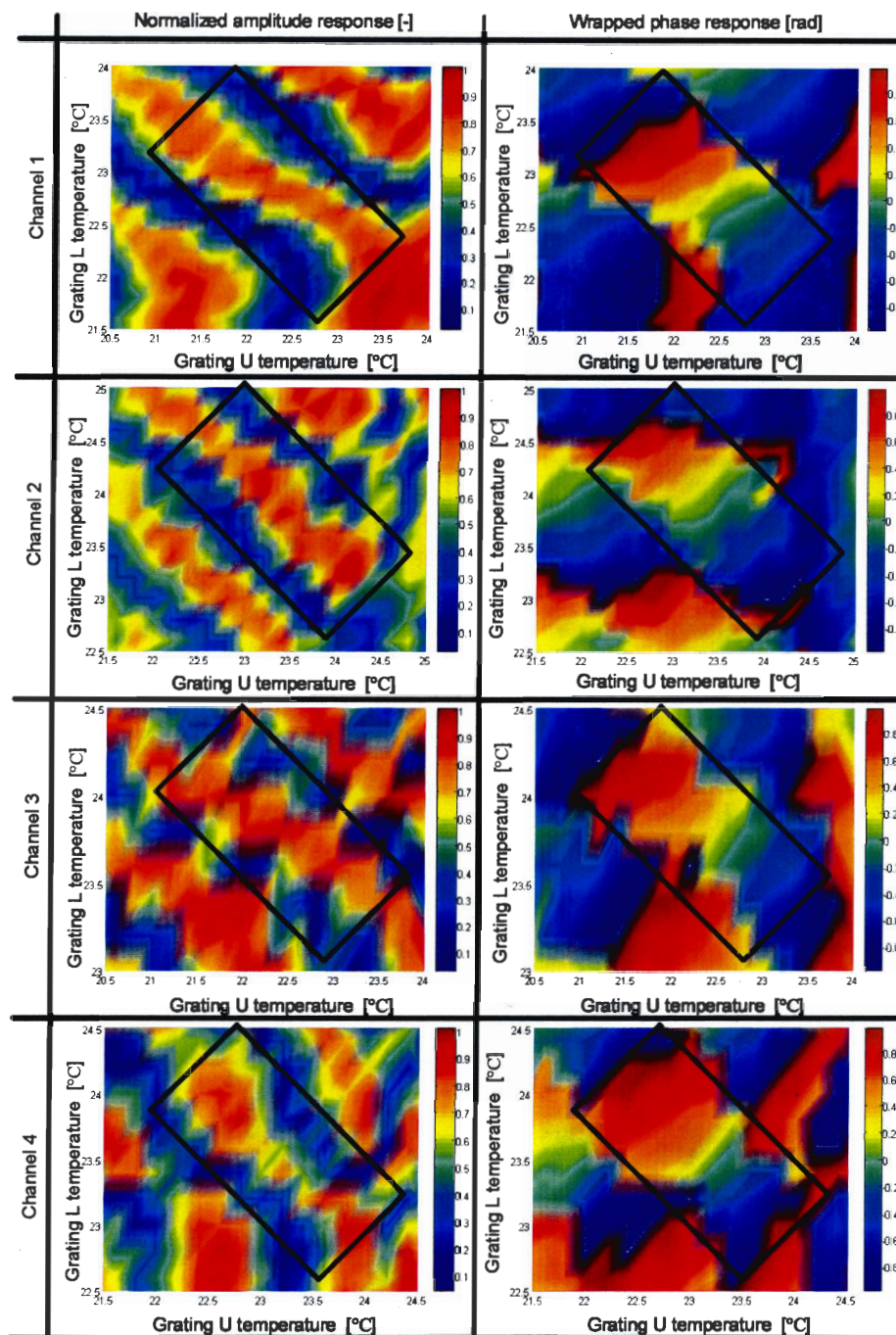


Figure 4-10: Calibration amplitude and phase information versus temperature adjustment for all channels: channel 1: 1555.14nm, channel 2: 1555.34nm, channel 3: 1555.54 and channel 4: 1555.74nm.

The measured maps for all four channels are reported in Figure 4.10 and the rectangles illustrate the zones of interest. Phase maps confirm that 2π phase tunability is achieved for all channels, as we expected based on arguments in Section 3.3.3.

The measured maps for all four channels are reported in Figure 4.10 and the rectangles illustrate the zones of interest. Phase maps confirm that 2π phase tunability is achieved for all channels, as we expected based on arguments in Section 3.3.3.

When comparing the amplitude responses with Figure 3.17a, we see that the shapes for the third and fourth channels are distorted. The differences between the new measurement setup and the previous one are the addition of a ROF distribution link, the insertion loss of several gratings in a cascade and the application of strain on the FBG-based filters. We recalibrated the system without the distribution link and the same phenomenon was still observed. Furthermore, considering that the filters operate at different wavelengths, the fact that gratings are cascaded along adjacent gratings should not have any impact except for a negligible loss. The only remaining possible source of discrepancy is that the filters are stretched. As was already mentioned, we apply a strain to shift the filter response to the channel center wavelength since all the filters have been fabricated for the shortest possible wavelength. Theoretically, if the stretch is applied uniformly over the grating length, a linear spectrum shift to higher wavelength is expected. To verify this, we performed a simple test by choosing one of the gratings and measuring its group delay response under different applied strains. Then, we calculated the cumulative phase of these measured group delay responses using (3.8). In this way, we could see the impact of strain on the filter phase tunability. Figure 4.11 depicts the cumulative phase response versus frequency displacement for one of the FBGs. As one can see, the curves are very similar which indicate that the strain does not have any side effect on the filter response.

Other effects such as slipping of the fiber in its jacket over time and interaction between thermal actuating and stretching may be the cause of this phenomenon. This explanation seems cogent once we consider the increase in quality degradation of amplitude maps for higher wavelengths. For commercial applications, one possible solution would be the direct fabrication of each grating for its respective channel wavelength. In this way, there is no need to apply stretch on the filters and the same non-distorted amplitude response as Figure 3.17a is expected.

To validate steering capability, we performed a fast calibration by applying a symmetric shift of the group delay responses versus modulation sidebands. From Section 3.4, we ex-

points are measured in comparison with a complete map measurement; the partial calibration will suffer less from measurement glitches and unstable stretch effect. The results are shown in Figure 4.12 illustrating the unwrapped phase retardation and amplitude variations versus temperature of the two corresponding gratings for each channel. As one can see, a phase tunability of more than 2π is easily achievable within 1.6° of Celsius temperature deviation for all channels. The flatness of the amplitude responses degrades as the strain increases (higher channel number) with maximum amplitude variation of 0.5 dB, 0.7 dB, 0.9 dB and 1.6 dB respectively.

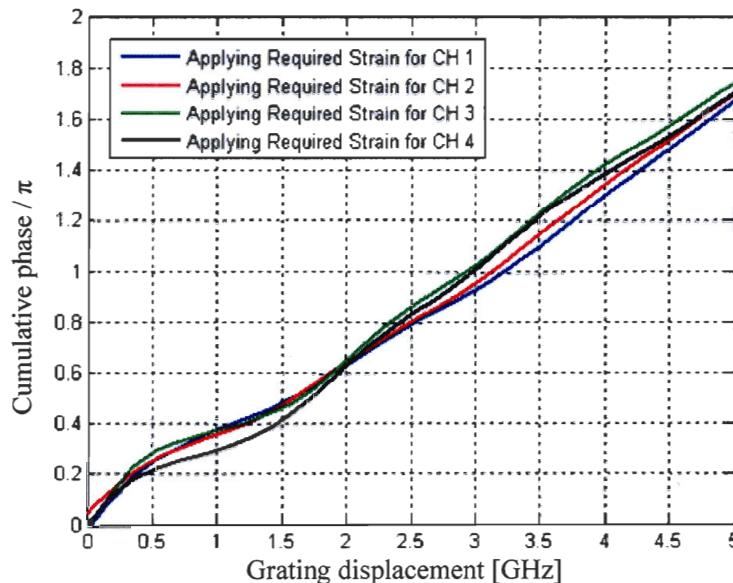


Figure 4-11: Cumulative phase versus grating displacement of the FBG_Ls under different strains.

Besides optical calibration, the system must also be calibrated in the RF domain. Since we designed and assembled all PDs, PAs and antennas similarly for the four channels, we do not expect to see any difference of power loss (power gain) amongst them in the RF domain. Some disparities may originate from slight differences in the responsivity of PDs, resistance of PDs (R_1 in Figure 4.8) and RF amplifier performance. In addition, different RF connections and coaxial cables can be another source of irregularity. A maximum RF asymmetry of 4 dB was recorded. In addition, a 2.7 dB power difference existed between the carriers in the multi-carrier generator (see Section 4.2.1). To overcome these problems, power regulation was realized by a set of proper attenuations before PDs.

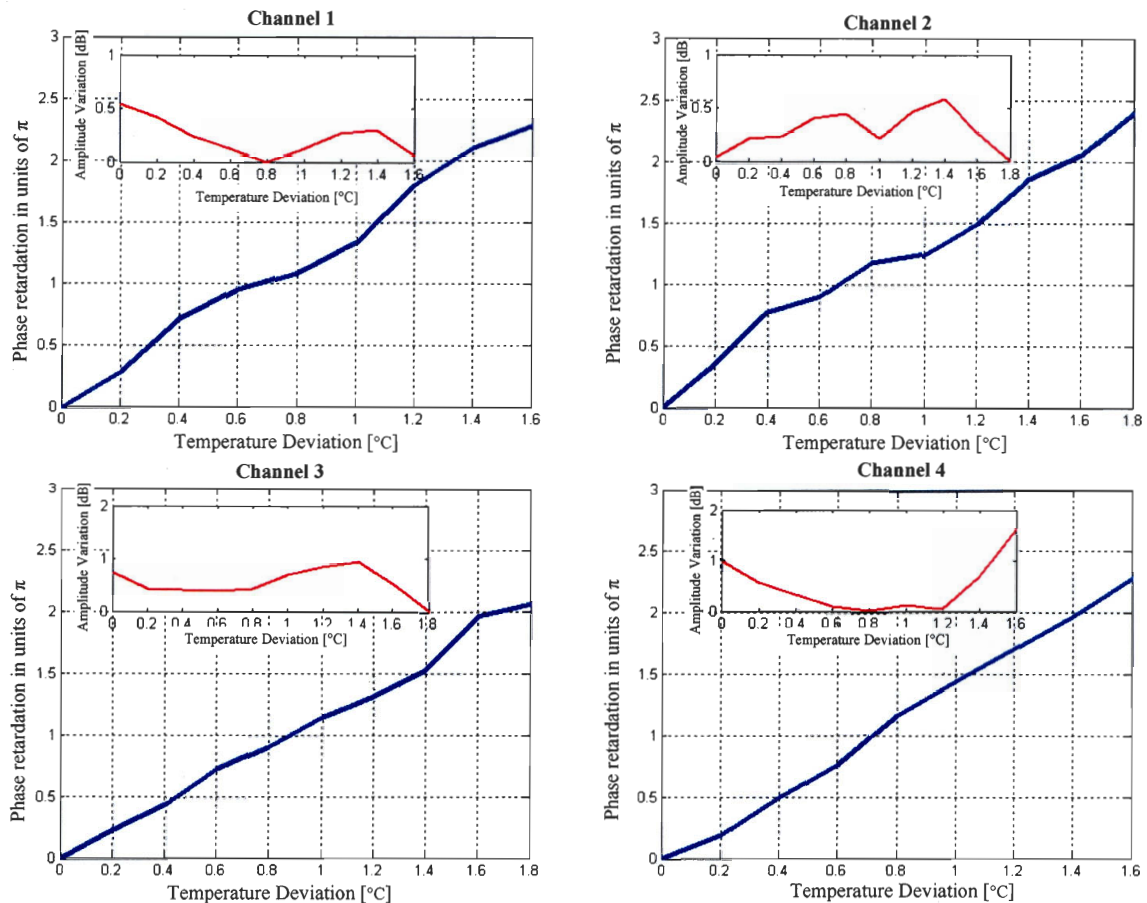


Figure 4-12: Measured unwrapped phase retardation and amplitude variation versus symmetric temperature deviation of the two corresponding gratings for each channel.

4.4. Radiation Pattern Simulation and Measurement

The radiation pattern of the array antenna is determined by the radiation patterns of the individual elements, their orientation in space and the amplitude and phase of the feeding currents. If each array element is an omnidirectional source, the radiation pattern obtained will be solely dependent on the array geometry and the feeding currents and will be exactly the array factor. If the elements of the array are similar and if they are directional, the radiation pattern is computed from the principle of pattern multiplication as the product of the array factor and the individual element pattern. Hence, the array factor can be easily computed from the array pattern and the single-element pattern.

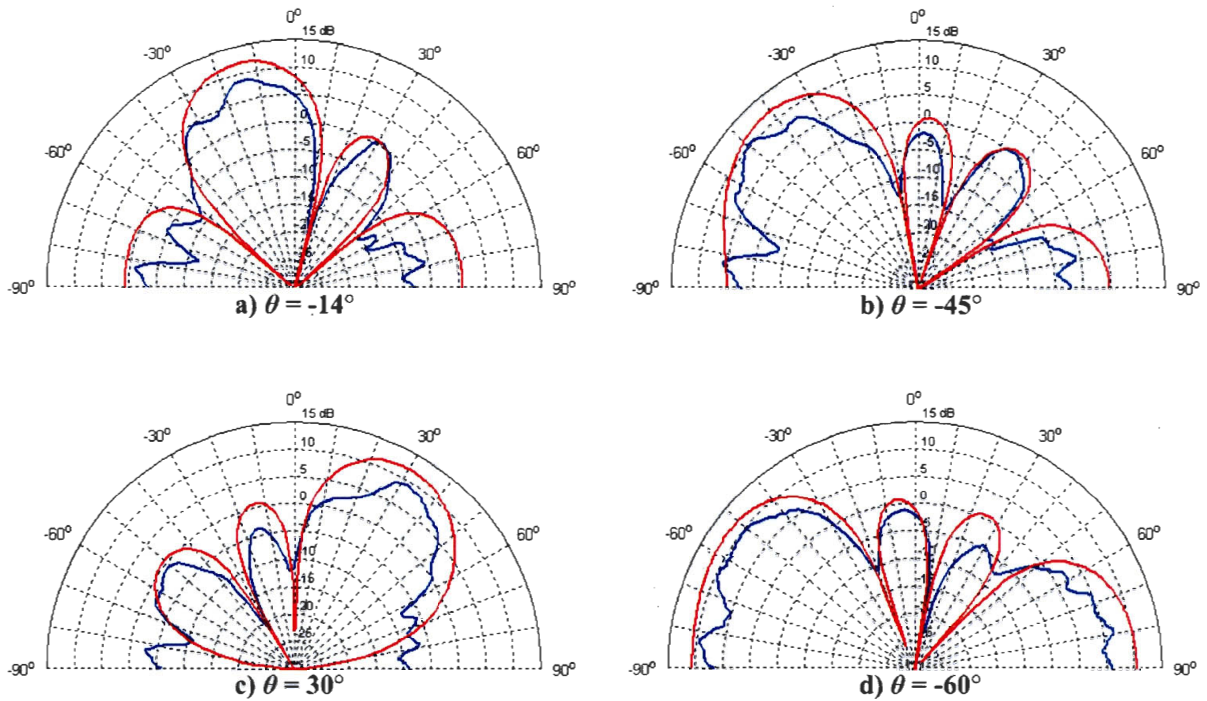


Figure 4-13: Measured (blue curves) and simulated (red curves) radiation pattern diagrams of a four-element array with half-wave spacing for pointing angles of: a) -14° , b) -45° , c) 30° and d) -60° .

Considering the complicated optical setup, we were forced to perform pattern measurement in the ROF laboratory without moving the setup to an anechoic chamber. We arranged pieces of RF absorbers on the floor and around the wireless setup to minimize reflections. To prove the concept of beam-steering with this novel optical beamformer, some examples are simulated and measured. The pattern measurement setup is based on a rotating transmitter and a fixed receiver. Since the beamformer is tested in transmit mode, we placed and fixed the detection part, RF amplification stage and PAA on a plate fixed on the shaft of a stepper motor (Applied-Motion HT23-393). A single antenna (similar to each element in the array) was used as the fixed receiver. We chose a 1 m distance between transmitter and receiver antennas to both meet the far-field range condition and reduce the impact of reflections. For each set of element excitations, we rotated the transmitter side for 180 steps covering 180° of the front side of the array; for each step the received RF power in the receiver was measured by a VSA and saved. The speed and delay time for each rotation step was chosen empirically in support of stable power acquisitions. The measurement and simulation results are shown in Figure 4.13 for different pointing angles.

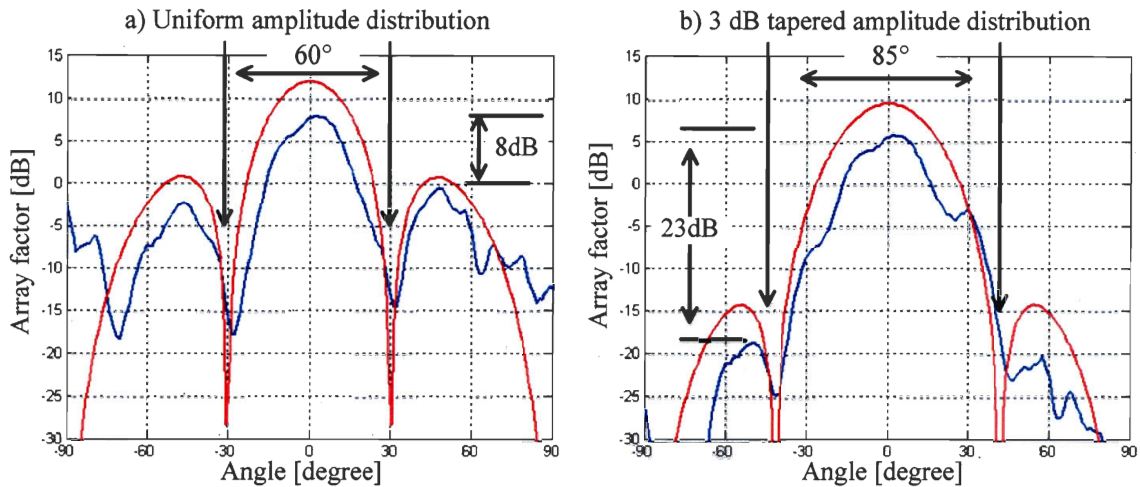


Figure 4-14: Simulation (red curves) and measurement (blue curves) of the radiation pattern diagram for a four-element array with half-wave spacing while pointing at 0° using the uniform (a) and 3 dB tapered (b) amplitude distribution.

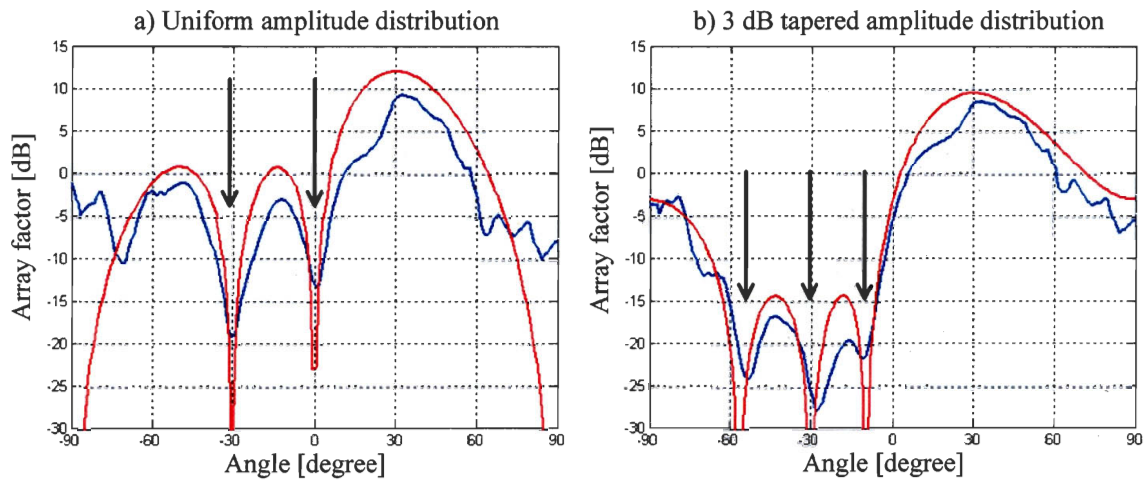


Figure 4-15: Simulation (red curves) and measurement (blue curves) of the radiation pattern diagram for a four-element array with half-wave spacing while pointing at 30° using the uniform (a) and 3 dB tapered (b) amplitude distribution.

The measurement results are in general agreement with simulations and confirm the beam-steering capability even for the extreme beam direction of -60° . For all examples, a slight difference of between 4° and 8° in pointing angle can be found. This amount may be related to imperfections in adjusting the absolute phase value for each element. Lower gain in all measured traces is probably due to the errors in amplitude and phase adjustment or unex-

The measurement results are in general agreement with simulations and confirm the beam-steering capability even for the extreme beam direction of -60° . For all examples, a slight difference of between 4° and 8° in pointing angle can be found. This amount may be related to imperfections in adjusting the absolute phase value for each element. Lower gain in all measured traces is probably due to the errors in amplitude and phase adjustment or unexpected loss in some radiators. Due to the inaccurate absorber positioning and performance, reflection may still influence the patterns. Another important reason for the observed differences is mutual coupling between array elements. Each array element while radiating acts as a receiver for adjacent array elements. Effects from this coupling behavior have been seen in the input impedance of the antennas [7]. The coupling also affects the radiation pattern of an array by disturbing the current distribution of the adjacent elements [7], thereby perturbing the radiation pattern. The impact of mutual coupling depends on the radiation pattern of the other elements, their excitation and the radiated power level. Furthermore, the mutual coupling effect was shown to degrade the impedance matching quality and signal to interference-plus-noise ratio (SINR) significantly, especially when the interelement spacing is decreased [46]. Some methods to improve the antenna design and to eliminate the effect of mutual coupling on SINR were proposed in [17] and [47]. As this was not the main target of this research, we did not consider these solutions in the design process.

To demonstrate the suitability of the system for null-steering applications, two different amplitude distributions have been simulated and measured. The beam directions of 0° and 30° were chosen. The pattern depicted in Figure 4.14a and 4.14b correspond to simulation and measurement performed using the uniform $(0, 0, 0, 0)$ and 3 dB tapered $(-3, 0, 0, -3)$ amplitude distribution, respectively, for the beam direction of 0° . As it is marked in the figures, the null positions are moved and the measured SLL ratio is increased from 8 dB to 23 dB by changing the amplitude distribution with an identical trend in both simulation and measurement. The same distributions were examined for the beam direction of 30° and the results are shown in Figure 4.15. We can see the change of null positions and occurrence of a new null in the direction of the 60° . These measurements confirm null-steering and beam-shaping by independent control over the phase and amplitude. The reduction of the gain for

the tapered excitation (in both simulation and measurement) is due to the lower injected power to the antenna.

Advanced pattern design techniques considering the SLL ratio, null managements and beam pointing can be found in [7] and [17]. However, the instability in the system limited the amplitude tuning resolution and made the process of calibration and measurement difficult, so we were not able to take advantage of those techniques for more complex pattern shaping examples.

4.5. Source of Errors in the Optical Domain

In the proposed optical beamforming scheme, several phenomena can cause errors and degrade the performance:

CW laser source: The optical source must be stable from the point of view of power level, polarization and operating wavelength to respect calibration information. The stability of the multi-carrier generator is directly proportional to the stability of the CW laser exploited to generate the carriers. However, small fluctuations of polarization and power level can be compensated by bias control and optical amplification stages. The requirements can be met by telecom, temperature stabilized distributed feedback (DFB) lasers.

FBG positioning: If the gratings are uniformly spaced, all the channels will experience the same propagation delay while traversing the DG-BF. If the spacing is non-uniform, some channels will have a higher propagation delay, which corresponds to excess phase retardation. It is relatively easy to control the positions of the gratings in the chain with a precision of 1 mm. This tolerance corresponds to an excess phase retardation of 2.8° at a modulation frequency of 5 GHz. This error can easily be compensated by proper offsetting of the calibration maps.

Sensitivity of FBGs to environmental parameters: The response of the FBG-based filters is sensitive to the temperature or stretch volatilities. Theoretically, when both these parameters are stabilized, there is no impact on the system performance. In this beamforming architecture, the fiber gratings are integrated and placed in the CO that usually has both vi-

bration proof facilities and automatic ventilation system. Nonetheless, the beamformer will require a temperature controlled package.

Asymmetry of power loss/gain between different channels: As described in Section 4.3, asymmetry in power delivery can originate from differences in non-flattened channel power, dissimilar RF connections, different responsivity of PDs, etc. A proper power regulation stage easily copes with this difficulty.

4.6. DG-BF Advantages and Disadvantages

The proposed beamforming system offers several advantages.

Simultaneous and independent control over amplitude and phase for each antenna in the array: Simultaneous control of amplitude and phase of the signal of each antenna in the array offers maximum flexibility in designing the radiation pattern. This allows for better interferer nulling and reduction of SLL. Previous published works based on FBG allow only for beam-steering by controlling the phase/delay of signals and to our knowledge, DG-BF is the first all-optical beamformer that supports this feature.

High speed adjustment of the radiation diagram: The DG-BF can be controlled by stretching or by adjusting the temperature of the gratings. Hence the speed of reaction of the beamformer is limited only by the speed of the stretcher. Piezoelectric stretchers can adjust the radiation diagram in a few milliseconds.

Easy integration with antenna remoting links: Antenna remoting through ROF links offers low transmission losses and immunity from electromagnetic interference and crosstalk compared to conventional coaxial antenna feeders. Also, optical WDM allows for addressing of several antennas over one single fiber. Optical signal processing can be implemented in ROF links in order to add beamforming functionalities. This is especially advantageous if the beamformer is designed to be localized and controlled at the CO, in order to simplify the base stations transceiver. However, if the ROF link antenna addressing is based on WDM, the beamformer must operate with constant optical wavelengths and can not rely on tunable sources because the wavelength positions are fixed by the WDM filters which route the optical signals from the CO to the base stations. DG-BF complies with

DWDM systems and allows for integration of multi-carrier laser source, optical modulator, beamformer, optical amplification stage and the processing center, all in the CO. This helps to share the cost of the equipment between several access points.

Reduced number of elements: The DG-BF employs few optical components: two chains of FBGs and a four-port circulator (or two three-port circulators) for independent complex control of four antennas. Furthermore, there is no need for employing TLS or tunable optical filters which reduces the complexity and the cost of the whole system.

Operation with DSB modulation systems: As we have discussed in Section 3.3.2, fiber dispersion has a detrimental effect on the propagation of DSB modulated signals: it causes each sideband of the optical modulated signal to have a different phase shift depending on the length of the fiber, dispersion and modulation frequency. At the optical receiver, each sideband beats with the optical carrier, and the two beat signals ideally interfere constructively. When the phase shift reaches π because of group delay dispersion, the intensity modulation is transformed into a pure phase modulation and no RF signal is detected. RF signal suppression has been observed also in beamformers based on chirped FBG, due to the chirp-induced dispersion within the modulation sidebands. Several authors have proposed to solve this issue by using single sideband (SSB) modulation instead of DSB [26], [28], but SSB requires a more complex and expensive modulation stage and does not allow for the use of low-cost modulators as those based on the electro absorption effect. The proposed beamformer is designed to be used with DSB signals and can be adjusted to compensate for RF signal suppression induced by fiber dispersion as shown in Section 3.4.

The main disadvantage of the proposed beamformer is the long length of each filter. Each filter has a length of 85 mm, therefore for beamforming of a four-element PAA two chains, each with a length of 36 cm, are required. Such long chains of gratings, along with the actuators needed for controlling the DG-BF, are not easy to package. Furthermore, such long gratings need large actuators and this increases power consumption of the system and makes it more susceptible to temperature fluctuation or vibration.

4.7. Conclusion

In this chapter, we described different components in the ROF link, the technique for increasing the RF gain and reducing the distortion. The calibration process for this beamformer was introduced and the measured amplitude and phase maps were presented. The radiation pattern measurement technique was explained and we demonstrated the beamsteering and null-steering capabilities of the DG-BF via comparing simulation and measurement results. A discussion of possible sources of error in the optical domain and their solutions were presented. Finally, we explained the advantages and disadvantages of this beamformer versus previous techniques.

Chapter 5

Conclusion

In this research, we investigated the feasibility of a novel phase-based optical beamformer with null-steering capacity and we demonstrated its performance via radiation pattern measurements. We reviewed recent developments in enabling beam-steering based on optical TTD method and our survey showed that many of the existing methods suffer from discrete beam-pointing or a need for complex devices such as TLS and tunable optical filters. Compared to other TTD solutions, the proposed null-steering optical beamformer is a reliable module for narrowband WLAN applications offering several advantages such as null-interfering and SLL reduction.

Beside the main target of this research, several parallel efforts were made to provide low-cost solutions for other components in the ROF link. We designed and fabricated the appropriate PAA, we set up the proper amplified detectors and we developed grating actuators. We made all these components compatible with our general link architecture and finally, we used them for radiation pattern measurements. In addition, since we were using an external modulator for narrowband applications, we took advantage of the modulator bias optimization technique to achieve RF gain improvement and distortion compensation.

For the first time to our knowledge, we examined the impact of the beamformer on the transmitted signal quality by measuring the EVM for IEEE 802.11a as one of the most common modulation formats used for WLAN applications. This test was indispensable since the beamformer module was based on FBG technology and the distortion of the signal phase could affect the IEEE 802.11 signal quality. The experimental results proved the ability of the null-steering beamformer to transmit the signal without distorting or adding noise.

The simulation and measurement results of the beamformer response for single-channel operation confirmed that the FBG-based filters provided enough dynamic range in setting the phase and amplitude of each element in the PAA. We then assembled the whole ROF link that relied on wavelength multiplexing to address each element. The multiwavelength light was generated by a multi-carrier laser source, externally modulated by an optimized-bias MZ modulator, optically amplified, processed by an optical null-steering beamformer, distributed over a 10 km fiber link, demultiplexed by an AWG, detected by the amplified PDs and finally fed to the PAA. The radiation pattern of the PAA was measured for several settings and the results demonstrated beam-steering, SLL reduction and null-steering capability.

From the system level point of view, this beamformer is compatible with DWDM architectures and can be integrated in the CO, resulting in shared equipment for several PAAs and consequently reducing the installation and maintenance costs. The flexibility in continuous selection of the phase excitation results in continuous beam-pointing. That means the beam-pointing resolution only depends on the accuracy of the FBG tuning.

From the point of view of implementation, the difficulties in the experimental work mostly came from fixing the fibers on the thermal actuators, stretching and stabilizing the filter responses. There are well-known commercial solutions that address these issues.

Future work

Regarding the successful measurement results for this type of beamformer, some efforts can be made to improve the functionality and performance of the system. As we already discussed, the main disadvantage of this system is the length of the gratings and non-compact multichannel solution. Without a new filter design, one can reduce the length of the gratings by increasing the chirp factor of the gratings. Shorter grating lengths will allow more stable and uniform temperature profile along the grating, lower power consumption and smaller packaging. In order to simplify the grating design, the solution based on GT-BF should be investigated further by relaxing some specifications. For instance, as we discussed in chapter one, a 2π controllability over the phase excitations enables the beamformer to cover a steering range of 180° . However, the extreme pointing angles are not of interest due to the antenna positioning limitation. Therefore, by reducing the phase tunability in the gratings response, we may be able to obtain a feasible multichannel solution of GT-BF for which the signal from a multiwavelength source could be processed by just a single pair of gratings and then demultiplexed to feed an antenna array. This would help in reducing the size and power consumption of this solution.

References

- [1] L. C. Odara, "Applications of antenna arrays to mobile communications. I," *Proc. of the IEEE*, vol. 85, pp. 1031-1060, 1997.
- [2] R. G. Vaughan, "On optimum combining at the mobile," *IEEE Transaction Vehicular Technology*, vol. 37, pp. 181-188, 1988.
- [3] M. Chryssomallis, "Smart Antennas," *IEEE Antennas and Propagation Magazine*, vol. 42, pp. 129-136, 2000.
- [4] J. H. Winters, "Smart Antennas for Wireless Systems," *IEEE Personal Communications Magazine*, vol. 5, pp. 23-27, 1998.
- [5] R. Dijk, R. Bregman, A. Roodnat, and F. E. Vliet, "Photonic True Time Delay Beamformer Demonstrator for a Radio astronomical Array Antenna," *Proc. of International Topical Meeting on Microwave Photonics*, pp. 78-80, 2000.
- [6] W. D. Jones, "Keeping Cars from Crashing," *IEEE Spectrum*, vol. 38, pp. 40-45, 2001.
- [7] C. A. Balanis, *Antenna Theory Analysis and Design*, 2nd ed., Wiley, 1996.
- [8] D. Parker, and D. C. Zimmermann, "Phased-Arrays –Part II: Implementations, Applications, and Future Trends," *IEEE Transactions on Microwave Theory and Techniques*, vol. 50, pp. 688-698, 2002.
- [9] J. B. Hacker, R. E. Mihailovich, M. Kim, and J. F. DeNatale, "A Ka-Band 3-Bit RF MEMS True-Time-Delay Network," *IEEE Transactions on Microwave Theory and Techniques*, vol. 51, pp. 305-308, 2003.
- [10] A. J. Seed, "Microwave Photonics," *IEEE Transactions on Microwave Theory and Techniques*, vol. 50, pp. 877-887, 2002.
- [11] J. G. Wang, and A. S. Mohan, "Modified Wiener beamforming for indoor multipath channels," *Proc. of IEEE 6th International Conference on Universal Personal Communications Record*, vol. 2, pp. 823-827, 1997.
- [12] M. Katz and J. Ylitalo, "Extension of space-time coding to beamforming WCDMA base stations," *Proc. of Vehicular Technology Conference*, vol. 2, pp. 1230-1234, 2000.
- [13] Y. F. Chen, and C. S. Wang, "Adaptive Antenna Arrays for Interference Cancellation in OFDM Communication Systems with Virtual Carriers," *IEEE Transactions on Vehicular Technology*, vol. 56, pp. 1837-1844, 2007.

- [14] Y. C. Chung, and R. L. Haupt, "Optimum amplitude and phase control for an adaptive linear array using a genetic algorithm," *Proc. of IEEE Antennas and Propagation Society International Symposium*, vol. 2, pp. 1424-1427, 1999.
- [15] M. M. Sisto, *Optical Distribution Links for OFDM-based Wireless Networks*, to appear as the Ph.D. Thesis, Laval University, 2008.
- [16] R. A. Sainati, *CAD of Microstrip Antennas for Wireless Applications*, Artech House, 1996.
- [17] R. C. Hansen, *Phased Array Antennas*, Wiley, 1998.
- [18] G. Kumar, and K.P. Ray, *Broadband Microstrip Antennas*, Artech House, 2003.
- [19] E. O. Hammerstad, "Equations for Microstrip Circuit Design," *Proc. of Fifth European Microwave Conference*, pp. 268-272, 1975.
- [20] I. J. Bahl, and P. Bhartia, *Microstrip Antennas*, Artech House, 1980.
- [21] Rogers Corporation, "RO4230™ High Frequency Circuit Material Antenna Grade Laminate", *Preliminary Data Sheet*, publication 92/124, 2006.
- [22] R. Kashyap, *Fiber Bragg Gratings*, 1st ed., Academic Press, 1999.
- [23] A. Molony, L. Zhang, J. A. R. Williams, I. Benion, C. Edge, and J. Fells, "Fiber Bragg-grating true-time delay system: Discrete-grating array 3-b delay lines and chirped-grating 6-b delay lines," *IEEE Transaction Microwave Theory Technology*, vol. 45, pp. 1527-1530, 1995.
- [24] G. A. Ball, W. H. Glenn, and W. W. Morey, "Programmable fiber optic delay line," *IEEE Photonic Technology Letter*, vol. 6, pp. 741-743, 1994.
- [25] J. L. Corral, J. Martí, J. M. Fuster, and R. I. Laming, "True time-delay scheme for feeding optically controlled phased-array antennas using chirped-fiber gratings," *IEEE Photonic Technology Letter*, vol. 9, pp. 1529-1531, 1997.
- [26] B. Ortega, J. L. Cruz, J. Capmany, M.V. Andrés, and D. Pastor, "Variable delay line for phased-array antenna based on a chirped fiber grating," *IEEE Transaction Microwave Theory Technology*, vol. 48, pp. 1352-1360, 2000.
- [27] Beatriz Ortega, José L. Cruz, José Capmany, Miguel V. Andrés, and Daniel Pastor, "Analysis of a microwave time delay line based on a perturbed uniform fiber Bragg grating operating at constant wavelength," *IEEE Journal Lightwave Technology*, vol. 18, pp. 430-436, 2000.

- [28] Vincenzo Italia, Marco Pisco, Stefania Campopiano, Andrea Cusano, and Antonello Cutolo, "Chirped Fiber Bragg Gratings for Electrically Tunable Time Delay Lines," *IEEE Journal Selected Topics in Quantum Electronics*, vol. 11, pp. 408-416, 2005.
- [29] H. Zmuda, R. A. Soref, P. Payson, S. Johns, and E. N. Toughlian, "Photonic beamformer for phased array antennas using a fiber grating prism," *IEEE Photonic Technology Letter*, vol. 9, pp. 241-243, 1997.
- [30] D. B. Hunter, M. E. Parker, and J. L. Dexter, "Demonstration of a Continuously Variable True-Time Delay Beamformer Using a Multichannel Chirped Fiber Grating," *IEEE Journal Lightwave Technology*, vol. 54, pp. 861-867, 2006.
- [31] N. P. Bansal, and R. H. Doremus, *Handbook of Glass Properties*, Academic Press, 1986.
- [32] Y. Liu, J. Yang, and J. Yao, "Continuous true-time-delay beamforming for phased array antenna using a tunable chirped fiber grating delay line," *IEEE Photonic Technology Letter*, vol. 14, pp. 1172-1174, 2002.
- [33] A. Hilt, "Microwave harmonic generation in fiber-optical links", *Proc. of 13th International Conference on Microwaves, Radar and Wireless Communications*, pp. 693-698, 2000,
- [34] M. M. Sisto, M. E. Mousa Pasandi, S. Larochelle, L. A. Rusch, "Optical Phase and Amplitude Control for Beamforming with Multiwavelength Gires-Tournois Bragg Grating Cavities," *Proc. of 4th IASTED International Conference on Antennas, Radar, and Wave Propagation*, pp. 238-243, 2007.
- [35] C. K. Madsen, and J. H. Zhao, *Optical Filter Design and Analysis*, Wiley, 1999.
- [36] M. Poulin, Y. Vasseur, F. Trepanier, M. Guy, M. Marin, Y. Painchaud, J. Rothenberg, "Apodization of a multichannel dispersion compensator by phase modulation coding of a phase mask," *Proc. of Optical Communication Conference, OME17*, 2005.
- [37] S. Doucet, S. LaRoche, M. Morin, "Multi-channel tunable chromatic dispersion compensator and profiler," *Proc. of 31st European Conference on Optical Communication*, vol. 3, pp. 421-422, 2005.
- [38] J. Skaar, L. Wang, and T. Erdogan, "On the Synthesis of Fiber Bragg Gratings by Layer Peeling," *IEEE Journal Lightwave Technology*, vol. 37, pp. 165-173, 2001.

- [39] IEEE Standard, 802.11a-1999 [ISO/IEC 8802-11:1999/Amd 1:2000(E)] (Supplement to IEEE 802.11, 1999 Edition) Part 11: Wireless LAN Medium Access Control (MAC) and Physical Layer (PHY) Specifications High-Speed Physical Layer in the 5 GHz Band, 1999.
- [40] T. S. Cho and K. Kim, "Effect of Third-Order Intermodulation on Radio-Over-Fiber Systems by a Dual-Electrode Mach-Zehnder Modulator with ODSB and OSSB Signals," *IEEE Journal Lightwave Technology*, vol. 24, pp 2052-2058, 2006.
- [41] M. E. Mousa Pasandi, M. M. Sisto, S. Larochelle, L. A. Rusch, "Low Distortion Null-Steering Beamforming with a Cascade of Fiber Bragg Grating Gires-Tournois", *Proc. of 20th Annual Meeting of the IEEE Lasers and Electro-Optics Society*, pp.114-115, 2007.
- [42] Y. Kim, S. Doucet, M. E. Mousa Pasandi, and S. LaRochele, "Optical multicarrier generator for radio-over-fiber systems", *Journal Optics Express*, vol. 16, pp. 1068-1075, 2008.
- [43] B. H. Kolner and D. W. Dolfi, "Intermodulation distortion and compression in an integrated electrooptic modulator," *Journal Applied Optics*, vol. 26, pp. 3676-3680, 1987.
- [44] M. M. Sisto, S. LaRochele, and L.A. Rusch, "Gain optimization by modulator bias control in radio-over-fiber links," *IEEE Journal Lightwave Technology*, vol.18, pp. 1840-1842, 2006.
- [45] I. A. Kostko, M. E. Mousa Pasandi, M. M. Sisto, S. Larochelle, L. A. Rusch, D. V. Plant, "A radio-over-fiber link for OFDM transmission without RF amplification", *Proc. of 20th Annual Meeting of the IEEE Lasers and Electro-Optics Society*, pp. 339-340, 2007.
- [46] I. J. Gupta, and A. A. Kseinski, "Effect of Mutual Coupling on the Performance of Adaptive Arrays," *IEEE Transaction Antennas Propagation*, vol. 31, pp. 785-791, 1983.
- [47] R. S. Adve and T. K. Sarkar, "Elimination of the Effects of Mutual Coupling in an Adaptive Nulling System with a Look Direction Constraint," *Proc. of Antennas and Propagation International Symposium*, pp. 1164-1167, 1996.

- [39] IEEE Standard, 802.11a-1999 [ISO/IEC 8802-11:1999/Amd 1:2000(E)] (Supplement to IEEE 802.11, 1999 Edition) Part 11: Wireless LAN Medium Access Control (MAC) and Physical Layer (PHY) Specifications High-Speed Physical Layer in the 5 GHz Band, 1999.
- [40] T. S. Cho and K. Kim, "Effect of Third-Order Intermodulation on Radio-Over-Fiber Systems by a Dual-Electrode Mach-Zehnder Modulator with ODSB and OSSB Signals," *IEEE Journal Lightwave Technology*, vol. 24, pp 2052-2058, 2006.
- [41] M. E. Mousa Pasandi, M. M. Sisto, S. Larochelle, L. A. Rusch, "Low Distortion Null-Steering Beamforming with a Cascade of Fiber Bragg Grating Gires-Tournois", *Proc. of 20th Annual Meeting of the IEEE Lasers and Electro-Optics Society*, pp.114-115, 2007.
- [42] Y. Kim, S. Doucet, M. E. Mousa Pasandi, and S. LaRochele, "Optical multicarrier generator for radio-over-fiber systems", *Journal Optics Express*, vol. 16, pp. 1068-1075, 2008.
- [43] B. H. Kolner and D. W. Dolfi, "Intermodulation distortion and compression in an integrated electrooptic modulator," *Journal Applied Optics*, vol. 26, pp. 3676-3680, 1987.
- [44] M. M. Sisto, S. LaRochele, and L.A. Rusch, "Gain optimization by modulator bias control in radio-over-fiber links," *IEEE Journal Lightwave Technology*, vol.18, pp. 1840-1842, 2006.
- [45] I. A. Kostko, M. E. Mousa Pasandi, M. M. Sisto, S. Larochelle, L. A. Rusch, D. V. Plant, "A radio-over-fiber link for OFDM transmission without RF amplification", *Proc. of 20th Annual Meeting of the IEEE Lasers and Electro-Optics Society*, pp. 339-340, 2007.
- [46] I. J. Gupta, and A. A. Kseinski, "Effect of Mutual Coupling on the Performance of Adaptive Arrays," *IEEE Transaction Antennas Propagation*, vol. 31, pp. 785-791, 1983.
- [47] R. S. Adve and T. K. Sarkar, "Elimination of the Effects of Mutual Coupling in an Adaptive Nulling System with a Look Direction Constraint," *Proc. of Antennas and Propagation International Symposium*, pp. 1164-1167, 1996.